Contribution à l'optimisation de la gestion de production des parc éoliens

Stefano Macri

Centre Val de Loire UNIVERSITÉ Spirit of the Loire Valley

UNIVERSITÉ D'ORLÉANS

UNIVERSITE D'ORLEANS

ÉCOLE DOCTORALE ÉNERGIE, MATÉRIAUX, SCIENCES DE LA TERRE ET DE L'UNIVERS

Laboratoire PRISME

Thèse présentée par :

Stefano MACRÌ

soutenue le : **18 décembre 2020**

pour obtenir le grade de : **Docteur de l'Université d'Orléans**

Discipline : **Energetique et mécanique des Fluides**

Contribution à l'optimisation de la gestion de production des parcs éoliens

Contribution to the optimisation of the wind farm production management

THÈSE DIRIGÉE PAR :

Sandrine	**AUBRUN**	Professeure des universités, Ecole Centrale de Nantes
Annie	**LEROY**	Maître de conférences HDR, École de l'Air

RAPPORTEURS :

Carlos Simao	**FERREIRA**	Professeur, TU Delft
Jeroen	**VAN BEECK**	Professeur, von Karman Institute for Fluid Dynamics

JURY :

Sandrine	**AUBRUN**	Professeure des universités, Ecole Centrale de Nantes
Pierre	**BÉNARD**	Maître de conférences, INSA Rouen Normandie
Carlos Simao	**FERREIRA**	Professeur, TU Delft
Azeddine	**KOURTA**	Professeur des universités, Université d'Orléans (President du jury)
Annie	**LEROY**	Maître de conférences HDR, École de l'Air
Jeroen	**VAN BEECK**	Professeur, von Karman Institute for Fluid Dynamics

INVITÉ:

Nicolas	**GIRARD**	Ingénieur Energies Renouvelables, ENGIE Digital

A mia madre,
stella polare della mia vita.

The answer, my friend, is blowin' in the wind,
The answer is blowin' in the wind.

Bob Dylan

Acknowledgments

This work was supported by Engie SA and the Agence Nationale de la Recherche (ANR) through the Investissements d'Avenir program under the Labex CAPRYSSES Project (ANR-11-LABX-0006-01).

A word of thanks to the staff of Engie Green in Lyon for the wonderful period I spent with them. They made me feel at home and I really appreciated it.

I also want to thank all the staff of the LHEEA laboratory at the Ecole Centrale de Nantes for their hospitality in the last part of my PhD. They made me feel at home despite the adversities due to the pandemic.

Personal Acknowledgments

Finally this journey has come to an end. It was not an easy travel but I will always remember it with joy and a bit of nostalgia. Now is time to turn page through a new chapter of my life, but before a few words of gratitude are due to the people who accompanied me during this time.

Firstly let me thank my directors (in order of appearance in this story) Sandrine and Annie. I thank Sandrine for the PhD project and for putting so much trust in a man coming from the motor-vehicles on such a green topic. I also really appreciated her commitment to my PhD despite the distance imposed by her new position in Nantes. I know it is not usual to find this dedication in similar conditions, for this a big thank you. I also really appreciated the short time we spent together in Nantes before the pandemic. A really special thank goes to Annie who has bravely chosen to support my PhD project on route. Her contribution was crucial to accomplish this success. I will always remember her daily visit to the wind tunnel, even when there was not a problem to solve but just to comfort me during these though periods. I'm really grateful to Sandrine and Annie for their commitment in this project, their approach to science, work and life it has been an example to me.
A sincere thanks goes to Nicolas Girard for the industrial supervising, I really appreciated his sensibility and approach to our meetings. A special thanks goes also to Thomas, who helped me integrate into the Engie Green team in Lyon and for the nice work we did together.
A really special thanks goes to Stéphane Loyer, the lord of the wind tunnel, without his help the wind would not haven blown. I also want to specially thank Yahia Haidous, without his help to design the control system of our experimental set-up this work would have never been completed. I also want to apologize to Yahia because I know that, since he met me, his hair started to fall faster because of my complex requests.

A word of thanks to all the member of ESA team of the PRISME laboratory, for the good time spent together. As concerns the PhD candidates/doctors, a special thanks goes to Francesco, his wisdom and support was really appreciated during this journey as well as the discussions, especially when we disagree (which is quite often). A huge thanks goes to Marco, his presence and help during the tough periods was really beneficial. I also want to thank Sophie for her sympathy and good humour. A sincere thanks goes to Roshan, I really appreciated his company. I also thank Wassim, especially for the very good food he offered us because of his laziness with French language. Speaking about the "seniors", I would like to give a special thank to Pierre-Yves for the very good time we spent together, it is rare

to meet such an interesting and brilliant person on both academics and personal side.

Thanks to the other components of the PRISME laboratory, especially to Sylvie who really helped me with the administrative stuff. Thanks to all the ECM team especially Fabrice, Christine, Bruno and Pierre. And all their PhD candidates/-doctors, Nicolas, Charles, Antony and of course Marco Di Lorenzo.

A huge thanks goes to Alessandro (better known as Geo) the friend who most of all was a guide and example of love for science and good life in these years. He has been figuratively, and sometime also literally, a light in the dark nights but most of all an example of braveness, coming two times in Orléans and one time in Nantes (during a pandemic) it is stuff for brave men. A special thanks goes also to Simone e Davide (Virtu & Sarah), our friendship persists despite the distance and the adversities and I really felt you there when necessary. I also want to thanks all my friend who showed an effort to keep a relation despite the distance (I apologies if I forgot someone), Giuppe & Aline, Giugno, Jacopo, Gianni, Picca, Ricky, Scuse & Fra, Marchino & Chiara, Mario, Zazza, Silvia, Greg, Andrea, Giuliano, Marco, Anna, Filippo, Lorenzo.

To conclude I would like to thank my family for the support they gave me in these years and for the example of rectitude they have been and they'll always be for me.

Contents

List of Figures

List of Tables

List of Symbols

τ_0	Aerodynamic time scale [s]
c	Airfoil chord [m]
α	Angle of attack [°]
ρ	Air density [kg/m^3]
ν	Air kinetic viscosity [m^2/s]
$\Delta\Gamma$	Circulation [m^2/s]
D	Diameter of the turbine [m]
R_v	Dimensionless vector resolution []
S_d	Disc surface [m^2]
P	Extracted power [kW]
τ^*_{end}	End of the wake deviation or end thrust variation [τ_0]
U_d	Flow rate at the disc location [m s^{-1}]
η_{CP}	Global power performances []
a	Induction factor []
U_∞	Incoming flow velocity [m s^{-1}]
τ^*_{lag}	Lag fitting parameter [τ_0]
C_P	Power coefficient of the turbine []
R	Radius of the turbine [m]
U_{ref}	Reference flow velocity [m s^{-1}]
U_{hub}	Reference wind speed at hub height [m s^{-1}]
Re	Reynolds number []
Ω	Rotational velocity of the turbine [rad s^{-1}]

P_∞	Static pressure upstream of the model [Pa]
τ^*_{start}	Start of the wake deviation or start thrust variation [τ_0]
St	Strouhal number []
T_u	Turbulence intensity in the streamwise direction [%]
k	Turbulent kinetic energy [$\mathrm{m}^2/\mathrm{s}^2$]
$a^{'}$	Tangential induction factor []
λ_r	Tip-speed ratio of the turbine []
C_T	Thrust coefficient of the turbine []
T	Thrust force applied to the actuator disc [N]
$\Delta\tau^*_{CT}$	Thrust variation duration [τ_0]
U	Velocity in the streamwise direction [$\mathrm{m\,s}^{-1}$]
U_w	Wake flow velocity [$\mathrm{m\,s}^{-1}$]
θ	Wake deviation angle [°]
$\Delta\tau^*_\theta$	Wake deviation duration [τ_0]
χ	Wake skew angle angle [°]
ΔX	Wind turbine spacing [m]
γ	Yaw angle of the turbine [°]
$\Delta\tau^*_m$	Yaw manoeuvre duration [τ_0]

List of Abbreviations

ABL	Atmospheric Boundary Layer
AD	Actuator Disc
BEM	Blade Element Theory
BL	Boundary Layer
HAWT	Horizontal Axis Wind Turbine
HIT	Homogenous Isotropic Turbulent
MAE	Mean Absolute Error
PIV	Particle Image Velocimetry
PSD	Power Spectral Density
SCADA	Supervisory Control And Data Acquisition
SMV	Sole du Moulin Vieux
VD	Velocity Deficit
WF	Wind Farm
WT	Wind Turbine

Résumé du Manuscrit

Ce travail de thèse présente des travaux originaux concernant la modélisation en soufflerie d'une stratégie de contrôle de la production énergétique d'un parc éolien, le dérapage volontaire d'une éolienne. L'attention est posée sur l'analyse du comportement du sillage au cours de la mise en œuvre de cette stratégie pour en déduire les aspects dynamiques et en caractériser les temps transitoires. Les études des interactions entre les sillages des éoliennes et des stratégies associées pour en réduire les effets négatifs (perte de production) se sont multipliés dans les dernières années. Elles concernent autant des études numériques qu'expérimentales, à échelle réelle et à échelle réduite en soufflerie. L'aspect particulier et original de cette thèse n'est donc pas le sujet de recherche en général mais la façon dont on l'approche. En effet, au moment où on écrit, à la connaissance de l'auteur, il n'existe pas d'études en soufflerie, et probablement même pas à l'échelle réelle, du transitoire de mise en œuvre de la stratégie de dérapage de sillage en terme de temps de stabilisation du sillage de l'éolienne à sa nouvelle position. On estime cette information cruciale pour affiner la capacité d'évaluation de la rentabilité de cette stratégie de contrôle de la production d'un parc éolien et pour mieux maitriser le phénomène en lui-même. Vu le caractère innovant de ce type d'étude, des protocoles expérimentaux ad hoc ont été mis en place et une métrique d'évaluation du phénomène à été proposée en s'appuyant sur des concepts d'aérodynamique utilisés pour l'analyses des phénomènes transitoires-instationnaires. Les travaux expérimentaux ont abouti à la proposition d'un possible modèle empirique pour décrire le phénomène étudié qui pourrait être utile si implémentés dans des modèles d'optimisation de production de parcs éoliens. Une autre partie de ce travail de thèse consiste à analyser des données de terrain issues d'un vrai parc éolien pour essayer de proposer une façon innovante de déduire les interactions de sillage entre deux éoliennes.
L'objectif de cette thèse était de fournir des informations sur la dynamique du sillage d'un modèle d'éolienne en se concentrant particulièrement sur le comportement du sillage pendant l'exécution des manœuvres de dérapage. Afin d'atteindre cet objectif, la caractérisation aérodynamique du sillage d'un modèle d'éolienne et son effet sur la charge d'un modèle d'éolienne en aval résultant d'une variation dynamique en dérapage positive (scénario de désalignement) ou négative (scénario

de réalignement) ont été étudiés expérimentalement pour différentes conditions de vent incident, nombres de Reynolds et facteurs d'induction axial.
Pour faciliter la lecture, le manuscrit à été divisé en six chapitres, dans le chapitre 1 une introduction générale sur le contexte et les objectifs de recherche à été donnée. Dans le chapitre 2, une brève revue de la littérature concernant les éoliennes et les parcs éoliens, avec un accent particulier sur le contrôle des parcs éoliens à été faite. Dans le chapitre 3, les montages expérimentaux ainsi que les systèmes de mesures et la méthodologie appliquée pour les essais en soufflerie ont été abordés. Le chapitre 4 à été consacré aux résultats et aux discussions des expériences en soufflerie, tandis que le chapitre 5 à présenté la mise en place et les résultats de la campagne à grande échelle. Enfin, au chapitre 6, les conclusions générales de ces travaux ainsi que leurs perspectives ont été examinées.
Dans la suite de ce résumé étendu, les principaux résultats et/ou sujets de chacun des principaux chapitres sont décrits de manière générale. Les détails complets sont disponibles dans les chapitres rédigés en langue anglaise.

Dans le chapitre 1, le contexte mondial de la recherche sur l'énergie éolienne avec un accent particulier sur les interactions de sillage et les sujets de recherche sur le contrôle des parcs éoliens ont été brièvement présentés.
L'énergie éolienne est l'une des solutions d'énergie renouvelable permettant de réduire les émissions mondiales de CO_2 et de lutter contre le réchauffement climatique causé partiellement par la production d'électricité conventionnelle. Au cours des dernières décennies, le secteur de l'énergie éolienne a connu une énorme croissance technologique, ce qui a eu un effet favorable sur la demande mondiale d'énergie éolienne. Par exemple, la capacité totale d'énergie éolienne installée dans le monde en 2019 était de 651 GW, soit une croissance de 10 % par rapport à 2018 (GLOBAL [2019]). Cette augmentation considérable et continue a contribué à mettre en lumière certains aspects difficiles qui doivent encore être abordés et résolus, comme la nécessité d'améliorer les techniques pour maximiser le rendement énergétique. Afin d'atteindre cet objectif, les exploitants de parcs éoliens ont commencé à augmenter la densité des parcs éoliens, avec pour conséquence une augmentation des interactions de sillages qui entraînent des pertes de puissance et une augmentation des charges de fatigue dans les parcs éoliens. Comme une éolienne extrait une certaine quantité d'énergie cinétique du vent incident, elle réduit l'énergie disponible pour les éoliennes dans son sillage. De plus, en raison de l'ajout du cisaillement du vent, le sillage est également source de production de turbulence. La présence de turbulence entraîne une augmentation des fluctuations de charges aérodynamiques sur l'éolienne dans le sillage. Les pertes de puissance et l'augmentation de la fatigue dues à ces interactions, généralement utilisées pour la conception des parcs éoliens, sont encore difficiles à estimer avec les modèles

d'ingénierie. En effet, la grande incertitude sur l'estimation du potentiel de la ressource éolienne dans un parc éolien, ainsi que la faible capacité à modéliser correctement les interactions du sillage, comme la non prise en compte de la dynamique du sillage, sont les principales raisons de ces imprécisions sur les estimations des pertes de puissance et de la fatigue. Néanmoins, différentes études (Barthelmie et al. [2009], Rezaei [2015], Beyer et al. [1994]) suggèrent que, selon la configuration du parc éolien (distance et configuration des éoliennes), les pertes de puissance du parc éolien dues aux effets de sillage peuvent atteindre des valeurs allant jusqu'à 23 % par rapport aux résultats de la configuration optimale. Il convient de noter que, généralement, la plupart des pertes se produisent dans les deux premières éoliennes en interaction, atteignant ainsi des valeurs considérablement plus élevées que 23 %. En ce qui concerne l'augmentation de la fatigue due à l'interaction du sillage entre deux éoliennes, elle peut atteindre 80 % (Sanderse [2009]). Outre l'amélioration des estimations des conséquences des interactions de sillage, un nouveau thème de recherche dans le domaine de l'énergie éolienne vise à étudier les stratégies de contrôle des parcs éoliens basées sur les caractéristiques aérodynamiques et mécaniques afin de réduire ces interactions. Une stratégie de contrôle des parcs éoliens consiste à contrôler individuellement chaque éolienne afin de réduire ses effets de sillage sur les turbines situées plus en aval et de maximiser la production totale d'énergie du parc éolien. Les solutions les plus couramment étudiées sont doubles : le contrôle de l'induction et le contrôle de dérapage. La première est basée sur une stratégie de réduction de la puissance, en effet la réduction de l'extraction de puissance d'une éolienne en amont laisse plus d'énergie cinétique disponible pour une éolienne en aval. Cette solution a permis de réaliser des gains allant jusqu'à environ 5 % (Machielse et al. [2008]) dans la production globale de deux éoliennes dans des conditions d'interaction de sillage complet. La seconde consiste à orienter le sillage, c'est-à-dire à désaligner volontairement une éolienne en fonction de la direction du vent afin de dévier son sillage et de réduire ainsi l'interaction du sillage avec une éolienne située en aval. Cette solution a montré qu'un gain allant jusqu'à environ 12 % (Adaramola and Krogstad [2011]) de la production globale de deux éoliennes dans des conditions d'interaction avec le sillage est possible. Alors que, jusqu'à présent, la dynamique de l'écoulement du sillage et de la charge des éoliennes lors des manœuvres de dérapage est généralement abordée par des modèles quasi-statiques, ce travail vise à quantifier les propriétés dynamiques de ces phénomènes. L'analyse de la dynamique des manœuvres de dérapage offre de nouvelles perspectives sur l'interaction entre les sillages et permet d'estimer le délai entre la manœuvre sur une éolienne en amont et son effet sur une éolienne en aval, ainsi que le temps d'advection du sillage par exemple. Ces analyses sont très importantes pour mettre en œuvre la stratégie appropriée dans les contrôleurs d'éoliennes. À cette fin, dans ce travail, un scénario typique d'interaction de sillage entre deux

éoliennes, modélisées avec un disque poreux, est reproduit dans des conditions de soufflerie pour étudier les effets de la stratégie de contrôle de dérapage. Une attention particulière est accordée à l'étude de la dynamique du sillage et de la charge de l'éolienne et à la transition entre la condition sans dérapage et la condition avec dérapage. Le choix d'expériences en soufflerie plutôt que de campagnes de mesures à grande échelle est dû à de multiples facteurs tels que la contrôlabilité et la répétabilité des conditions d'écoulement et de la manœuvre. En effet, ce sont des conditions fondamentales pour la bonne reproduction de la dynamique des stratégies de contrôle. Ce travail vise à caractériser la réponse au sillage et à la charge d'une éolienne à l'application d'une stratégie de contrôle du sillage L'étude de la transition entre les conditions d'absence de dérapage et celles de dérapage vise à mettre en évidence la réponse du sillage à une variation de dérapage et l'influence du type de manœuvre de dérapage sur cette réponse temporelle.
En plus des études en soufflerie, l'analyse de l'interaction du sillage entre deux éoliennes a également été réalisée en conditions réelles. En effet, dans le cadre du projet SMARTEOLE[1], les données à haute résolution temporelle ($1Hz$) d'une éolienne appartenant à *Engie Green*, et instrumentée par cette dernière, étaient disponibles à des fins d'analyse et de recherche.

Le chapitre 2 a présenté une revue non exhaustive de la littérature sur l'état de l'art concernant l'aérodynamique des éoliennes et des parcs éoliens, avec une attention particulière sur les propriétés du sillage, les modèles d'ingénierie du sillage et le contrôle des parcs éoliens. La modélisation des éoliennes utilisée dans le cadre des expériences de cette thèse, basée sur le concept du disque actuateur, a été décrite ainsi que les principales propriétés du sillage, en mettant l'accent sur les conditions de sillage dévié. En outre, les stratégies de contrôle des parcs éoliens les plus courantes ont été présentées.
L'aérodynamique et la modélisation des éoliennes à axe horizontal (HAWT) ont été traitées. Il convient de noter que les HAWT ne sont pas la seule typologie d'éoliennes mais qu'elles sont les plus utilisées. Généralement, une HAWT est composée d'un rotor à trois pales relié à un arbre à faible vitesse, puis, par l'intermédiaire d'une boîte de vitesses, la vitesse de rotation est augmentée avant d'atteindre le générateur d'électricité via l'arbre à grande vitesse. Ces composants, ainsi que plusieurs autres composants tels que la plupart du système de contrôle et d'acquisition de données (SCADA), sont intégrés dans la nacelle. La nacelle est placée au sommet d'une tour d'acier reposant généralement sur une base en béton. Le système de contrôle d'une éolienne est composé de plusieurs capteurs et actionneurs. Deux des plus importants sont l'anémomètre et la girouette, tous deux placés au-dessus de la nacelle. En effet, l'anémomètre fournit la vitesse du vent tandis que la gi-

[1] https ://anr.fr/Project-ANR-14-CE05-0034

rouette indique la direction du vent. En fonction de ces deux variables, le système de contrôle de l'éolienne permet une régulation optimale de la machine. En fait, la majeure partie de la régulation des éoliennes dépend simplement de la vitesse et de la direction du vent. La nacelle est capable de tourner (en changeant l'orientation de la turbine) afin de faire face au vent en fonction de la mesure de la girouette. Au-delà d'autres facteurs tels que la régulation du réseau et les situations d'urgence, la vitesse du vent est une variable clé pour déterminer si une éolienne est opérationnelle ou non. En effet, les éoliennes ont une plage de vitesse de vent opérationnelle délimitée par un seuil de vitesse de vent de coupure et de démarrage, et en dehors de cette plage, elles sont volontairement arrêtées. D'autres réglages telles que l'angle de calage des pales et la vitesse du rotor sont ajustées en fonction des mesures de la puissance active du générateur. Bien que, pour les expériences en soufflerie dont il est question dans ce travail, la turbine ait été modélisée par le concept de *actuator disc*, un examen plus approfondi de l'aérodynamique est nécessaire. Étant donné le but de l'étude du sillage d'une éolienne en condition de dérapage, certaines notions sur le modèle *actuator disc vortex* utilisé dans *Glauert theory* sont également utiles. En effet, ces notions sont nécessaires pour estimer les performances d'une éolienne en conditions de dérapage ainsi que pour comprendre les modèles de déviation de sillage traités dans cette étude.
Les propriétés principales d'un sillage éolien ont été présentées. La recherche sur les propriétés aérodynamiques d'une éolienne a été déterminante pour le succès de l'énergie éolienne. Malgré les efforts déployés dans l'étude aérodynamique, il faut constater que certaines des questions les plus difficiles, notamment en termes d'étude des interactions avec le sillage, n'ont pas encore été résolues. Néanmoins, pour la plupart des problèmes non résolus, certaines lois empiriques ont été développées. Bien que ces lois empiriques aient généralement été utiles pour la conception des éoliennes et des parcs éoliens, comme le mentionne Vermeer et al. [2003], il est nécessaire de revenir à une approche plus physique afin d'avoir une compréhension plus approfondie. En général, le sillage est divisé en deux régions bien distinctes :

- Le *near wake* situé juste en aval du rotor. Cette région est caractérisée par des signatures aérodynamiques distinctes de la présence du rotor. En effet, il est possible d'identifier les signes du nombre de pales, les effets tridimensionnels sur le sillage et les tourbillons de bout de pales. La dimension dans le sens de l'écoulement de cette région dépend de différents facteurs externes tels que la turbulence ambiante et la hauteur du rotor et son point de fonctionnement, mais elle se situe généralement entre un et cinq diamètres en aval de l'éolienne.

- Le $far\ wake$ est la région en aval du *near wake* et c'est donc la région où les caractéristiques du rotor ne sont plus distinguables dans le sillage. Les tour-

billons à l'extrémité des pales ont perdu leurs caractéristiques individuelles et les distributions de vitesse du sillage deviennent auto-similaires. Le sillage lointain d'une éolienne est donc similaire au sillage d'un disque d'actuateur (disque poreux).

Le troisième chapitre se termine avec une revue sur le principaux aspects du contrôle de parc éoliens. Comme détaillé dans (Pao and Johnson [2009]), le contrôle des parcs éoliens peut être utilisé pour l'optimisation de la qualité de la production d'énergie électrique et de la stabilité du réseau, ou pour l'étude de la réduction des interactions aérodynamiques entre les éoliennes afin de réduire les pertes de puissance dues aux sillages. Jusqu'à présent, le contrôle des parcs éoliens était principalement axé sur l'aspect électrique, mais l'amélioration de l'aérodynamique a été de plus en plus étudiée ces dernières années (Knudsen et al. [2015], Sanderse [2009]). Cet intérêt pour les interactions aérodynamiques est certainement une conséquence de la densification de la configuration des parcs éoliens, comme mentionné au chapitre 1. N'étant pas traitée dans ce travail, l'approche concernant les aspects électriques n'a pas été abordée dans cette étude. En ce qui concerne le contrôle du parc éolien orienté sur les performances aérodynamiques, il existent deux stratégies principales : le contrôle par *induction* (ou réduction de puissance ou bridage), qui consiste en une régulation volontaire vers le bas de l'éolienne en amont afin de laisser plus d'énergie cinétique aux éoliennes en aval, et le contrôle par *yaw* (ou décalage en lacet), qui consiste en un désalignement en lacet volontaire de l'éolienne en amont afin de dévier le sillage et limiter l'intéraction avec les éoliennes en aval. Ces deux méthodes ont pour objectif de contrôler la production d'énergie de chaque éolienne afin d'augmenter le taux de production de l'ensemble du parc éolien et/ou de réduire les effets de fatigue.

Dans le chapitre 3, une description détaillée des trois installations expérimentales utilisées pour cette étude ainsi que les deux souffleries du laboratoire $PRISME$ ont été décrites avec un accent particulier sur les conditions d'écoulement générées : deux campagnes dans des conditions d'écoulement turbulent homogène et isotrope (HIT) et une dans des conditions de couche limite atmosphérique (ABL). Les expériences ont été réalisées dans les deux souffleries du laboratoire $PRISME$ de l'Université d'Orléans. La première était une soufflerie à jet ouvert de type "$Eiffel$" où un ventilateur aspire l'air ambiant et un convergent le dirige vers la section d'essai, augmentant sa vitesse et amortissant les fluctuations de vitesse. La soufflerie a une section d'essai carrée de 0,5 m × 0,5 m × 2 m. À l'extrémité du convergent, une grille de turbulence à géométrie uniforme est située afin de fournir un écoulement turbulent isotrope homogène avec une vitesse d'écoulement pouvant atteindre 40 ms^{-1}. La première campagne en écoulement turbulent isotrope homogène (campagne HIT1) a été réalisée dans cette installa-

tion.La deuxième soufflerie est la soufflerie en circuit fermé "$LucienMalavard$". Cette installation est composée de deux sections d'essai : la section d'essai principale qui a une section carrée de 2 m × 2 m × 5 m avec une vitesse d'écoulement maximale de 50 ms^{-1} et la section d'essai de retour qui a une section carrée de 4 m × 4 m × 20 m avec une vitesse maximale de 12,5 ms^{-1}. Dans la section d'essai principale, les expériences de la campagne en écoulement turbulent isotrope homogène (campagne HIT2) ont été réalisées, tandis que dans la section d'essai de retour, une couche limite atmosphérique a été modélisée à une échelle réduite afin de réaliser des essais dans des conditions reproduisant une couche limite atmosphérique (campagne ABL).
Les modèles utilisés pour la représentation des rotors d'éoliennes ont été décrits et leur choix a été motivé. Les propriétés du disque et la mise à l'échelle ont été présentées. Cette approche de modélisation des éoliennes est largement utilisée dans la littérature (Muller et al. [2015], Yu et al. [2017], Bastankhah and Porté-Agel [2014], Van Gent et al. [2017]), en particulier lors d'expériences en soufflerie à des échelles géométriques très basses. Comme référence à pleine échelle, il a été choisi une éolienne de 80 m de diamètre avec une vitesse de vent de référence de 12 ms^{-1}. En ce qui concerne l'échelle géométrique : pour la première campagne dans des conditions d'écoulement turbulent isotrope homogène (HIT1), l'échelle était de 1 :800, tandis que pour la deuxième campagne dans des conditions d'écoulement turbulent isotrope homogène (HIT2) et pour la campagne la campagne ABL, l'échelle était de 1 :320 avec une gamme de nombres de Reynolds, basée sur le diamètre du rotor, d'environ 10^4. Cela a conduit à un diamètre D de 0,1 m pour les conditions HIT1 et de 0,25 m pour les conditions HIT2 et ABL. Les disques étaient soutenus par une tige cylindrique reproduisant la tour de l'éolienne, dont le diamètre était de 0,005 m pour les conditions HIT1 et de 0,01 m pour les conditions HIT2 et ABL. Dans tous les cas, la hauteur du moyeu a été fixée à 0,25 m. Ce choix sera détaillé dans les prochaines sections. Deux types différents de grillage métallique ont été utilisés afin de reproduire deux niveaux de porosité, et donc deux facteurs d'induction différents. Les caractéristiques géométriques des mailles ainsi que les niveaux de porosité, les facteurs d'induction et les valeurs conséquentes des coefficients de puissance et de poussée sont énumérés pour les deux mailles utilisées. Une description détaillée du protocole expérimental en ce qui concerne la mise à l'échelle des disques et des manœuvres de dérapage, le suivi du sillage (protocole d'acquisition $Stereo\ PIV$ et post-traitement des données) et les mesures de variation de charge du modèle d'éolienne en aval (protocole d'acquisition des données issues de la balance aérodynamique 6 DOF et post-traitement des données) a été fournie. Une attention particulière a été accordée à la réduction d'échelle de l'éolienne et des manœuvres de dérapage en fonction de la taille de l'éolienne et de la vitesse de manœuvre réaliste. En conséquence de cette approche,

la durée de la manœuvre (mise à l'échelle selon une condition de pleine échelle) est un multiple de l'échelle de temps aérodynamique du rotor (τ_0), ce qui a conduit à l'analyse de la dynamique relativement lente de la stratégie d'orientation du sillage transitoire sur une éolienne opérationnelle. En outre, une description exhaustive des méthodes les plus courantes de détermination du centre de sillage et des motivations qui ont conduit au choix de celle basée sur la densité de puissance éolienne disponible à la position d'un modèle hypothétique d'éolienne en aval a été fournie.

Dans le chapitre 4 la déviation du sillage, la puissance éolienne disponible et les variations de poussée ont été analysées. L'angle de déviation du sillage, la puissance éolienne disponible et le coefficient de poussée du modèle d'éolienne en aval ont été choisis comme paramètres de mesure et ont d'abord été analysés en fonction de différents angles de dérapage en configuration statique. Ensuite, avant d'analyser la conséquence d'une variation dynamique de l'angle de dérapage sur ces paramètres, une évaluation des performances aérodynamiques des deux modèles d'éoliennes a été effectuée à l'aide des équations classiques $Momentumtheory$ et comparée aux performances de deux éoliennes fonctionnant dans des conditions optimales (pas de dérapage, pas d'interaction avec le sillage). Les résultats montrent que selon les équations $Momentum\ theory$ et la définition classique des performances des parcs éoliens, la déviation du sillage ne semble pas avoir d'effet positif sur les performances globales des éoliennes. Cette conclusion est contradictoire avec la littérature sur les expériences de parcs éoliens en grandeur réelle sur la déviation du sillage et la reproduction en soufflerie de la déviation du sillage par des modèles d'éoliennes en rotation. Par conséquent, ces résultats devraient suggérer la non-faisabilité de l'analyse des performances par l'utilisation de la théorie du disque actuateur pour l'évaluation d'une telle stratégie de contrôle des parcs éoliens. Ensuite, des considérations sur la performance du parc éolien, la durée, le début et la fin de la réponse temporelle du sillage à une variation dynamique de dérapage ont été estimés et comparés. Les principaux résultats sont résumés ici. Les résultats globaux ne montrent aucune influence notable des conditions d'écoulement (flux turbulents isotropes homogènes ou flux de la couche limite atmosphérique) ou des nombres de Reynolds sur les propriétés statiques et dynamiques des différentes mesures. L'influence du degré de modélisation physique de l'éolienne (disque poreux par rapport au modèle d'éolienne en rotation) sur les résultats n'a pas été étudiée car on suppose que cette caractéristique ne joue pas un rôle majeur dans la dynamique du sillage en dérapage, mais cette question doit être approfondie. En ce qui concerne la caractérisation de l'ampleur de la déviation du sillage dans des conditions de dérapage statique, les résultats montrent que la déviation du sillage est inférieure d'un ordre de grandeur à l'incrément de dérapage et que la relation entre la déviation du sillage et l'angle de dérapage n'est pas linéaire, comme on l'a

déjà constaté dans la littérature. Dans le cas d'un niveau de porosité plus élevé, l'incrément de poussée est beaucoup plus faible que dans le cas d'une porosité plus faible. Cependant, alors qu'une influence significative de la porosité sur l'angle de déviation du sillage et l'amplitude de la poussée du modèle d'éolienne en aval est constatée dans des conditions statiques, aucune influence significative de la porosité n'est observée sur la dynamique du sillage et de la charge. D'autre part, l'analyse des trois mesures révèle des caractéristiques temporelles différentes selon que la manœuvre de lacet est positive ou négative. En général, le transitoire de déviation du sillage a une durée légèrement plus courte et commence plus tard pour la variation de dérapage négative que pour la positive. Une bonne connaissance de ces effets permet de déterminer le temps nécessaire au développement complet du pilotage du sillage. Au contraire, la variation de poussée commence plus tard pour la manœuvre de dérapage positive que pour la négative. L'influence de la vitesse de la manœuvre de dérapage a été testée et le doublement de la vitesse de la manœuvre dérapage ne semble pas influencer la dynamique du sillage ou de la charge. Enfin, l'étude montre que les mêmes propriétés dynamiques du sillage de l'éolienne en amont et de la variation de charge de l'éolienne en aval ne peuvent être généralisées à aucune configuration de variation de dérapage, et que la vitesse d'advection doit être supposée différente selon la direction de la manœuvre de dérapage. Une première étape dans la proposition de coefficients d'ajustement a été faite afin de soutenir un modèle dynamique de la déviation du sillage ou de la poussée pour les variations de dérapage positives ou négatives. Les lois d'ajustement mises en œuvre pour les conditions dynamiques de dérapage semblent être exploitables pour une généralisation d'une loi décrivant le phénomène de transitoire. En particulier, le coefficient c s'est avéré assez robuste pour être utilisé dans une loi empirique. En ce qui concerne le coefficient τ^*_{lag}, bien que sa signification physique soit claire, son application dans une loi empirique exige plus de prudence. En effet, les valeurs mesurées ne suivent pas une tendance aussi claire que pour le coefficient de durée. Ceci est probablement dû à la spécificité de ce paramètre qui est directement lié au début du phénomène, et par conséquent il est plus sensible à sa dispersion. Néanmoins, τ^*_{lag}, étant représentatif de l'advection, pourrait être ajusté en faisant une simple hypothèse d'advection. D'autre part, le paramètre c, représentatif de la durée transitoire, peut mieux amortir les fluctuations de τ^*_{start} et τ^*_{end} qui sont généralement concordantes (toutes deux surestimées ou sous-estimées). À ce stade, une exploitation plus poussée de ces données et études doit être effectuée en vue de la mise en œuvre d'un modèle empirique. En effet, un modèle empirique capable de prédire la dynamique du sillage et de la variation de charge serait bénéfique s'il était mis en œuvre dans des modèles de contrôle des parcs éoliens fournissant des informations sur la réponse temporelle du sillage et de la charge des éoliennes en aval à la manœuvre de dérapage de l'éolienne en amont. Une bonne connaissance

de ces réponses temporelles et de leur variabilité en fonction du type de manœuvre de dérapage serait importante pour le réglage des modèles de contrôle dynamique des parcs éoliens, ce qui contribuerait à améliorer leur précision. Bien que durant ce travail de thèse, différentes échelles de modèles d'éoliennes, niveaux de porosité et conditions d'écoulement aient été testés, il serait intéressant de tester des niveaux de porosité plus faibles pour reproduire des situations de signature de sillage plus élevée (coefficient de poussée plus élevé) ainsi que de tester également avec des modèles d'éoliennes en rotation pour voir si le degré de modélisation de l'éolienne est important sur la dynamique du sillage. Une autre perspective intéressante concernant l'analyse des variations de charge serait de placer les modèles d'éoliennes en amont et en aval sur des balances aérodynamiques synchronisées afin d'évaluer et de comparer correctement la variation de la dynamique de charge des deux modèles.

Dans le chapitre 5 un travail préliminaire sur l'analyse en grandeur réelle des retards de réponse entre les éoliennes en fonction de leur degré d'interaction à été présenté. Grâce au post-traitement d'une base de données de terrain recueillie au cours du projet ANR SMARTEOLE sur deux éoliennes en grandeur réelle, le délai global entre la dynamique de deux éoliennes a été évalué. Des fonctions de corrélation entre les séries temporelles de puissance des deux éoliennes acquises à une fréquence d'échantillonnage de 1 Hz ont été réalisées et les délais entre les réponses des éoliennes évalués. En sélectionnant les séries temporelles en fonction de la direction du vent et du point de fonctionnement de l'éolienne, l'influence de l'interaction du sillage sur le délai entre les réponses de l'éolienne a été étudiée. En outre, l'influence du niveau des interactions de sillage a été examinée en termes de statistiques d'inter-corrélation montrant une concordance générale avec les considérations classiques d'advection. Les résultats obtenus ont montré que ce type d'analyse peut contribuer à affiner les paramètres dynamiques des modèles de contrôle des parcs éoliens. Pour plusieurs raisons (entre autres le stockage), il n'est pas trivial de disposer d'une grande base de données à 1 Hz. Le but de ce travail était donc d'évaluer la potentialité de cette approche sur l'exploitation des mesures de puissance pour récupérer la réponse des éoliennes, en particulier dans les conditions d'interaction avec un sillage.

Chapter 1

Introduction

Wind energy is one of the renewable energy solutions to reduce the global CO_2 emissions and fight the global warming caused by conventional power generation. In the last decades, the wind energy sector has had a huge technological growth with a consequent favourable effect on the global wind energy demand. For example consider that the installed total wind energy capacity globally in 2019 was 651 GW with a growth of 10 % compared to 2018 (GLOBAL [2019]). This considerable and continuative increase helped to highlight some challenging aspects that still have to be faced and solved such as the necessity to improve the techniques to maximise the power yield. In order to accomplish this goal, wind farm operators started to increase the wind farm density with a consequent growth of the wake interactions that bring power losses and fatigue loads in wind farms. As a wind turbine extracts an amount of kinetic energy from the incoming wind, it reduces the energy available for the wind turbines in its wake. Moreover, due to the adding of wind shear, the wake is also source of turbulence production. The presence of turbulence leads to the increase of the load fluctuations over the wind turbine in the wake. The power losses and fatigue increase due to these interactions, generally used for wind farm design, are still difficult to estimate with engineering models. Indeed, the high uncertainty on the estimation of the wind resource potential within a wind farm, together with the low capability to properly model the wake interactions, such as the non-consideration of the wake dynamics, are the principal reasons of these inaccuracies on the power losses and fatigue estimations. Nevertheless, different studies (Barthelmie et al. [2009], Rezaei [2015], Beyer et al. [1994]) suggest that, depending on the wind farm layout (wind turbine distance and pattern), the wind farm power losses due to the wake effects can reach values up to 23 % by comparison with the optimal layout results. It has to be remarked that, generally, most of the losses occur within the first two interacting wind turbines reaching so values considerably higher than 23 %. Concerning the fatigue increase due to wake interaction between two wind turbines this can reach value

up to 80 % (Sanderse [2009]). Apart from improving the wake interactions consequences estimations, a new research topic in the wind energy community aims to study wind farm control strategies based on aerodynamic and mechanic features in order to reduce these interactions. A wind farm control strategy consists in controlling individually each wind turbine in order to reduce its wake effects on the closer downstream turbines and maximise the total wind farm power production. The most commonly investigated solutions are twofold: the induction control and the yaw control. The first one is based on a power curtailment strategy, indeed reducing the power extraction of an upstream wind turbine leaves more kinetic energy available for a downstream one. This solution has shown gains up to $\approx 5\%$ (Machielse et al. [2008]) in the global production of two wind turbines in fully wake interactions conditions. The second one consists in the wake steering, where a wind turbine is voluntarily misaligned according to the wind direction in order to deflect its wake and so reducing the wake interaction with a downstream wind turbine. This solution has shown that a gain up to $\approx 12\%$ (Adaramola and Krogstad [2011]) in the global production of two wind turbines in fully wake interactions conditions is possible.

Whereas, so far, wake flow and wind turbine load dynamics during yaw manoeuvres are usually approached by quasi-static models, this work aims at quantifying dynamical properties of these phenomena. Analyzing yaw manoeuvre dynamics offers new insights into wake interactions and provides the opportunity to estimate the delay between the manoeuvre on an upstream wind turbine and its effect on a downstream one, as well as wake advection time for example. Those analyses are very important to implement the proper strategy in the wind turbine controllers. To this end, in this work, a typical scenario of wake interaction between two wind turbines, modelled with a porous disc, is reproduced in wind tunnel conditions to investigate the effects of the yaw control strategy. Particular attention is given to the study of the wind turbine wake and load dynamics and the transition between the no yaw condition and the yawed condition. The choice of wind tunnel experiments instead of full scale measurement campaigns is due to multiple factors such as the controllability and the repeatability of the flow conditions and manoeuvrer. Indeed, these are fundamental conditions for the proper reproduction of control strategy dynamics. This work aims to characterize the wake and load response of a wind turbine to the application of a wake steering control strategy. The study of the transition between the non yawed and the yawed conditions wants to provide an highlight on the wake response to a yaw variation and the influence of the kind of yawing manoeuvrer to this time response. In addition to the wind tunnel studies, the analysis of the wake interaction between two wind turbines was also performed in full scale conditions. Indeed, in the frame-

work of the SMARTEOLE project[1] the high time resolution ($1Hz$) wind turbine data from a wind farm owned and instrumented by *Engie Green* were available for research analysis purposes.

The manuscript will be organized as it follow. In chapter 2, a brief review of the literature concerning wind turbine and wind farm, with particular focus on wind farm control will be done. In chapter 3, the experimental set ups as well as the measurement systems and methodology applied for wind tunnel tests will be discussed. Chapter 4 will be dedicated to the wind tunnel experiments results and discussions while chapter 5 will show the full scale campaign set up and results. Finally, in chapter 6, the overall conclusions of this work as well as its perspectives will be discussed.

[1] https://anr.fr/Project-ANR-14-CE05-0034

Chapter 2

Theoretical background and literature review

This chapter presents a non exhaustive review on the state of the art concerning wind turbines and wind farm aerodynamics, with particular attention on the wake properties, wake engineering models and wind farm control. In section 2.1 the wind turbine aerodynamics and modelling based on the actuator disc concept and *Betz theory* will be described. In section 2.2, wake properties will be discussed with particular attention to the skewed wake properties. Finally, in section 2.3 the most common wind farm control strategies will be presented.

2.1 Wind turbine aerodynamics & modelling

In this section the aerodynamics and the modelling of Horizontal Axis Wind Turbines will be treated (HAWT). It is worth to notice that HAWTs are not the only typology of wind turbines but they are the most commonly used. Generally a HAWT (Fig.2.1) is composed by a three blade rotor connected to a low-speed shaft, then through a gear box the rotational speed is increased before reaching the electricity generator via the high-speed shaft. These components, together with several other components such as most of the Supervisory Control and Data Acquisition (SCADA) system, are embedded in the nacelle. The nacelle is placed at the top of a steel tower leaning generally on a concrete base. A wind turbine control system is composed by several sensors and actuators. Two of the most important are the anemometer and the wind vane, both placed over the nacelle. Indeed, the anemometer provides the wind speed while the wind vane the wind direction. According to these two variables, the wind turbine control systems provides the optimal regulation of the machine. Actually, most of wind turbine regulation just depends on wind speed and direction. The nacelle is able to rotate

(changing the turbine orientation) in order to face the rotor to the wind according to the wind vane measurement. Beyond other factors such as grid regulation and emergency situations, the wind speed is a key variable to determine whether a turbine is operational or not. Indeed, wind turbines have an operational wind speed range delimited by a cut-in and cut-off wind speed threshold, and out of this range, they are voluntarily shut-down. Other regulations such as the blade pitch angle and the rotor speed are adjusted according to the generator active power measurements. Although, for wind tunnel experiments discussed in this work, the turbine was modelled by the concept of *actuator disc*, a more extensive review of aerodynamics is necessary. Given the purpose of studying the wake of a wind turbine in yawed conditions, some notions about the *actuator disc vortex model* used in *Glauert theory* are also useful. Indeed, these concepts are necessary to estimate the wind turbine performances in yawed conditions as well to comprehend wake deviation models treated in this review.

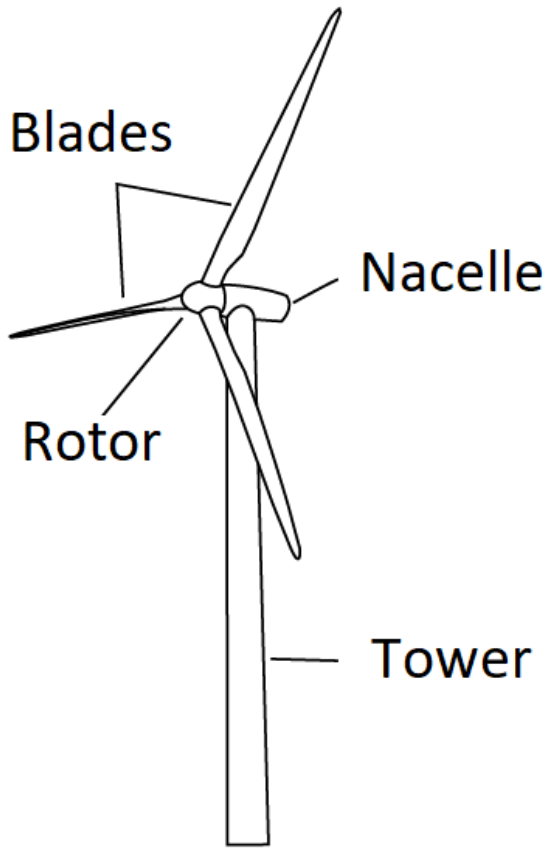

Figure 2.1 – Scheme of an HAWT in a three blade configuration

2.1.1 Actuator disc concept - Betz theory

The aerodynamic behaviour and the kinetic energy extraction of a wind turbine can be described using a simplified model such as the actuator disc or *Froude disc theory* (Froude [1889]). The peculiarity of this approach consists on the possibility to analyse the kinetic energy extraction without considering the rotor geometry. Indeed Froude simplifies the concept by modelling the rotor as a porous disc traversed by the air flow. This approach permits to estimate the global efficiency of a wind turbine by classical aerodynamic considerations. Figure 2.2 shows the simplified scheme of the actuator disc and stream-tube and the evolution of the main physical quantities involved in the energy extraction process.

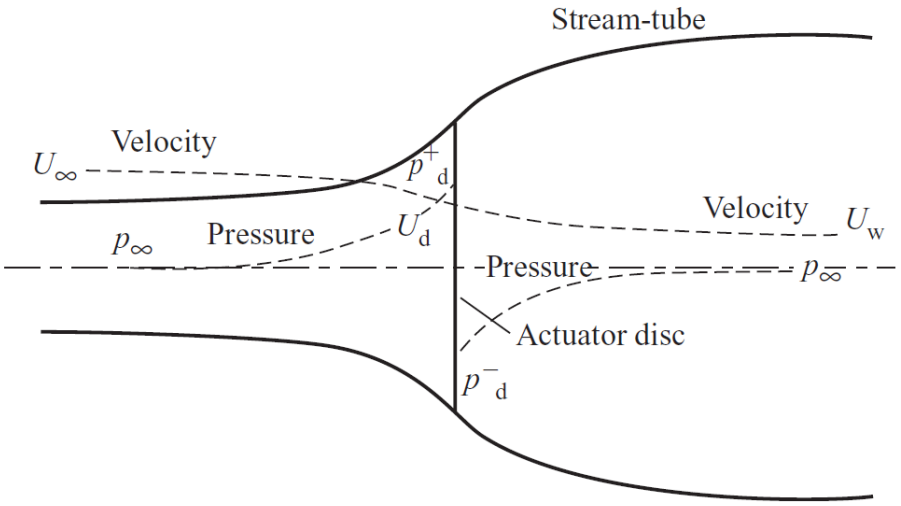

Figure 2.2 – An Energy Extracting Actuator Disc and Stream-tube from Burton et al. [2011].

Froude principle assumes the presence of a static pressure discontinuity imposed by the disc. This pressure difference creates a kinetic energy reduction that implies a flow speed diminution. The air mass traversing the rotor area is slowed down by the presence of the actuator area itself (the kinetic energy extraction). This air mass can be described by a stream tube with a width varying because of the mass conservation law and the flow speed reduction due to the kinetic energy extraction. Indeed, far upstream of the disc, the stream tube has a lower section, then, approaching the disc region, its section increases because of the start of the flow velocity reduction imposed by the presence of the disc. Far downstream of the disc, where the flow is maximally slowed down, the section further increases. Because of the mass conservation, the mass flow rate must be constant along the

stream tube. The stream-tube can be divided in three different regions: the upstream or free stream region witch parameters are characterized by the symbol ∞, the disc region (d) and the downstream or wake region (w). The mass flow rate will be so

$$\rho A_\infty U_\infty = \rho A_d U_d = \rho A_w U_w \tag{2.1}$$

where ρ is the air density (constant), A is the stream-tube section and U is the flow velocity. As mentioned before, according to Froude theory the disc induces a flow velocity variation to be superposed to the free stream velocity U_∞, this flow velocity reduction can be quantified as "aU_∞" where a is the axial induction factor. Consequently, the flow rate at the disc location can be retrieved by:

$$U_d = (1 - a)U_\infty \tag{2.2}$$

Knowing the disc surface it is possible to determine the rate of change of momentum imposed by the disc presence and associate it to the thrust applied to the actuator disc T:

$$T = (U_\infty - U_w)\rho A_d U_d \tag{2.3}$$

The thrust originating this variation can be also retrieved looking at the pressure difference across the disc, where p_d^+ represents the pressure at the upstream side of the disc and p_d^- at the downstream one. Thus,

$$T = (p_d^+ - p_d^-)A_d = (U_\infty - U_w)\rho A_d U_d = (U_\infty - U_w)\rho A_d U_\infty (1 - a) \tag{2.4}$$

Applying Bernoulli's equation (considering ρ constant) separately between the free stream region and the upstream disc gives:

$$\frac{1}{2}\rho U_\infty^2 + p_\infty = \frac{1}{2}\rho U_d^2 + p_d^+ \tag{2.5}$$

while between the downstream disc section and the wake region:

$$\frac{1}{2}\rho U_d^2 + p_d^- = \frac{1}{2}\rho U_w^2 + p_\infty \tag{2.6}$$

Combining equations (2.4), (2.5) and (2.6) gives:

$$\frac{1}{2}\rho A_d (U_\infty^2 - U_w^2) = (U_\infty - U_w)\rho A_d U_\infty (1 - a) \tag{2.7}$$

From eq 2.7 it is possible to retrieve the wake flow velocity:

$$U_w = (1 - 2a)U_\infty \tag{2.8}$$

Looking at equations 2.8 and 2.2 it is possible to understand as, half of the axial velocity deficit occurs at the disc and the other half downstream the disc. As mentioned before, the thrust force T applied on the disc can be described in one of the forms in equation 2.4. Considering equation 2.8, the thrust force can be expressed as:

$$T = 2\rho A_d U_\infty^2 a(1-a) \tag{2.9}$$

Knowing the thrust force and the speed at the disc location, it is possible to estimate the extracted power as:

$$P = TU_d = 2\rho A_d U_\infty^3 a(1-a)^2 \tag{2.10}$$

Once defined the thrust force and the extracted power it is possible to define the thrust coefficient C_T and the power coefficient C_P. The thrust coefficient is defined as the ratio between the thrust force and the total available force (Eq.2.11) while the power coefficient as the ratio between the extracted wind power and the available wind power (Eq.2.12).

$$C_T = \frac{T}{\frac{1}{2}\rho A_d U_\infty^2} = 4a(1-a) \tag{2.11}$$

$$C_P = \frac{P}{\frac{1}{2}\rho A_d U_\infty^3} = 4a(1-a)^2 \tag{2.12}$$

It must be highlighted that, as demonstrated by Betz in 1919, the maximal power extractable by a wind turbine cannot reach the available power. Indeed, by cancelling the derivative of (Eq.2.12):

$$\frac{dC_P}{da} = 4(1-a)(1-3a) \tag{2.13}$$

it is possible to determine the maximal value of the induction factor $a = \frac{1}{3}$, and consequently, the power coefficient maximum:

$$C_{Pmax} = \frac{16}{27} \tag{2.14}$$

This means that HAWT power extraction is constrained by a theoretical limit at about 59 % of the available power, and that, while this limit is reached, the wind turbine is reducing the flow speed in its wake of $\frac{1}{3}$ of the free stream U_∞. Figure 2.3 shows the variation of the power and thrust coefficients as a function of the axial induction factor, it has to be taken into account that for $a \geq 0.5$, U_w

becomes null and the momentum theory is no more applicable. Betz limit is just based on aerodynamic considerations, so it does not take technological constraints into consideration. It is worth to notice that nowadays, thanks to the technological improvement consequent to a huge effort in research and development, wind turbines under optimal wind conditions are capable to reach maximal power coefficients between 45 % and 50 % while just a few years ago this value was around 30 % 40 %.

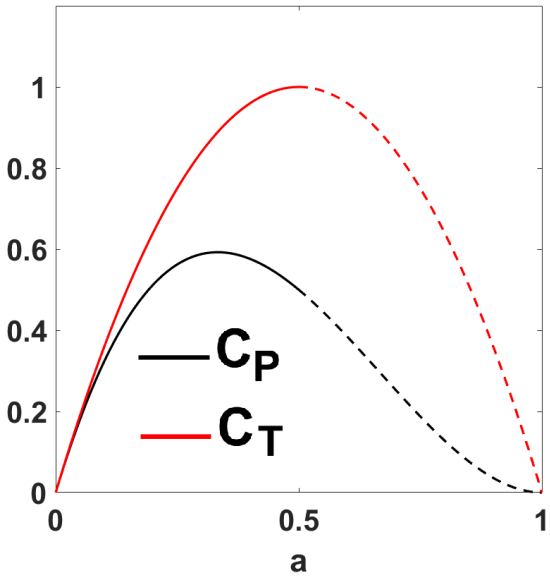

Figure 2.3 – C_P and C_T as a function of the axial induction factor. Dashed lines represents the region of non applicability of the momentum theory.

2.1.2 Rotating Froude disc

The conversion of the kinetic energy (wind flow) into electrical energy depends on the typology of the wind turbine. For HAWTs, wind energy extraction is obtained through a rotor revolving with an angular velocity Ω on an horizontal axis parallel to the wind direction, so that the rotor plane is faced to the incoming wind. Thanks to their aerodynamic design, the blades generate a pressure difference across the rotor area (disc) causing a loss of axial momentum in the wake and also an energy transfer into a resulting torque. This torque generates the rotor revolution on the basis of the energy extraction from the wind. Moreover the rotor revolution by reaction brings the air to rotate in the opposite direction to the rotor causing the increase of the wake angular momentum and the presence of velocity components on the rotor plane (Fig.2.4).

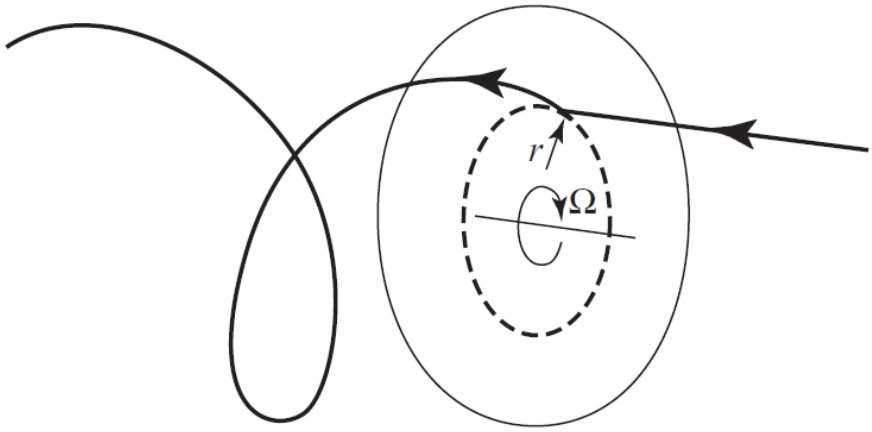

Figure 2.4 – Air particle trajectory through the rotor disc from Burton et al. [2011]

It has to be taken into account that the flow entering the rotor disc is mono-directional, and therefore, there are no components on the rotor plane and so no rotational motion. It is passing through the disc that the flow acquires its rotational components that persist along all the evolving wake. As for the variation in the streamwise velocity, the tangential velocity variation can be described by the tangential induction factor $a^{'}$. The tangential flow rate is zero far upstream the disc while it starts to increase passing through the disc. Indeed, it is $a^{'}\Omega r$ in the middle of the disc thickness where r is the radial distance from the centre of the disc and Ω the angular speed becoming $2a^{'}\Omega r$ just downstream the disc (Fig.2.5). The tangential and axial velocities depend on the radial position. Considering an annular ring, the axial velocity component together with the thrust force exerted on the ring are related by the rate of change of the axial momentum, while the tangential components of the velocity (on the rotor plane) and the torque acting

on the ring can be described by the rate of change of the angular momentum. The rotor disc can be considered as composed by a multitude of independent elementary rings where r is the radial coordinates and δr its radial width.

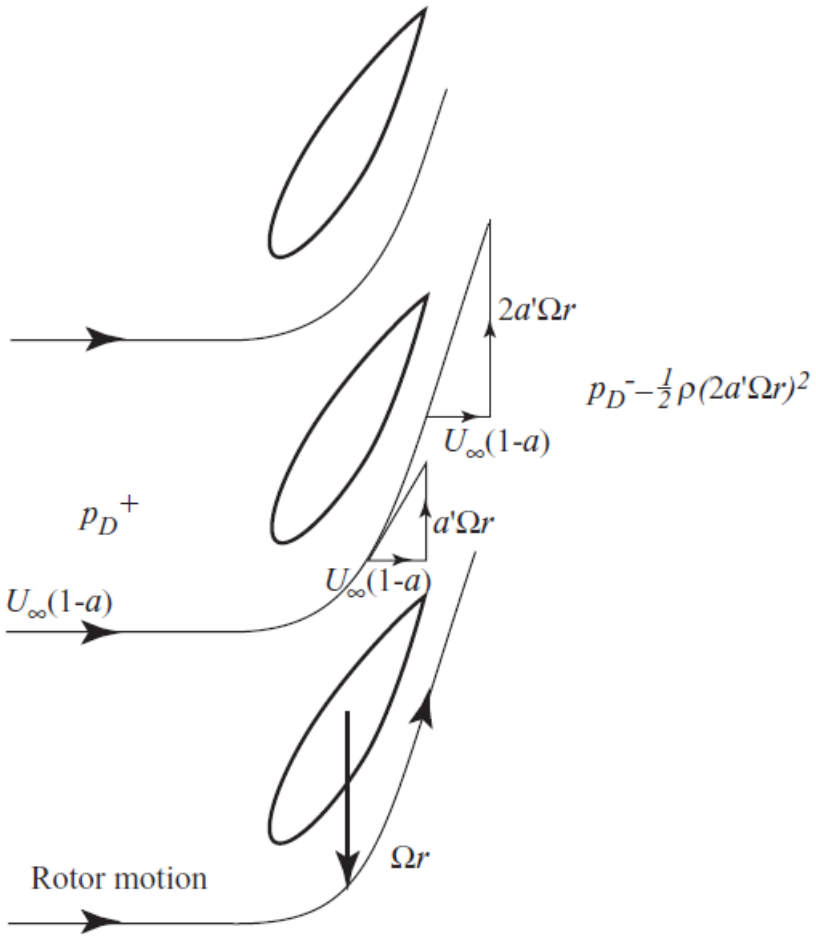

Figure 2.5 – Tangential speed through the rotor disc from Burton et al. [2011]

Indeed, as described in Burton et al. [2011], the torque exerted on the ring can be retrieved by the calculation of the rate of change of angular momentum (via the mass flow rate and the change of tangential velocity):

$$\delta Q = \rho \delta A_d U_\infty (1 - a) 2\Omega a' r^2 \tag{2.15}$$

given δA_d as the area of an annular ring. If δQ can be seen as the driving torque on the rotor shaft, the power output is consequently given by:

$$\delta P = \delta Q \Omega \tag{2.16}$$

As described in section 2.1.1, the power extracted from the wind can be described by the rate of change of axial momentum being in this case:

$$\delta P = 2\rho \delta A_d U_\infty^3 a(1-a)^2 \tag{2.17}$$

According to equations 2.15 and 2.16:

$$2\rho \delta A_d U_\infty^3 a(1-a)^2 = \rho \delta A_d U_\infty (1-a) 2\Omega^2 a' r^2 \tag{2.18}$$

Consequently:

$$U_\infty^2 a(1-a) = \Omega^2 r^2 a' \tag{2.19}$$

where Ωr is the tangential speed whose ratio with the free stream velocity ($\lambda_r = \frac{\Omega r}{U_\infty}$) represents the local speed ratio, which is called the tip speed ratio if calculated at the circumference of the disc (r=R). Equation 2.19 becomes:

$$a(1-a) = \lambda_r^2 a' \tag{2.20}$$

Considering the area of the ring $\delta A_d = 2\pi r \delta r$ and equation (2.16), the shaft power is:

$$\delta P = \delta Q \Omega = \frac{1}{2} \rho U_\infty^3 2\pi r \delta r 4a'(1-a)\lambda_r^2 \tag{2.21}$$

where $\frac{1}{2}\rho U_\infty^3 2\pi r \delta r$ represents the available power in the flow passing the annular ring. The other parameters state for the efficiency of the power extraction of the blade element:

$$\eta_r = 4a'(1-a)\lambda_r^2 \tag{2.22}$$

It is now possible to retrieve the power coefficient of the rotating disc:

$$\frac{d}{dr} C_P = \frac{4\pi \rho U_\infty^3 (1-a) a' \lambda_r^2 r}{\frac{1}{2}\rho U_\infty^3 \pi R^2} = \frac{8(1-a)a'\lambda_r^2 r}{R^2} \tag{2.23}$$

By introducing $\mu = \frac{r}{R}$, it gives:

$$\frac{d}{d\mu} C_P = 8(1-a)a'\lambda^2 \mu^3 \tag{2.24}$$

In this way, taking into account that both axial a and tangential a' induction factors vary depending on the radial position, it is possible to determine the global

power coefficient given a tip speed ratio λ by integrating equation 2.24. With the same principle applied for the actuator disc in section 2.1.1, it is possible to determine the following values of a and $a^{'}$ that maximise the power efficiency as fully detailed in Burton et al. [2011]:

$$a = \frac{1}{3} \;\&\; a^{'} = \frac{a(1-a)}{\lambda^2 \mu^2} \tag{2.25}$$

It is worth to notice that the axial induction factor a is the same as the one found for the non rotating condition and it does not depend on the radial position. Concerning the tangential induction factor $a^{'}$, it varies depending on the radial position. Substituting the values of $a^{'}$ showed in expression 2.25, in equation 2.24 and integrating between 0 and 1 gives:

$$C_P = \int_0^1 8(1-a)\frac{a(1-a)}{\lambda^2 \mu^2}\lambda^2 \mu^3 d\mu \tag{2.26}$$

Integrating and considering the value of a that maximise the C_P, it gives:

$$C_P = 4a(1-a)^2 = \frac{16}{27} \tag{2.27}$$

It is possible to conclude that the maximal values reachable by the power coefficient ($\frac{16}{27}$) is the same as for the non rotating case.

2.1.3 Actuator disc vortex cylinder model

The Froude disc is described as composed by multiples blades sweeping its surface. Each blade has a circulation $\Delta\Gamma$ that starts convecting at the blade tip at the flow velocity, evolving into an helical vortex downstream of the blade. Considering a high tip speed ratio and a blade number sufficiently high to have a small disc porosity, the aggregation of helical tip vortices will form a tubular surface containing the wake. Assuming that the number of blades could be increased up to infinity, the tubular surface can be considered as a continuous tubular vortex sheet. The vortex of intensity $\Delta\Gamma$ generated by the root of each blade balances the vortex generated at the tip of the blade developing along the rotation axis x and concurring to the total vorticity Γ caused by the blade root (Fig.2.6).

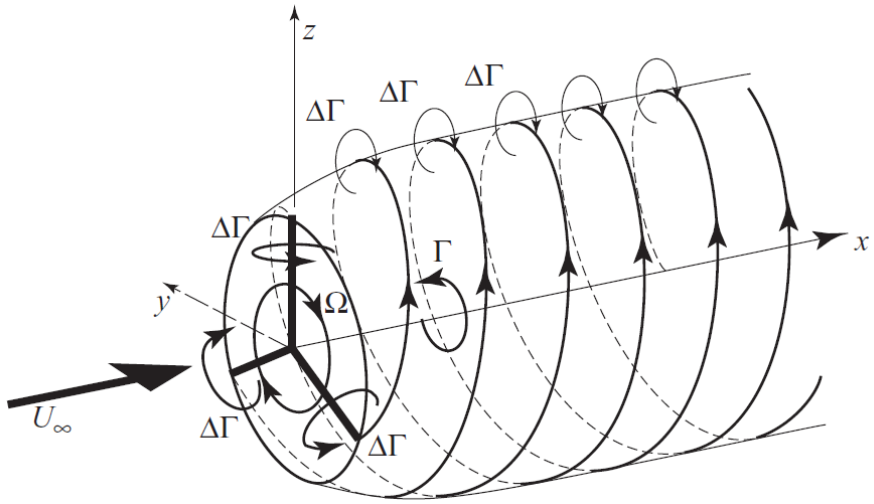

Figure 2.6 – Scheme of the vortex helical wake generated by a three blade rotor each with uniform circulation $\Delta\Gamma$. From Burton et al. [2011]

The total vorticity Γ is generated by the vortices present along all the blade, not only at the tip and the root of the blade. Figure 2.7 represents a simplified schematization of the wake vortices where only the symmetrical wake of a non rotating blade is considered. In this way, it is possible to appreciate the three dimensionality of the vortices and the distribution of the circulation along the blade.

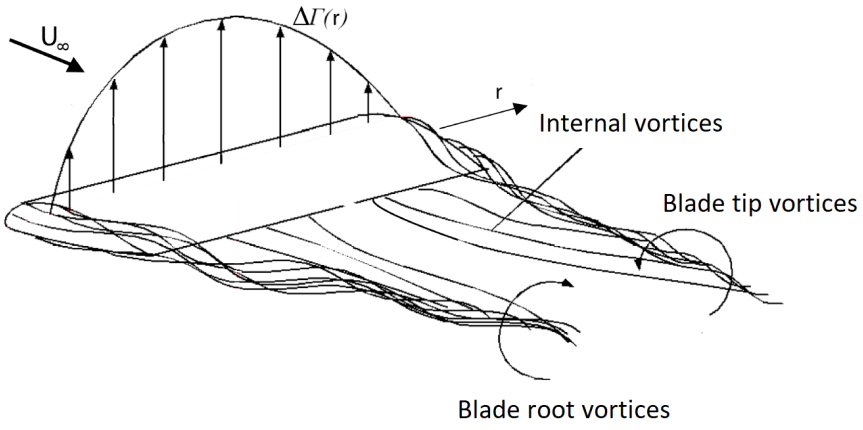

Figure 2.7 – Simplified vortex scheme of a symmetric blade wake without rotation.

It is worth to notice that in the case of a rotating blade the tip blade vortices are the main components of the wake in terms of vortical structures. Indeed, for a real blade configuration there is not a symmetry of the blade and so the circulation distribution $\Delta\Gamma$ is not uniform but increases radially. Moreover, in a real configuration, the presence of the nacelle affects the circulation at the blade root. It has to be taken into account that, due the flow rate reduction in the wake, the helical vortex tube increases radially although it is common to approximate the stream tube with a cylinder.

2.1.4 Glauert theory

All the considerations done until now do not take into account blade aerofoil geometric characteristics. Glauert [1935] proposed a model called *Blade Element Momentum* (BEM) in order to determine the loads on a blade depending on its geometric characteristics such as the blade angle of attack α and pitch angle β. This model, described in Burton et al. [2011], is generally used in the wind turbine numerical modelling and is based on the *Momentum theory*, and the *Blade Element theory*. *Glauert theory* relies on the assumption that the efforts on a blade element can be retrieved starting from the 2D characteristics of the blade profile. Indeed, all the three dimensional effects are ignored and the radial velocity is not considered. Given a radial position on the aerofoil, the wind speed components expressed as a function of the free-stream velocity, the flow parameters and the rotational speed of the rotor determine the angle of attack. At this point, knowing the radial evolution of the power and trust coefficient, the effort on the blade can be determined for given values of a and a'. Let's consider a wind turbine rotor composed of N blades, radius R, chord c and pitch angle β measured between the rotor plane and the blade zero lift line. As described in section 2.1.2, considering a blade element, its tangential speed at a distance r from the rotor centre is Ωr and the wake tangential speed at rotor position is $\Omega r a^{'}$. Thus the total tangential speed of the flow will be $(1 + a^{'})\Omega r$. The speed components, the pitch and angle of attack, as well as the effort exerted on a blade element at a radial position r are shown in figure 2.8.

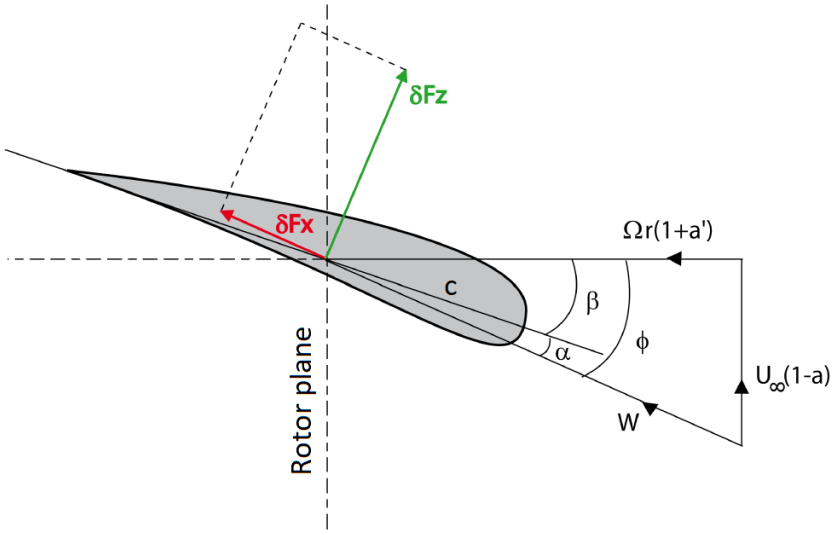

Figure 2.8 – Blade element velocities and forces.

Equation 2.28 gives the relative wind speed, while equations 2.29 and 2.30 the angle ϕ and α respectively.

$$W = \sqrt{U_\infty^2(1-a)^2 + \Omega^2 r^2(1+a')^2} \tag{2.28}$$

$$sin\phi = \frac{U_\infty(1-a)}{W} \qquad cos\phi = \frac{\Omega r(1+a')}{W} \tag{2.29}$$

$$\alpha = \phi - \beta \tag{2.30}$$

The lift force F_z, normal to the direction of the relative wind speed W, and the drag force F_x, parallel to W, exerted on a length δr of each blade are therefore:

$$\delta F_z = \frac{1}{2}\rho W^2 c C_z \delta r \tag{2.31}$$

$$\delta F_x = \frac{1}{2}\rho W^2 c C_x r \delta r \tag{2.32}$$

So, considering a N-blade wind turbine, it is possible to retrieve the elementary thrust δT and torque δQ applied on an annular ring of radius r and width δr:

$$\delta T = N\frac{1}{2}\rho W^2 c(C_z cos\phi + C_x sin\phi)\delta r \tag{2.33}$$

$$\delta Q = N\frac{1}{2}\rho W^2 c(C_z sin\phi + C_x cos\phi) r\delta r \tag{2.34}$$

Combining equations (2.33) and (2.34) with the expression of the elementary thrust and torque retrieved by the angular momentum theory (equation (2.35) and equation (2.36)), it is possible, with an iterative process not discussed here, to determine the radial evolution of the induction factors a and $a^{'}$.

$$\delta T = 4a^{'}(1 + a^{'})\frac{1}{2}\rho\Omega^2 r^2 2\pi r\delta r \tag{2.35}$$

$$\delta Q = 4a^{'}(1 - a)\frac{1}{2}\rho U_\infty^2 \Omega r^2 2\pi r\delta r \tag{2.36}$$

2.2 Wind turbine wake properties

The research on the aerodynamic properties of a wind turbine was determinant for the success of wind energy. Despite the efforts put into the aerodynamic study it has to be noticed that some of the most challenging issues, especially in terms of wake interactions study, have not been solved yet. Nevertheless, for most of the unsolved issues, some empirical laws have been developed. Although these empirical laws have generally been useful for the wind turbine and wind farm design, as mentioned by Vermeer et al. [2003], it is necessary to go back to a more physical approach in order to have a deeper comprehension. As seen in the previous section, the wind turbine's wake can be defined as the air mass losing pressure and velocity traversing the rotor. Generally, the wake is divided in two quite distinct regions:

- The *near wake* located just downstream the rotor. This region is characterized by distinguishable aerodynamics signs of the presence of the rotor. Indeed it is possible to identify the signs of the blade numbers, the three dimensional effects on the wake and the tip vortices. The size in the flow direction of this region depends on different external factors such as the ambient turbulence and the rotor height, but generally it is between one and five diameters downstream the wind turbine.

- The *far wake* is the region downstream the *near wake* and it is therefore the region where the rotor characteristics are no more distinguishable in the wake. Blade tip vortices have lost their individual characteristics and wake velocity distributions become self-similar. The far wake of a wind turbine is therefore similar to the wake of an actuator disc (porous disc). In the present study, the interaction of far wakes with a downstream wind turbine is studied, the literature review will focus on the far wake properties.

2.2.1 Wake in uniform flows

In the analysis of the wind turbine wake, different external factors have to be taken into account. Indeed, the vortical structures in the wind turbine wake are influenced by the atmospheric turbulence, the blade tip vortices, the wind turbine hub and tower and the wake meandering. Since in this work the wind turbine is modelled by the use of non rotating porous discs, only the wake generated by a porous disc will be shortly discussed here. Nevertheless, it can be found a detailed discussion on the effects of the vortical structures generated by the blade tips and their propagation according to the atmospheric turbulence level in the studies performed by Alfredsson and Dahlberg [1979], Troldborg et al. [2010]. Regarding the description of the meandering and its influence on the wake properties, some interesting studies have been done by Larsen et al. [2008, 2007], Trujillo and Kühn [2009], Larsen et al. [2009], Muller et al. [2015], Espana et al. [2012]. As concerns to the wake generated by a porous disc, in order to be able to properly compare the wake generated by a porous disc with the wake of a rotating wind turbine, it is necessary to introduce the variables that permits to do a reliable comparison. The porous disc is defined by a porosity level (or solidity) defined as the ratio between the empty surface and the total surface of the disc. The porosity is determined by different parameters such as the mesh size and the wire diameter (in case of mesh-type disc). The porosity level is strictly related to the induction factor of the disc. Indeed, a higher porosity level implies a lower induction factor. Aubrun et al. [2007] have done a detailed characterisation of the wake generated by an actuator disc in a turbulent isotropic uniform flow. The shape of velocity deficit and turbulence intensity profiles depending on the disc mesh (induction factor) and the distance downstream of the model are discussed. In this study the induction factor of porous disc is obtained by:

$$a = \frac{1}{2}\left(1 - \frac{min(U_w)}{U_\infty}\right) \tag{2.37}$$

where U_w represents the wake velocity and U_∞ the free stream velocity. Figure 2.9 shows the results obtained by Aubrun et al. [2007]. As it can be seen by the analysis of the influence of the downstream position, the near wake region can be considered ended 4 diameters downstream of the disc. Indeed, the velocity deficit profile is characterised by an annular shear layer as well the turbulence intensity profile has an annular distribution up to x/D = 4, where the two shear layers start collapsing. At x/D = 9, in the far wake region, it is interesting to notice that the turbulence intensity reaches values 3 times higher than the free-stream level. As concerns to the influence of the porosity level on the velocity deficit profile, the results show the possibility to control the wake signature of a porous disc by changing its porosity level. In the same study the axial force was calcu-

lated applying the momentum theory to the mean velocity profile downstream the disc in order to retrieve the thrust coefficient and the power coefficient defined as in expressions 2.11 and 2.12 (left side). The values of these coefficients were compared with the values obtained by the use of the induction factor (Expressions 2.11 and 2.12 (right side)) showing a good agreement and so the applicability of this kind of wind turbine physical modelling. Moreover Aubrun et al. [2013] performed wind tunnel experiments to compare the wake of a rotating wind turbine with the wake of a porous disc, in both homogeneous and isotropic turbulent flow conditions and atmospheric boundary layer flow conditions. The results, here not reported for the sake of brevity, confirm that the use of a porous disc (based on the actuator disc concept) as a wind turbine model is satisfactory in terms of far wake reproduction. Indeed, the wake of a porous disc wake developing in the atmospheric boundary layer are indistinguishable from the wake developed by the rotating model after 3 rotor diameters downstream of the rotor disc. In case of turbulent isotropic uniform flow conditions, although the comparison is still satisfactory, some discrepancies are still distinguishable, mainly on the turbulence intensity distribution. A detailed comparison between the near wake of a porous disc and the near wake of a rotating wind turbine model has been performed by Lignarolo et al. [2016]. It highlights the difference in the turbulent mixing of the two kind of wakes.

Mesh number	Mesh size[mm]	Wire diameter [mm]	Porosity level [%]	Induction factor a
1	5	1.3	60	0.185
2	3.75	0.9	65	0.135
3	5.6	1.4	64	0.12
4	5.6	1.12	70	0.11
5	7.1	1.8	65	0.12
6	5	1.8	55	0.195
7	7.1+3.75	1.8+0.9	<55	0.22

Metallic mesh properties. The porosity level is the percentage of the void area to the total mesh area.

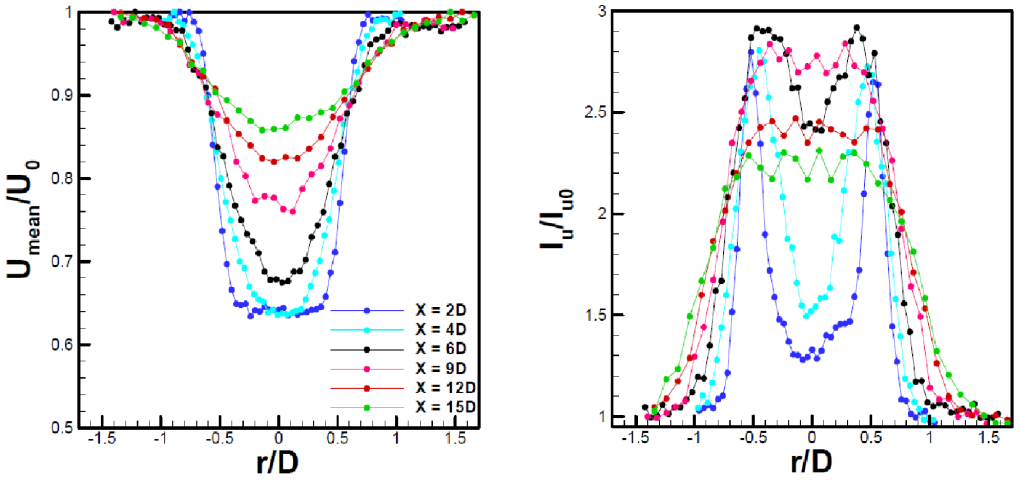

Streamwise velocity and turbulence intensity downstream of a porous disc (diameter 10cm, mesh 6)

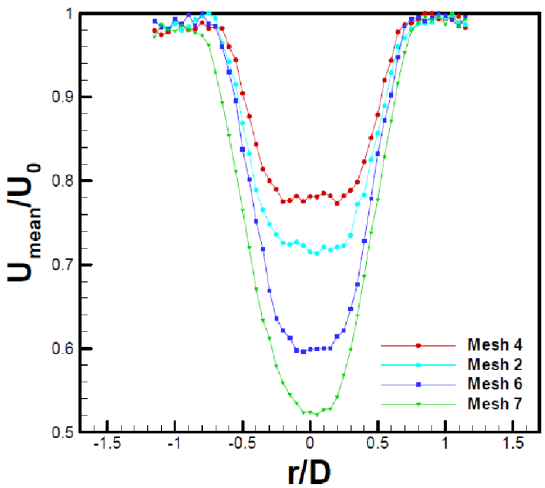

Influence of porosity level on the streamwise velocity at $X = 4D$ downstream of the disc (diameter 20cm).

Figure 2.9 – List of the tested meshes, velocity deficit and turbulence intensity profiles at different distances downstream of the model (top) and effect of the mesh on the velocity deficit (bottom). From Aubrun et al. [2007].

2.2.2 Skewed wake properties

As it can be easily admitted, the wind direction varies more or less frequently depending on the wind farm site. So, a wind turbine is quite often aimed to rotate the nacelle in order to face the wind direction. According to the wind turbine control system, the nacelle position is generally adjusted (if necessary) each ten minutes. Inevitably this can bring to situations of wind turbine misalignment according to the wind direction. This condition obviously brings to a production loss of the yawed wind turbine, but as it will be detailed in section 2.3, this voluntary yaw misalignment is one of the envisaged wind farm control strategies to increase the overall farm production. Knowing that the aerodynamic description of a wind turbine wake is already complex in aligned conditions, this becomes even more complex when a wind turbine rotor is not faced to the wind. Different studies have been performed in order to define a theory or an empirical model capable to properly describe these operational conditions (Mikkelsen and Sørensen [2001], Grant et al. [1997], Grant and Parkin [2000], Medici and Dahlberg [2003], Parkin et al. [2001]). In particular, Zhong and Infield [1991] summarizes the difficulties of a yawed wind turbine modelling. The *Blade Element Theory* is generally used to determine the thrust and power coefficients, nevertheless in case of a yawed rotor, the resulting variations of angle of attack generate some supplementary torque, especially on the vertical and horizontal axis. Consequently BEM theory is not relevant for the estimation of the aerodynamics loads of the rotor because it is not capable to take into account the torques generated by the rotor misalignment, as stated by Smulders et al. [1981]. The analysis of the charge of a misaligned wind turbine has been a topic of interest of different European projects (Schepers et al. [1995], Schepers [1998], Snel and Schepers [1995]). These projects, both via experimental reproduction in wind tunnel and at full scale condition measurements, have yield to the formulation of different empirical laws in order to describe the aerodynamic loads on the blade. Here by analogy with what it was done for the no yawed condition, the momentum theory, the Glauert theory and the vortex cylinder model will be briefly described for a misaligned rotor disc case, as well as all the consequences regarding the wake of a wind turbine in yawed conditions.

2.2.3 Momentum theory for yawed conditions

The flow exerts a pressure force normal to the disc plane. Let's assume that this force is responsible of the rate of momentum variation, and that the induced velocity has to be normal to the disc plane. Considering a disc not perpendicular to the flow direction (Fig.2.10), it is then possible to see that the induced velocity is still normal to the disc plane and therefore, just a component of the induced velocity is parallel to the flow direction. Despite this difference, the wake velocity

is still the double of the induced velocity, assuming that the rate of momentum change is equal.

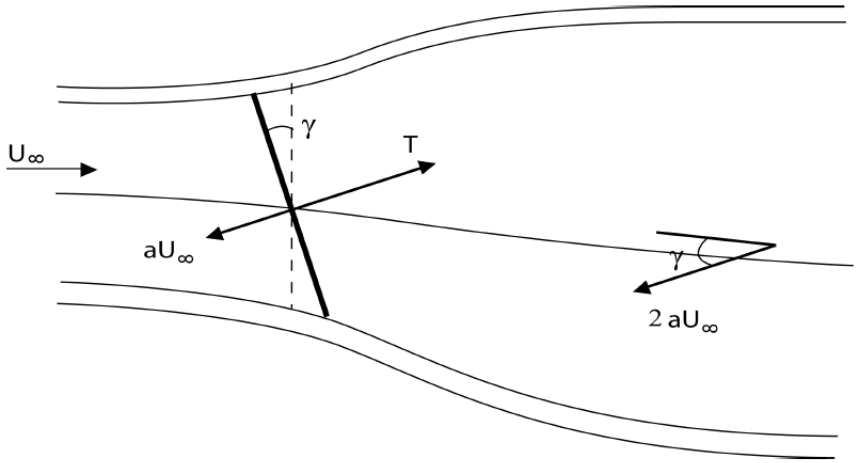

Figure 2.10 – Scheme of a yawed disc stream-tube

By analogy with the considerations done for equation 2.9, it is possible to retrieve the thrust force for a yawed disc:

$$T = 2\rho A_d U_\infty^2 a(cos\gamma - a) \tag{2.38}$$

where A_d is the frontal disc surface and γ the yaw angle. Analogously with equation (2.10) the extracted power will be:

$$P = TU_d = TU_\infty(cos\gamma - a) = 2\rho A_d U_\infty^3 a(cos\gamma - a)^2 \tag{2.39}$$

It is therefore possible to estimate the thrust (Eq.2.40) and power (Eq.2.41) coefficient for yawed conditions:

$$C_T = \frac{T}{\frac{1}{2}\rho A_d U_\infty^2} = 4a(cos\gamma - a) \tag{2.40}$$

$$C_P = \frac{P}{\frac{1}{2}\rho A_d U_\infty^3} = 4a(cos\gamma - a)^2 \tag{2.41}$$

With the same procedure applied in section 2.1.1 the cancellation of the C_P derivative with respect to a gives:

$$a = \frac{cos\gamma}{3} \quad C_{Pmax} = \frac{16}{27} cos^3\gamma \tag{2.42}$$

2.2.4 Glauert theory for yawed conditions

It is worth to notice that the application of the momentum theory on the yawed disc does not give an accurate description of the phenomenon. Indeed, it does not take into account that the transversal pressure gradients concurring to the wake deviation could also contribute to the axial force exerted on the disc by the flow, influencing in this case the induced axial velocity. These considerations brought Glauert to develop a formulation of his model for the yawed condition starting from his studies on the autogyro (Fig.2.11). Basically an autogyro is an aircraft similar to an helicopter: it is composed by a rotor propeller providing the horizontal thrust and a free rotor providing the lift. Thanks to the horizontal velocity provided by the propeller and to its capacity of varying its inclination according to the horizontal direction, the rotor is capable to provide the necessary lift force to sustain the autogyro and a further horizontal thrust. Finally, the lift rotor can be seen as a yawed wind turbine, that varies its yaw angle γ according to the autogyro speed.

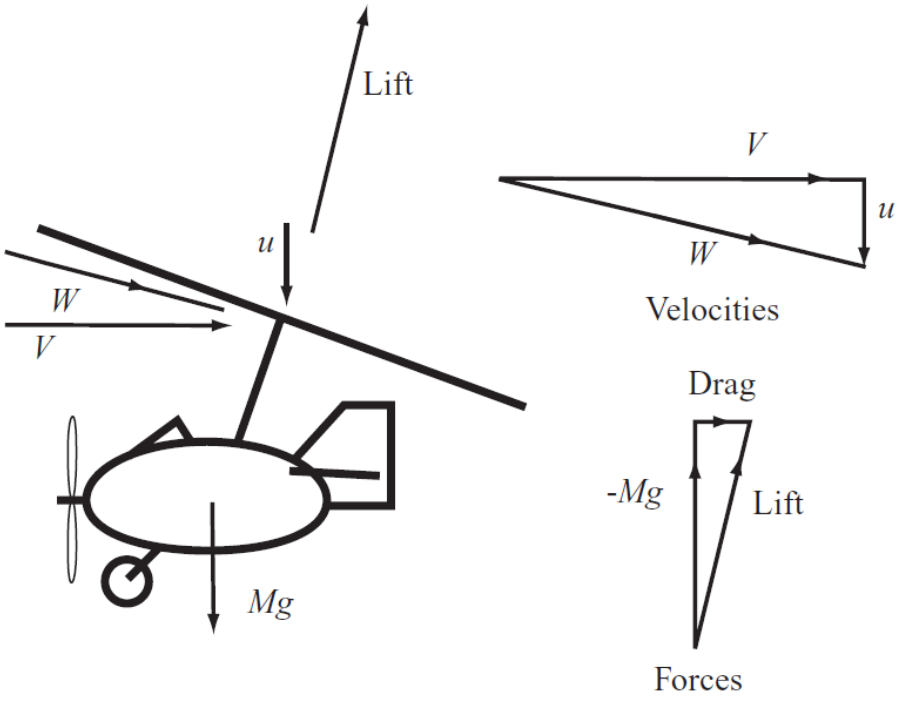

Figure 2.11 – Scheme of the Glauert's autogyro with velocity and force components. From Burton et al. [2011].

It is not the aim of this chapter to give a detailed description of the autogyro that can be found in Burton et al. [2011], but to give below the thrust and power

coefficient (Eqs.2.43 & 2.44) that will be useful for the analysis of the experimental results

$$C_T = 4a\sqrt{1 - a(2cos\gamma - a)} \tag{2.43}$$

$$C_P = 4a(cos\gamma - a)\sqrt{1 - a(2cos\gamma - a)} \tag{2.44}$$

2.2.5 Yawed actuator disc vortex cylinder model

In section 2.1.3, the vortex cylinder model has been described for non yawed conditions showing equivalent results to the momentum theory approach. The interest of vortex cylinder theory is to bring more details on the wake properties and this becomes particularly interesting in case of yawed conditions. The wake of a yawed disc is skewed because of thrust force components perpendicular to the flow. Indeed, being the thrust force perpendicular to the disc, it has necessarily a component perpendicular to the flow in case of yawed conditions. By reaction to these thrust force components, a reaction force in the opposite direction impacts the wake, causing a flow acceleration upwind and sideways. The angle χ between the wake centre line and the rotor centre line is called skew angle, and as shown in figure 2.12, it is greater than the yaw angle γ.

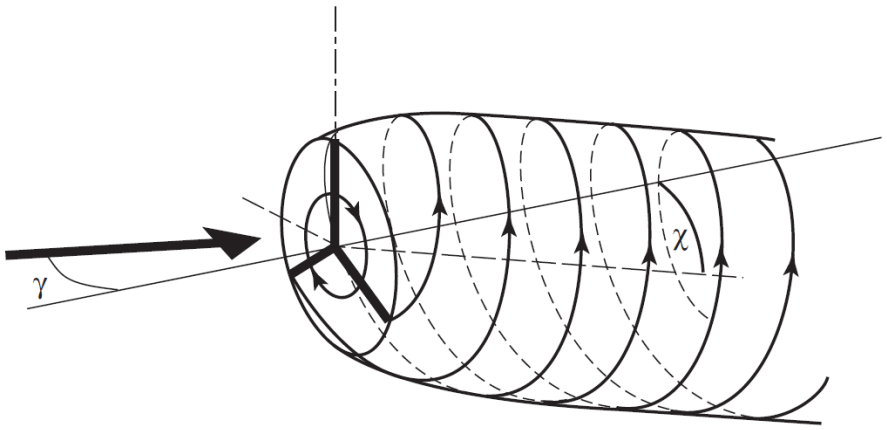

Figure 2.12 – Scheme of the deflected vortex wake for yawed conditions. From Burton et al. [2011].

In order to apply the same model used for the non yawed conditions, it must be assumed that the bound circulation on the rotor disc is radially and azimuthally uniform. As seen before, the angle χ varies continuously for yawed conditions making impossible to have a uniform circulation. Finally, it is necessary to assume

that a small circulation variation around a mean value has a negligible effect on the induced velocity and that, for this reason, the wake motion is principally dominated by the blade tip vortex shedding related to the mean value of the circulation as detailed by Burton et al. [2011]. The radial wake expansion is neglected because, as for the non yawed conditions, it would have been a further complication. Assuming that the mean induced velocity at the disc location is $aU_\infty arcos(\chi/2)$, within a direction that bisects the skew angle χ, the induced velocity will be twice the velocity at the rotor (Fig.2.13 in fully developed wake conditions. Thus, it can be demonstrated a relation between the skew angle χ and the yaw angle γ, depending on the induction factor a (Burton et al. [2011]):

$$\chi = (0.6a + 1)\gamma \tag{2.45}$$

And likewise for the thrust and power coefficient:

$$C_T = 4a(cos\gamma + tan\frac{\chi}{2}sin\gamma - a\sec^2\frac{\chi}{2}) \tag{2.46}$$

$$C_P = C_T(cos\gamma - a) \tag{2.47}$$

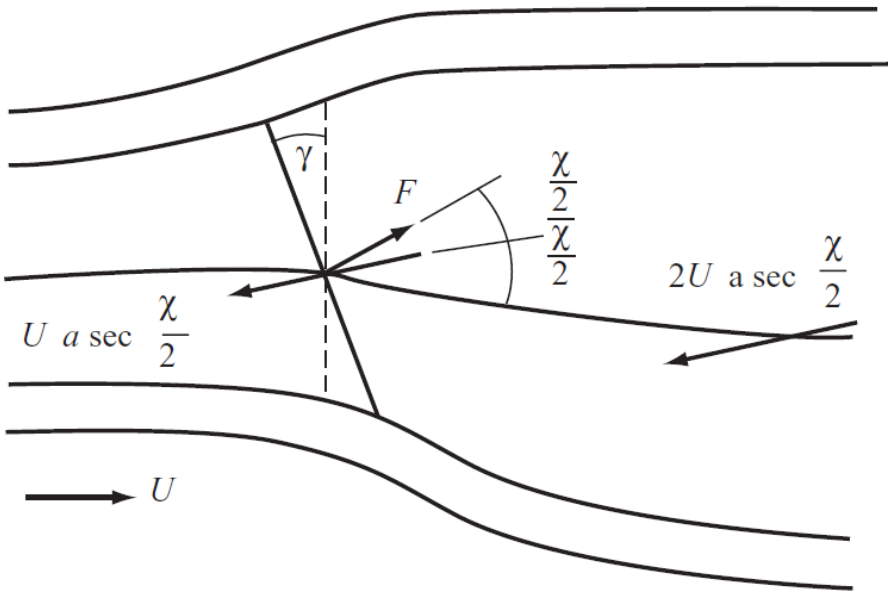

Figure 2.13 – Average induced velocities in yawed conditions. From Burton et al. [2011].

2.2.6 Engineering wake models

In this section, a non-exhaustive description of some wake analytical models is exposed. The interaction between an atmospheric boundary layer (ABL) and a wind farm has been studied in several works (Vermeer et al. [2003], Porté-Agel et al. [2014], Baidya Roy et al. [2004], Kirk-Davidoff and Keith [2008]), showing its effect both in terms of wind farm production management and potential impacts of wind farms on local meteorology. The wake characteristics of a wind turbine in uniform flow has been already discussed in section 2.2.1. Here, the necessary notions to the comprehension of the wake models defined for atmospheric boundary layer conditions will be just provided. The wake of a wind turbine is generally described as a succession of similar distributions for the velocity deficit and the added turbulence intensity profiles as axisymmetric in all the wake sections. However, the terrain characteristics and the wind shear caused by the ABL invalidate the axial symmetry hypothesis. Some velocity deficit vertical profiles retrieved by both wind tunnel experiments and numerical simulations are compared by Vermeer et al. [2003] in figure 2.14. It is possible to notice that the peak of the velocity deficit is not located in correspondence of the rotor center but below, in accordance with the asymmetry due to the ABL. This peculiarity was noticed for the first time by Talmon [1984], that stated the impact of the upstream wind shear and the terrain characteristics on the velocity deficit asymmetry. The velocity deficit evolution downstream a wind turbine has been the focus of different studies in the past years. Indeed, it is a crucial information in order to understand the wake propagation of a wind turbine and its interaction with the other turbines. The first empirical approach used by several authors (e.g.,Magnusson and Smedman [1996, 1999], Baker and Walker [1984], Crespo and Hernández [1986], Högström et al. [1988], Barthelmie et al. [2003], Zhang et al. [2013], Iungo and Porté-Agel [2014], Aitken et al. [2014]) was based on the evolution of the velocity deficit ($VD = U_{hub} - min(U_w)$) as a function of the downstream distance:

$$\frac{VD}{U_{hub}} = A\left(\frac{x}{D}\right)^{-n} \tag{2.48}$$

where U_{hub} represents the reference wind speed at the hub height, x the distance downstream of the wind turbine, D the diameter, A a constant depending on the axial induction factor ($1 < A < 3$). n is generally chosen between 0.75 and 1.25. Equation 2.48 is not the only empirical formulation of the velocity deficit evolution. Magnusson and Smedman [1996, 1999] introduced an other formulation not just based on the downstream distance x but on the transport time $t = \frac{x}{U_{hub}}$:

$$\begin{aligned} \frac{VD}{U_{hub}} &= C_2 \ln\left(\frac{t_0}{t}\right) + C_T \\ t_0 &= C_1 \frac{1}{f_R} \ln\left(\frac{H_{hub}}{z_0}\right) \frac{D}{2H_{hub}} \end{aligned} \tag{2.49}$$

where

f_R: rotor rotation frequency

z_0 : roughness length

H_{hub}: wind turbine hub height

C_T: wind turbine thrust coefficient

$C_1 = 1$ & $C_2 = 0.4$: constants taken from Magnusson and Smedman [1999].

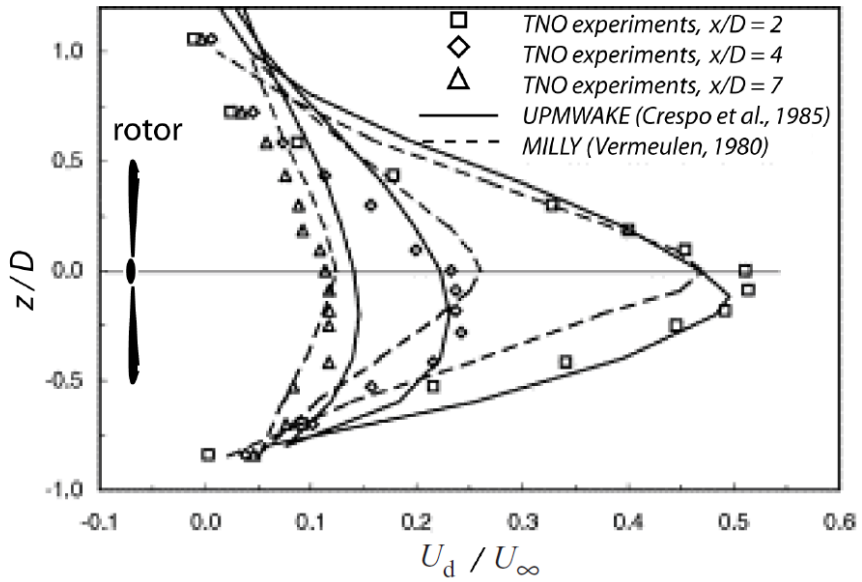

Figure 2.14 – Velocity deficit vertical profile VD (non dimensionalized by the reference wind speed) several distances downstream the rotor. Comparison between wind tunnel experiments (Vermeer et al. [2003]) and analytical wake model (Crespo et al. [1988], Vermeulen [1980]). From Vermeer et al. [2003].

It is interesting to notice that both empirical formulations of the velocity deficit evolution do not take into consideration the ambient turbulence. The authors do not provide any explanation about this choice but, according to the

knowledge on the influence of the ambient turbulence over the wake recovery, it would have been beneficial to introduce this parameter into the empirical models. The aspects related to the turbulence distribution and its effect on the wake propagation and wind turbine loads will not be treated here because not pertinent with the work subject. An interesting review of the principal study concerning the characteristic of the turbulence in the wake has been done by Porte-Agel et al. [2020]. An alternative way to describe the velocity deficit evolution, and in general the wake characteristics, are the analytical models. These are obtained by a manipulation of the flow governing equations and not by fitting of experimental data as the empirical model. Several authors (e.g,Vermeulen [1980], Katic et al. [1986], Larsen [1988], Ainslie [1988], Ott et al. [2011]) studied and developed analytical models in order to describe and predict the wind turbine wake behaviour. Here just the most commonly used in literature (Jensen [1983], Frandsen et al. [2006], Bastankhah and Porté-Agel [2014]) will be shortly described. If interested, a more detailed description and analysis of the analytical wake models can be found in Crespo et al. [1999], Barthelmie et al. [2003] and Göçmen et al. [2016]. The first model briefly described is the one developed by Jensen [1983]. The so-called Jensen model is formulated crossing the application of the conservation mass to a control volume downstream the wind turbine with the use of *Betz theory* (discussed in section 2.1.1) for the determination of a relation between the wind speed just behind the rotor and the thrust coefficient C_T. This model, for reason of simplicity, describes the wake shape (or velocity deficit distribution) as a top-hat distribution. So, according to this model, the mean velocity deficit VD normalised by the mean reference wind speed is given by:

$$\frac{VD(x)}{U_\infty} = \frac{1 - \sqrt{1 - C_T}}{(1 + k_t x/R)^2} \tag{2.50}$$

where C_t the wind turbine thrust coefficient, U_∞ the mean reference wind speed, VD the velocity deficit defined as the difference between the reference speed and the wake speed, x the distance downstream the rotor and R the rotor radius. A particular attention has to be put on the coefficient k_t since it represents the wake growth rate. This coefficient is constant and can be chosen according to the kind of flow. Jensen [1983] suggested an unique value of k_t equal to 0.1 although further successive studies (Barthelmie et al. [2009], Göçmen et al. [2016]) suggested to set $k_t = 0.04 - 0.05$ in offshore conditions and 0.075 in onshore conditions. The wake growth coefficient k_t can be also estimated, as done by Frandsen [1992], according to the ratio between the friction velocity and the streamwise velocity component at the hub height for the incoming ABL flow. This approach applied to a logarithmic ABL profile gives:

$$k_t \approx \frac{0.5}{\ln(z_h/z_0)} \tag{2.51}$$

z_h and z_0 being the wind turbine hub height and the terrain roughness length respectively.

The second model discussed here is the model developed by Frandsen et al. [2006], based on the conservation mass and momentum balance calculated over a control volume containing the wind turbine. This model describes the velocity deficit distribution with a top-hat shape and the normalized velocity deficit is given by:

$$\frac{VD(x)}{U_\infty} = \frac{1}{2}\left(1 - \sqrt{1 - \frac{2C_T}{\beta + \alpha x/D}}\right) \tag{2.52}$$

where D is the rotor diameter, $\alpha \approx 10k_t$ and β is given by:

$$\beta = \frac{1 + \sqrt{1 - C_t}}{2\sqrt{1 - C_t}} \tag{2.53}$$

It is interesting to notice that both models illustrated until now, making the assumption of a top-hat distribution for the wake profiles, underestimate the velocity deficit values at the wake center while overestimate its values at the lateral border of the wake. Bastankhah and Porté-Agel [2014], based on both numerical and experimental data, stated that the wake can be reasonably represented by a self similar Gaussian distribution in far wake positions. According to these observations they assume that the normalized velocity deficit is given by:

$$\frac{VD(x)}{U_\infty} = C(x)exp\left(-\frac{r^2}{2\sigma^2(x)}\right) \tag{2.54}$$

where $C(x)$ is the maximum normalised velocity deficit at the downstream position x, r is the radial distance from the radial distance from the wake center, and σ the wake width. In this case, the wake growth rate is also assumed to be linear. Moreover, this consideration is in accordance with both wind tunnel tests done by Chamorro and Porté-Agel [2010] and numerical simulations done by Wu and Porté-Agel [2011]. So, the wake width normalized by the rotor diameter is given by:

$$\frac{\sigma(x)}{D} = k\frac{x}{D} + \epsilon \tag{2.55}$$

where k is the wake growth rate, and ϵ the value of $\frac{\sigma}{D}$ when x approaches 0. For the sake of brevity, all the steps will be not reported here (see Bastankhah and

Porté-Agel [2014]), but by combining the conservation of mass and momentum with equations 2.54 and 2.55, it is possible to retrieve the original version of the model:

$$\frac{VD}{U_\infty} = \left(1 - \sqrt{1 - \frac{C_T}{8(\sigma/D)^2}}\right) exp\left(-\left\{\frac{y^2}{2\sigma^2} + \frac{(z - z_h)^2}{2\sigma^2}\right\}\right) \tag{2.56}$$

For this version of the model the value of the wake growth k from which depends the values of σ, has to be estimated for each case, and it is considered the same for vertical and lateral wake expansions. The results obtained by Abkar and Porté-Agel [2015] and Xie and Archer [2015] described how the wake width can be influenced in the vertical direction by the ground and thermal stratification, and so can be different form the lateral wake. They pushed to adjust the model in this direction as shown in the following expression:

$$\frac{VD}{U_\infty} = \left(1 - \sqrt{1 - \frac{C_T}{8(\sigma_y\sigma_z/D^2)}}\right) exp\left(-\left\{\frac{y^2}{2\sigma_y^2} + \frac{(z - z_h)^2}{2\sigma_z^2}\right\}\right) \tag{2.57}$$

where σ_y and σ_z are respectively given by:

$$\frac{\sigma_y(x)}{D} = k_y\frac{x}{D} + \epsilon \tag{2.58}$$

$$\frac{\sigma_z(x)}{D} = k_z\frac{x}{D} + \epsilon \tag{2.59}$$

k_y and k_z being the growth rates for the lateral and vertical directions respectively and ϵ defined as before. An exhaustive comparison of the three model briefly described here can be found in Porte-Agel et al. [2020]. The wake models described until now are conceived to properly estimate the far-wake characteristics, so they can be exploited for inter-distances between the wind turbines higher than four rotor diameters. In order to resolve this issue, Blondel and Cathelain [2020] developed a model capable of properly estimate the wake characteristics in both the near wake and the far wake regions. This model, not discussed here for the sake of brevity, is based on a super-Gaussian shape function, evolving from a top-hat shape in the near wake region to a Gaussian in the far wake region.

Wake deflection modelling

As it will be discussed in section 2.3, yaw control strategy are becoming more and more foreseen for wind farm production optimization. For this reason, several studies focused on the analysis of the far wake deflection consequent to the rotor

misalignment (e.g.,Medici and Alfredsson [2006], Fleming et al. [2014], Marathe et al. [2016]), showing an increase of the wake deflection with the distance downstream of the rotor. In both references Jiménez et al. [2010] and Fleming et al. [2014] studies, the increase of the wake deflection with the yaw angle is confirmed. Jiménez et al. [2010] showed that an increment of the thrust coefficient leads to an higher wake deflection. Concerning the incoming turbulence intensity, Bastankhah and Porté-Agel [2016b] showed that the wake deflection decreases in presence of higher ambient turbulent, while Churchfield et al. [2016] and Vollmer et al. [2016] showed that an increment of the thermal stability enhance the wake deviation. These considerations suggest that this control strategy is more beneficial for offshore wind farms and/or stable boundary layer conditions. Concerning the characteristics of the wake in yawed conditions, several studies (Howland et al. [2016], Bastankhah and Porté-Agel [2016b], Churchfield et al. [2016], Wang et al. [2017]) have been done suggesting the presence of a counter-rotating vortex pair in the wake cross-section of a yawed wind turbine (for yaw angle $>20^{\circ}$) giving the wake a kidney shape. Furthermore Fleming et al. [2014], Gebraad et al. [2016], Schottler et al. [2017], Bastankhah and Porté-Agel [2016b] showed that the yawed conditions have effects on both the horizontal and vertical wake displacements. As for the non yawed conditions, different analytical models concerning the yawed conditions have been developed, especially with attention to the lateral wake deflection and the wake deviation angle θ represented in figure 2.15.

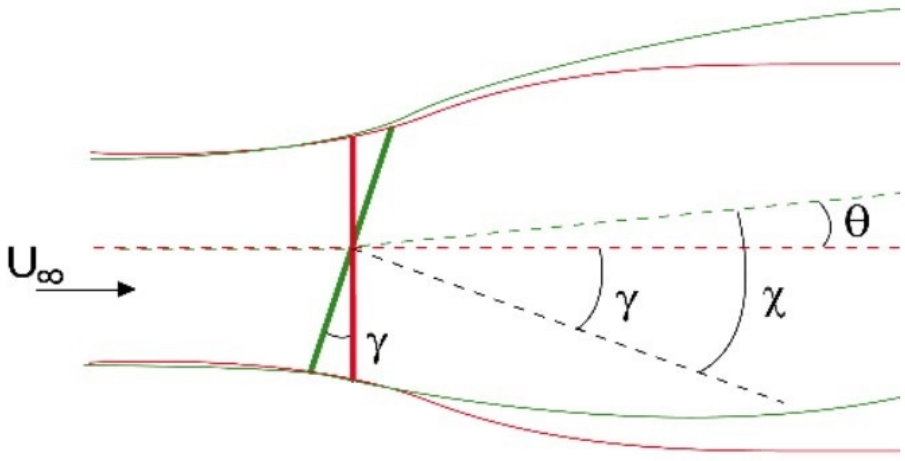

Figure 2.15 – Representation of the skew angle χ, the yaw angle γ and the deviation angle θ.

.

The simplest one derived by the vortex theory, as demonstrated by Burton et al. [2011], assumes a linear behaviour of the the wake deviation angle θ according to the yaw angle:

$$\theta = 0.6a\gamma \tag{2.60}$$

As it can be seen, this model does not consider any influence on the downstream position of the wake, but just the influence of the induction factor a. Jiménez et al. [2010] derived an analytical wake model to predict the wake deviation based on the mass and momentum conservation:

$$\theta \approx \frac{cos^2\gamma sin\gamma \frac{C_T}{2}}{\left(1 + \beta\frac{x}{D}\right)^2} \tag{2.61}$$

where C_T is the wind turbine thrust coefficient in absence of yaw, θ is the wake deviation angle, x the distance downstream of the rotor and β a tunable parameter. This model is valid only in the far wake and the suitable values of β are the object of several discussions in literature (Lissaman [1979], Vermeulen [1980], Katic et al. [1986], Voutsinas et al. [1990]) although the authors in their work found a reasonable agreement with their LES simulations assign to β a range of value between 0.09 and 0.125. It is interesting to notice that this model takes into account the distance downstream the wake such as the value of the thrust coefficient. Bastankhah and Porté-Agel [2016b] developed a model based on the budget study of RANS equations, this model makes a distinction between the near wake and the far wake, here for the sake of brevity, only the far wake formulation is shown:

$$\theta \approx \frac{0.3\gamma}{cos\gamma}(1 - \sqrt{1 - C_T cos\gamma}) \tag{2.62}$$

This model does take into account the thrust coefficient in absence of yaw but does not consider the distance downstream of the wake. These are not the only wake deflection models present in literature, also Gebraad et al. [2016] developed his own model by the combination of the before mentioned work with the Jensen wake model discussed at the start of this chapter. Instead, Shapiro et al. [2018] developed a model based on a lifting line approach. The latter mentioned models will be not discussed here because not used in the rest of the work. It is important to notice that the aforementioned wake deviation models estimate directly the wake deviation angle θ without necessarily estimate the wake center position and then the deviation angle depending on its variation, as usually done in wind tunnel experiments. So this different approach has to be taken into account while comparing the experimental results with the model predictions. Indeed, the wake center determination methodology can significantly affect the wake deviation angle

value. The considerations about the wake center determination methodology will be done in section 3.4.

2.3 Wind farm control

As detailed in (Pao and Johnson [2009]), wind farm control can be actuated concerning the optimization of the electrical power generation quality and grid stability or concerning the study of the reduction of the aerodynamic interactions among the wind turbines in order to reduce the power losses due the wakes. Until now, the wind farm control was mostly focused on the electrical side, but aerodynamic improvement has become more and more studied in the last years (Knudsen et al. [2015], Sanderse [2009]). This interest in aerodynamic interactions is certainly a consequence of wind farm layout densification as mentioned in Chapter 1. Being not treated in this work, the approach concerning the electrical aspects will be not discussed in this review. Regarding the wind farm control oriented on aerodynamic performances, there are two principal strategies: the *induction* control (or power curtailment or down-regulation), consisting in the voluntary down regulation of the upwind wind turbine in order to let more kinetic energy at the downwstream turbines, and the *yaw control* (or yaw offset), consisting in the voluntary yaw misalignment of the upstream wind turbine in order to deviate the wake from the downstream turbines. Both of them have the objective to control the power production of each wind turbine in order to increase the rate of production of the whole wind farm and/or to reduce the total fatigue losses.

2.3.1 Induction control

The induction control (here in after power curtailment) strategy is based on a quite simple principle. As shown by analysis of the wake models treated in section 2.2.6, the signature of the wake is strongly dependent on the thrust coefficient C_T of the wind turbine. So taking into consideration the evolution of the power and thrust coefficients described in section 2.1.1, it is possible to remarkably reduce the thrust coefficient, so the wake intensity, with a slightly reduction of the power coefficient. Indeed, looking at figure 2.3, it is possible to notice that around the *Betz limit* (induction factor a=1/3), the C_P curve is flat while the C_T curve is steep, so a reduction of the induction factor would result in a low reduction of the power coefficient while the diminution of the thrust coefficient would be consistent and so the wake signature lower. Machielse et al. [2008] developed a theoretical model of the power curtailment, modelling the two wind turbines as actuator discs and using *BEM* theory. Results show that the induction factor reduction from 1/3 to 1/5 leads to a gain on the overall production of $\approx$ 4.8 %.

The induction control potentiality has been studied by several authors performing either simulations or wind tunnel experiments in order to characterize this wind farm control strategy (Knudsen et al. [2015]). Generally, these studies report a gain of the overall power production between 4 and 6 % in case of the most disadvantageous wind conditions (full wake interactions) and between 0.5 and 1 % considering all the wind directions. Heer et al. [2014] show the vulnerability of this kind of results highlighting how they are influenced by the wake model chosen in the simulations. Other studies observed the effect of the atmospheric conditions on the power curtailment effectiveness. Indeed, Johnson and Fritsch [2012] show that while for low turbulence intensity level the gain was about 3 %, in case of medium intensity turbulence level the gain dropped to 1 %, becoming negative (-14 %) in case of high turbulence intensity levels. This variability of the performance related on the turbulence level suggest the difficulty to perform full scale tests. In more recent studies, Munters and Meyers [2017, 2018] showed the possibility to increase the wind farm production via a sinusoidal thrust control strategy applied on the first row of wind turbines. Indeed, this strategy seems to accelerate the wake recovery time. A similar approach of this *wake mixing* strategy has been studied by Gebraad et al. [2015] and Frederik et al. [2020]. Furthermore Boersma et al. [2018] developed a control oriented dynamic model called $WFSim$ based on the axial induction dynamic variation.

2.3.2 Yaw control

The yaw control strategy (or wake steering) is based on the voluntary misalignment of a wind turbine according to the wind direction in order to deviate the wake laterally, and so reduce its impact on a downstream wind turbine. The potentiality of this control strategy has been shown by different simulation studies (e.g.Bossanyi and Jorge [2016], Gebraad et al. [2017]) and full-scale tests (e.g.Machielse et al. [2008], Wagenaar et al. [2012], Fleming et al. [2017]). Nevertheless, some issues regarding the correct estimation of the net gains persist. Some studies on the effects of wake steering have been also performed in wind tunnel in order to evaluate the effect of the yaw manoeuvre on the wake position (e.g. Bastankhah and Porté-Agel [2016a], Grant et al. [1997], Howland et al. [2016], Schottler et al. [2018]). These studies, whom results will be partially discussed in chapters 3 and 4, are also interesting as concerns to the wake center determination. Indeed, this latter is a crucial parameter to characterize the wake deflection but there is not a unique approach to its determination as it will be discussed in the next chapter. Fleming et al. [2014] used a computational fluid dynamics tool called $SOWFA$ to simulate the performances of the $NREL$ reference wind turbine (described in Churchfield et al. [2016]). This work highlights the wake rate deflection at different distances downstream of the yawed wind turbine, for example yawing the wind turbine of 35°

the wake at 7D downstream will be deviated of 0.5D. This work also investigates the consequences of the yaw control actuation in terms of loads and fatigue by the use of the software *FAST* (described in Sprague et al. [2015]), showing a reduction between 10 and 20 % of the yawed wind turbine loads against a power reduction higher than 30 %. Concerning the performances of the downstream wind turbine, this is taken into account in a further study of Fleming et al. [2015], with the same tools used previously, and considering a full wake condition (upstream and downstream wind turbine aligned according to the wind direction). The results state a global power production increase of 4.6 % applying a yaw angle of 25° to the upstream wind turbine. Despite the interesting results concerning the power production, it has to be noticed that the downstream wind turbine fatigue loads have been found to increase. This increase in fatigue loads can be explained by the asymmetry introduced by the wake deflection itself. Indeed, the downstream wind turbine passes from a symmetrical full wake condition (almost absent lateral load variation on the blade due to the rotation) to a partial wake condition with the consequent asymmetries. In section 2.2.6, some wake models have been shown, but none of them was "control-oriented". In order to model the wake control strategy the National Renewable Energy Laboratory and TU Delft developed a set of control and optimization tools called *FLORIS*. As shown by Annoni et al. [2018], this tool includes several wake models and wake deflection models and turbine model based on *FAST* C_p/C_t look up tables in order to properly describe the physics. Moreover it has an optimization section, based on the data (SCADA and others) collected and elaborated by the data section, which is capable to perform real-time optimizations to improve wind plant performance. Fleming et al. [2019] and Fleming et al. [2020] compared the FLORIS predictions to the results of a field campaign aimed to evaluate the wake steering. It showed results in agreement with the measurements that reported an overall production gain of 4 % for two closed wind turbines over a 10° wind sector. It is important to notice that *FLORIS* considers both the axial induction and the yaw angle but predicts only the steady-state characteristics of the wake. So, the fact that a downstream wind turbine responds with a certain delay to the control commands applied on the upstream one is not taken into account. This delay may depend on the wind turbine spacing and the flow conditions. In order to solve this problem, Gebraad and Van Wingerden [2014] extended the characteristics of the *FLORIS* model in order to take into account the aforementioned delays. The new model is called *FLORIDyn*. An exhaustive description of *FLORIDyn* application and potentialities can be found in Gebraad et al. [2015].

Finally, most yaw control models proposed so far still give little consideration to the transient process between the non-yawed and yawed conditions. However, analyzing yaw manoeuvre dynamics affords new insights into wake interactions.

This provides the opportunity to estimate the delay between the manoeuvre on an upstream wind turbine and its effect on a downstream one. Analysis of the time lag between the start of yaw motion and the beginning of wake deviation effects at the downstream wind turbine position can inform about the wake advection time. Moreover, tracking wake variation during the yaw manoeuvre makes it possible to compare the manoeuvre duration with the time needed for wake stabilisation in the deviated condition. The same comparisons can be made regarding the effects of the manoeuvre on the global load measured on a downstream wind turbine. Those analyses are very important to implement the proper strategy in the WT controllers. That's why the main objective of the present PhD project is to reproduce the dynamic yaw variation of a wind turbine in order to provide the time response of the wake at the position of a downstream wind turbine. Indeed, a proper knowledge of this dynamic characteristics can be crucial to increase the wind farm control model effectiveness. Some studies are starting to analyse this kind of dynamic parameters, for example Abraham et al. [2020], although with a different dynamics scaling approach and metrics from the ones applied in this thesis (described in chapter 3 and 4), analyses the lag in the wake response observed for dynamic yaw changes. This work shows a qualitative picture of the wake response to a 30° step change in yaw angle using the vortex wake model, demonstrating that it took about 9 rotor revolutions for the wake to fully stabilize.

Chapter 3

Experimental set-ups & methodology

In this chapter, the experimental set-ups, the wind turbine modelling and the methodologies chosen for the wake position tracking and load variation estimation in wind tunnel experiments will be described. Concerning the wind tunnel experiments, three different campaigns were carried out, two in homogeneous isotropic turbulent flow (HIT) conditions and one in Atmospheric Boundary Layer (ABL) conditions. In all the three campaigns, the experimental set-up concerning the control system and data acquisition was installed in an equivalent configuration. For these reasons, the chapter will be organised as it follows. The wind turbine modelling by the use of porous discs will be firstly detailed. Second, the two wind tunnel facilities of the $PRISME$ laboratory with a description of the three test sections used for the experiments and the corresponding flow conditions will be exposed. Then, the yaw manoeuvre scaling methodology will be detailed. At last, the measurement systems and the metrics will be described, namely, the wind turbine wake tracking measurement by the use of Stereo $Particle\ Image\ Velocimetry$ (Stereo-PIV 2D-3C), as well as the wake center determination method. As concerns to the load variations, the acquisition methodology by the use of a 6 Degree of Freedom (DoF) unsteady balance, the data processing and the metrics, will be discussed.

3.1 Porous disc modelling

The porous disc wind turbine modelling has been already exposed in chapter 2. Only the disc properties and the scaling will be presented in this section. This wind turbine modelling approach is broadly used in literature (Muller et al. [2015], Yu et al. [2017], Bastankhah and Porté-Agel [2014], Van Gent et al. [2017]), especially

while operating wind tunnel experiments at very low geometric scales. As full scale reference, it was chosen a 80 m diameter wind turbine with a reference wind speed of 12 ms^{-1}. As concerns the geometrical scaling: for the first campaign in HIT conditions (here in after HIT1), the scale was 1:800, while for the second campaign in HIT conditions (here in after HIT2) and ABL campaign, the scale was 1:320 with a range of Reynolds numbers, based on the rotor diameter, of about 10^4. This led to a diameter D of 0.1 m for HIT1 conditions and of 0.25 m for HIT2 and ABL conditions. The discs were supported by a cylindrical rod reproducing the wind turbine tower, whose the diameter was 0.005 m for HIT1 conditions and 0.01 m for HIT2 and ABL conditions. In all cases, the hub height was settled at 0.25 m. This choice will be detailed in the next sections. Two different kinds of metallic meshes were used in order to reproduce two levels of porosity, and so two different induction factors, defined as in section 2.2.1. In table 3.1, the mesh geometric characteristics as well the porosity levels, the induction factors and the consequent values of the power and thrust coefficients (see equations 2.11 & 2.12) are listed for the two used meshes (here in after P1 and P2). Figure 3.1 shows, as an example, the two porous disc models used for the HIT1 campaign.

Table 3.1 – *Porous disc mesh characteristics .*

	Wire diameter $[mm]$	Mesh width [mm]	Porosity (P) [%]	a	C_P	C_T
P1	1.12	3.55	57	0.16	0.45	0.54
P2	1.25	5.69	67	0.11	0.35	0.40

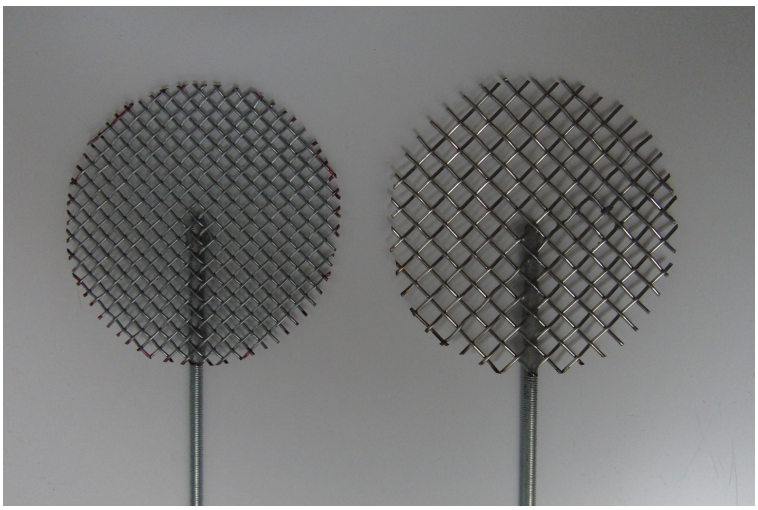

Figure 3.1 – *Porous disc model used for HIT1 campaign (diameter 0.1 m) : P1 disc on the left and P2 disc on the right.*

3.2 Wind tunnel facilities

The experiments were performed in the two wind tunnel facilities of the $PRISME$ Laboratory of the University of Orléans. The first one was an "$Eiffel\ type$" open jet wind tunnel where a fan draws the ambient air and a convergent directs it towards the test section, increasing its speed and dampening the speed fluctuations. The wind tunnel (Fig. 3.2) has a 0.5 m × 0.5 m × 2 m squared test section. At the end of the convergent, an homogeneous geometry turbulence grid is located in order to provide an homogeneous isotropic turbulent flow with a flow speed up to 40 ms^{-1}. The HIT1 campaign was carried out in this facility.

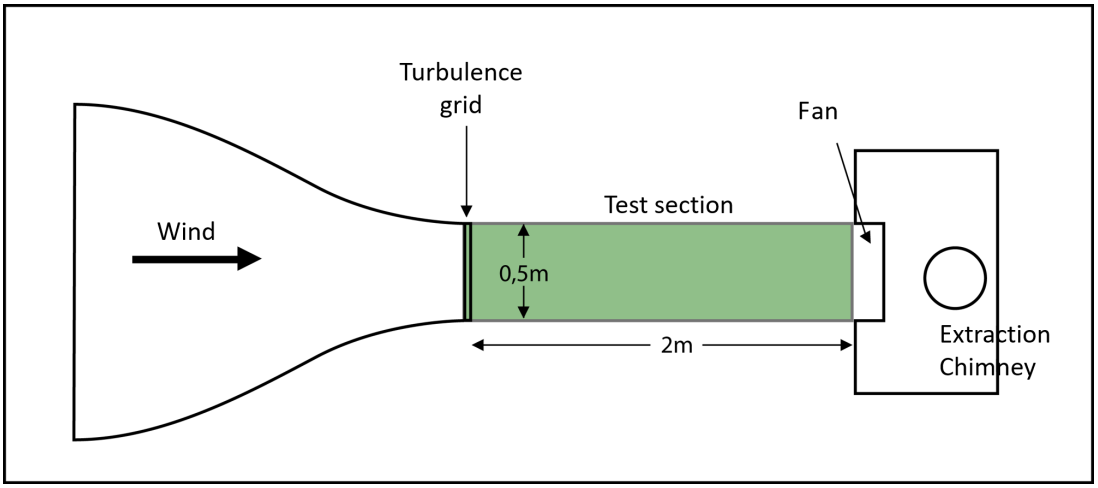

Figure 3.2 – *Scheme of the "Eiffel type" wind tunnel with a squared test section (0.5 m height and width, 2 m length).*

The second wind tunnel is the closed-loop "$Lucien\ Malavard$" wind tunnel shown in figure 3.3. This facility is composed of two test sections: the main test section which is a squared 2 m × 2 m × 5 m section with a maximal flow velocity of 50 ms^{-1} and the return test section that is a squared 4 m × 4 m × 20 m section with a maximal velocity of 12.5 ms^{-1}. In the main test section, the experiments of the HIT2 campaign were carried out, while in the return test section an atmospheric boundary layer was modelled at reduced scale in order to perform tests in ABL conditions.

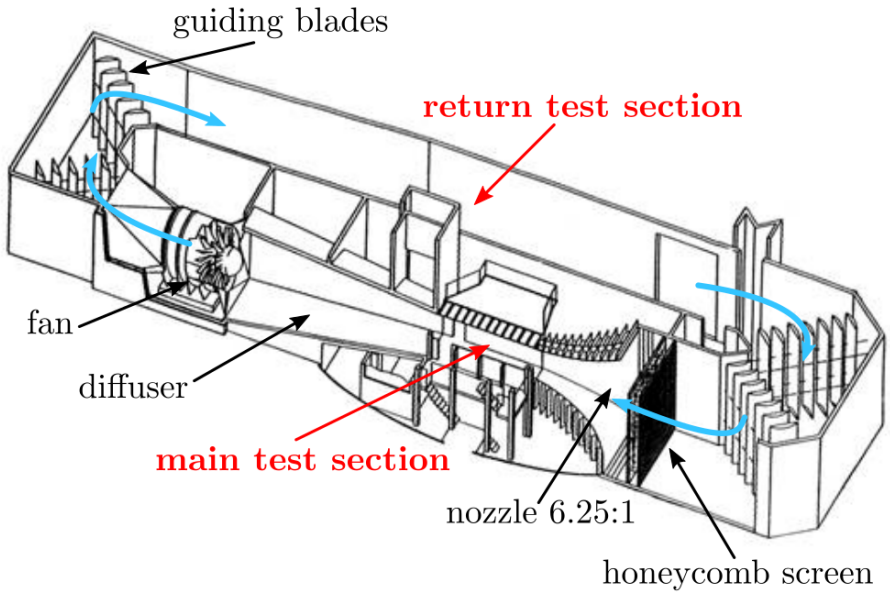

Figure 3.3 – *Scheme of the "Lucien Malavard" closed-loop wind-tunnel of the PRISME Laboratory. From Baleriola [2018].*

3.2.1 HIT1 flow characteristics

The first experimental campaign carried out was the HIT1 campaign. In this section, the flow characteristics in the two test section regions of interest will be exposed. The first region corresponds to the position of the upstream wind turbine, in this campaign located 0.5 m downstream of the turbulence grid. The second region corresponds to the position of either the downstream wind turbine either the PIV measurement plane, located at 0.35 m (3.5D) downstream of the first wind turbine model (this spacing here in after will be defined as ΔX). Figure 3.4 shows a scheme of the load measurement experiments set-up and the regions of interest. Both wind turbine models are located at the center of the test cross (0.25 m). Indeed, since the flow is uniform, there is no need to scale the hub height.

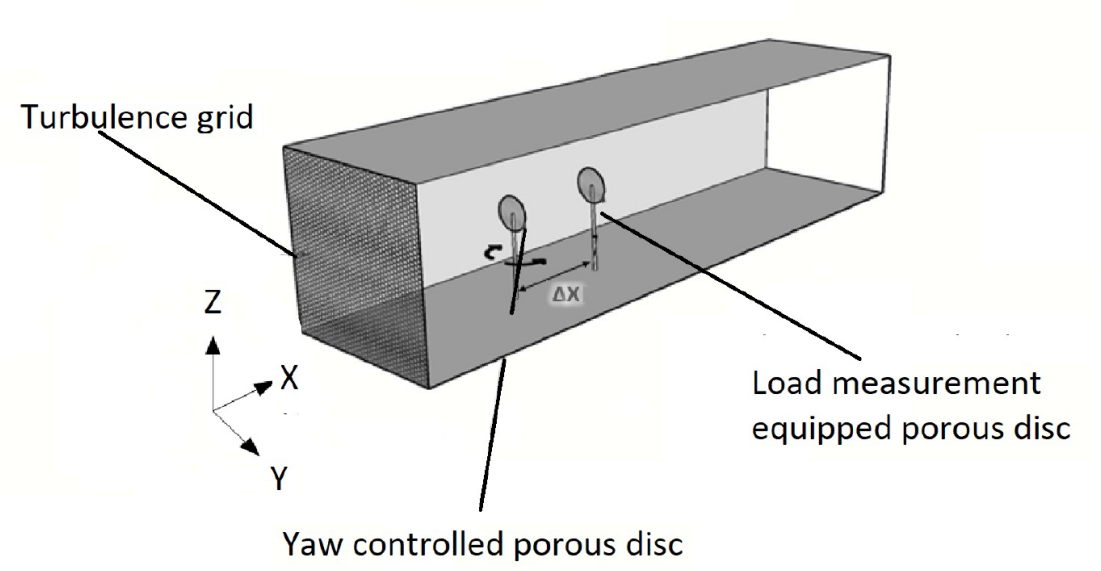

Figure 3.4 – *Set-up of the 6 DOF aerodynamic balance system in the square test section (0.5 m height and width, 2 m length) of the "Eiffel type" wind tunnel.*

The turbulence grid (Fig.3.5) consists in a metal sheet with 14 mm holes distanced of 7 mm. It provides a turbulence intensity level of 4.8 % at the upstream wind turbine location and 4 % at the downstream wind turbine (or PIV plane) location. Experiments were carried out at a reference free stream wind speed (U_{ref}) of 6 ms^{-1}.

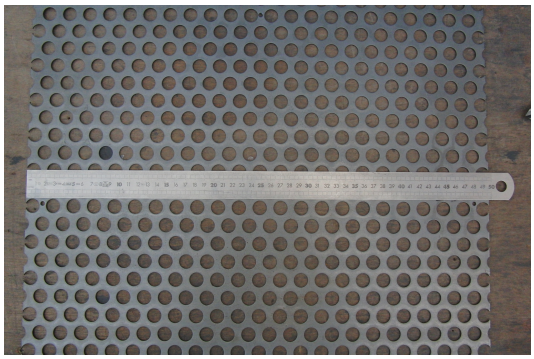

Figure 3.5 – *Photo of the metal sheet turbulence grid: hole diameter of 14 mm, spacing between the holes of 7 mm.*

3.2.2 HIT2 flow characteristics

The HIT2 campaign was carried out in the main test section of the *Lucien Malavard* wind tunnel. The main purpose of this campaign was to verify the absence of Reynolds effects by reproducing the same experiments of HIT1 campaign in different flow conditions. In this case, a turbulence grid (Fig.3.6) was also located at the entrance of the test section. The grid was composed by quadrangular steel bars of 25 mm width (m) and a 100 mm long spacing (M). The grid generated a turbulence intensity of 4.5 % at the upstream wind turbine position (2 m downstream of the grid) and 4.0 % at the downstream wind turbine position (or PIV measurement plane). The spacing (ΔX) between the two wind turbine positions was 1.05 m (4.2D). Experiments were carried out at three different reference free stream velocities of 5, 10 and 15 ms^{-1}.

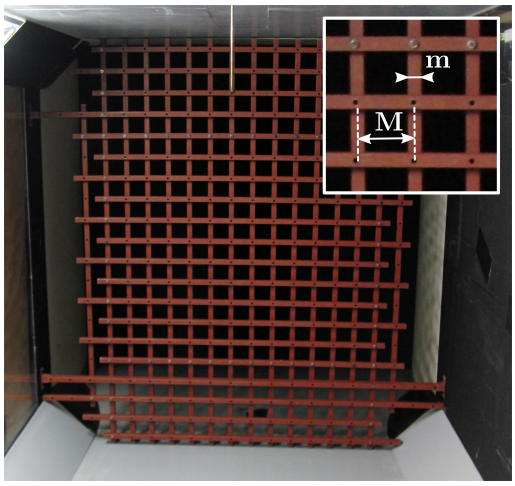

Figure 3.6 – *Photo of the turbulence intensity grid placed at the test section entry of Lucien Malavard wind tunnel.*

3.2.3 ABL flow characteristics

The third experimental campaign was performed in the return test section of the *Lucien Malavard* wind tunnel, which has been adapted as an atmospheric boundary layer wind tunnel. The purpose of this campaign was to reproduce an ABL flow condition in order to evaluate its impact on the yaw manoeuvre effects in terms of both wake and load. The test section conditioning consents to reproduce a neutrally stratified ABL flow with a geometric scale of 1:400. This was possible thanks to a turbulence grid located at the entrance of the return test section, combined with triangular turbulence generators (Fig.3.7). These, together with the installation of a 14 meters development plate composed by perforated steel

sheets, consented the formation of the appropriate turbulence intensity profiles. It is to be mentioned that, despite the return test section size of 4 m × 4 m, the effective test section for the ABL condition is reduced to 3 m width and 1.5 m height.

Figure 3.7 – *Photo of the turbulence intensity grid placed at the return test section entry of Lucien Malavard wind tunnel.*

The ABL properties are in agreement with the common references for this kind of flow (Counihan [1975], Snyder [1981], ESD [1985], VDI [2000]), as it was tested by Muller et al. [2015] in the same wind tunnel configuration at the end of the 14 m development plateau (Fig.3.8). The modelled ABL (geometric scale 1:400) represents a flow above a moderately rough terrain with roughness length of $z_0 = 5.10^{-5}$ m (full scale z_0=0.02 m), a power law exponent of α=0.14 and a friction velocity of u^*=0.29 ms^{-1}.

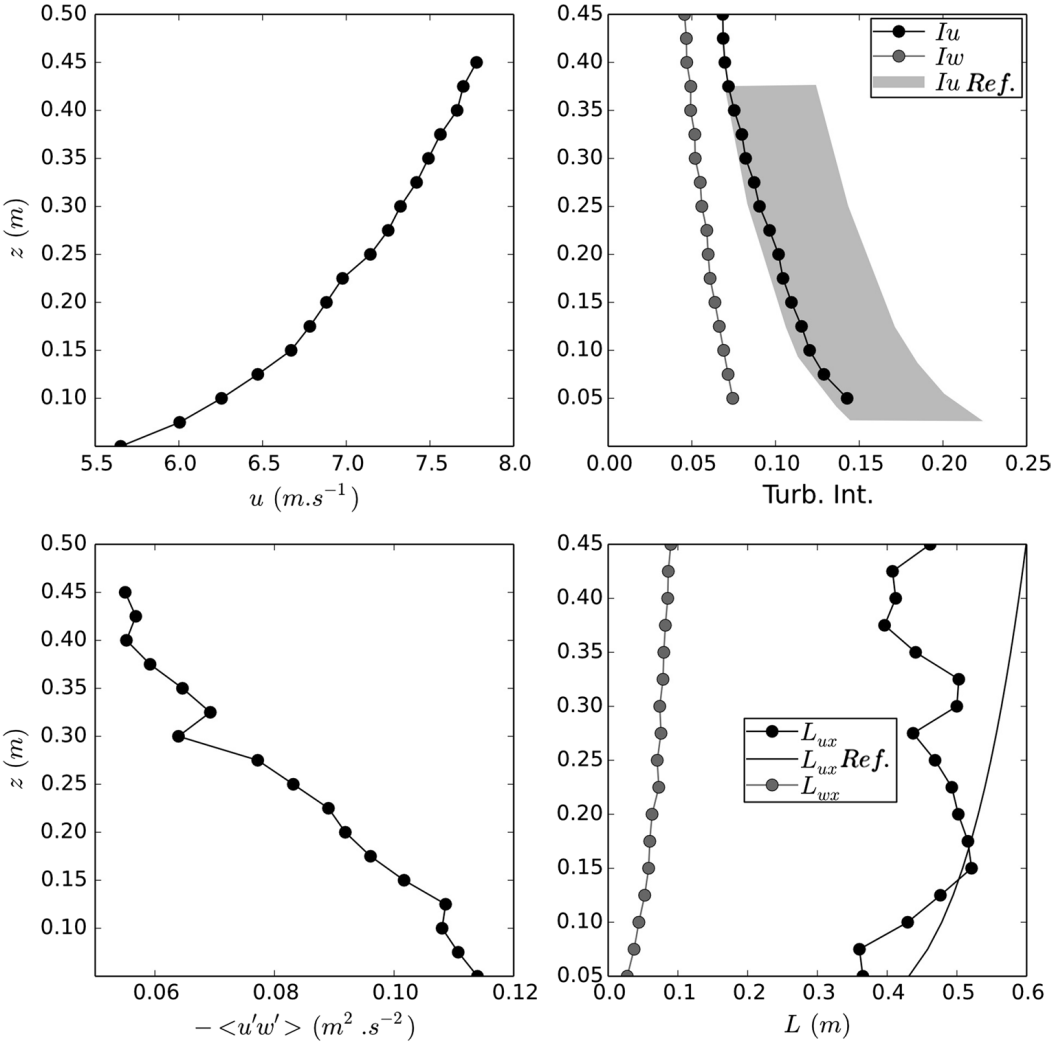

Figure 3.8 – *Vertical profiles of ABL flow conditions. From Muller et al. [2015]. Upper left the mean streamwise velocity u; upper right the streamwise ($I_u = \sigma_u/u$) and vertical turbulence intensities ($I_w = \sigma_w/u$), with the standard range proposed by the VDI [2000] for a moderately rough ABL; lower left the Reynolds stress; lower right Integral scale for the axial velocity component (L_{ux}) and for the vertical velocity (L_{wx}), along with the scaled down reference profile obtained from Counihan [1975] for a roughness $z_0 = 0.02$.*

Experiments were carried out at a reference wind speed (U_{ref}) of 5 ms^{-1} measured at hub height (0.25m) of the upstream wind turbine, located 13 m downstream of the turbulence generator. At this position, the turbulence level was 11 %, as for 4.2 D downstream, where either the second turbine or the PIV

measurement plane were located.

3.3 Yaw manoeuvre scaling

Before discussing the yaw manoeuvre scaling, it is important to introduce the general experimental protocol and the main purposes of the analysis. This work was conceived to analyse the consequences of a wind turbine yaw manoeuvre in terms of both wake deviation at the position of an eventual downstream wind turbine and load variations over a downstream wind turbine. The same methodology and instrumentation were used in all the three experimental campaigns, assuring thus the comparability between the results. The yaw motion of the upstream wind turbine was controlled by a $Kollmorgen AKM24D - ANBNC - 00$ rotational servomotor with speed reducer (ratio 1:32) and measured by a Kubler type 8.5872.3832.G141 circular encoder with a 14-bit resolution. The motion system and the acquisition board were controlled via *LabView*, providing a continuous measurement of the angular position. Figure 3.9 shows the yawing wind turbine configuration for the HIT2 campaign.

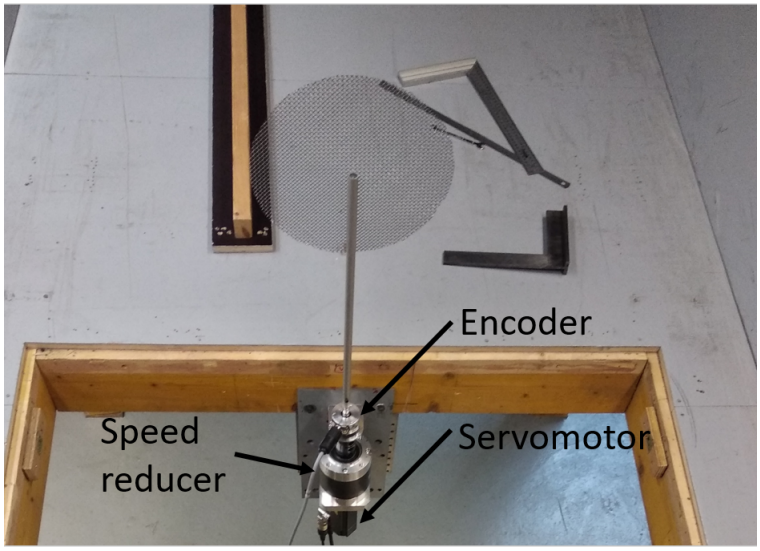

Figure 3.9 – *Photo of yawing disc configuration in the HIT2 campaign set up.*

Firstly, a static yaw variation was reproduced to quantify the order of magnitude of the studied phenomenon in steady conditions. So the wake deviation and the load variation were studied for different static yaw angles γ (see Fig.2.15) of the upstream wind turbine. The values of γ for which the static conditions were studied are from 0° to 30° by step of 10°. As concerns the angle measurement

accuracy, the 14-bit resolution encoder provided a precision of 0.022° that granted the measure repeatability between the campaigns. In case of static yaw angles, there was no need of further scaling apart from the rotor diameter scaling. Different considerations have to be done for the dynamic yaw variation reproduction in wind tunnel. Indeed, in order to properly represent a dynamic yaw angle variation from 0° to 30°, it was taken as reference a full scale commercial wind turbine of 80 m diameter with a wind speed at hub height (U_{ref}) of 12 ms^{-1}, a nominal yawing speed of 0.5 $\circ/s$. Starting from this information, it was possible to retrieve the duration for a 30° yaw manoeuver in both directions. In order to scale this duration, it was necessary to introduce an aerodynamic time scale τ_0 that was derived from a *Strouhal* number based on the reference wind speed at hub height and the wind turbine rotor diameter D ($\tau_0 = \frac{D}{U_{ref}}$). Knowing all the mentioned parameters, the yaw variation duration as a function of the time scale τ_0 was expressed. For the reference full scale conditions, the yaw variation duration calculated was $10\tau_0$. Consequently, the wind tunnel experiments were designed taking into account this scaling factor. Starting from the disc diameter and the wind tunnel reference wind speed, the aerodynamic time scale was retrieved, then the yaw variation speed was adjusted in order to have a 30° yaw variation in $10\tau_0$. In table 3.2, the values of τ_0 are reported as a function of the tested reference wind speed and rotor diameter for all the experimental configurations. There was not founded a difference in the yaw variation duration according to the direction of the manoeuvre (from 0° to 30° or the opposite).

Table 3.2 – *Dynamic yawing scaling parameters.*

Set-up	D $[m]$	U_{ref} $[ms^{-1}]$	τ_0 s
Full scale	80	12	6.66
HIT1	0.10	6	16.6×10^{-3}
HIT2a	0.25	5	50×10^{-3}
HIT2b	0.25	10	25×10^{-3}
HIT2c	0.25	15	16.6×10^{-3}
ABL	0.25	5	50×10^{-3}

3.4 Wake measurements and wake center position determination

3.4.1 PIV system and setup

As mentioned before, the wake tracking measurements were done by the use of *Stereo Particle Image Velocimetry* (Stereo-PIV 2D-3C). This technology consents to estimate the three dimensional velocity components over a two dimensional measurement field. The used PIV system is composed of a Nd: Yag laser Evergreen 200 ($2 \times 200\ mJ$) emitting 532 nm wavelength pulse with a frequency of 2.5 Hz in case of non-synchronized acquisitions. The laser is installed in order to generate a light sheet crossing transversely the test section (yz measurement plane). Seeding particles are micro-sized olive oil droplets sprayed by a PIVTEC seeding system. The image acquisition is performed by two *LaVision Imager LX* cameras (4032 $px \times 2688\ px$) with 105 mm lens. The cameras are equipped with a 532 nm wavelength filter in order to filter out the laser pulsing frequency. Moreover a standard *LaVision Scheimpflug adapter* is used for both cameras because of their oblique installation according to the measurement plane. Figure 3.10 shows the scheme of the $Stereo - PIV$ set-up installation for HIT1 and HIT2 configurations while figure 3.11 shows a photo of the ABL configuration set-up.

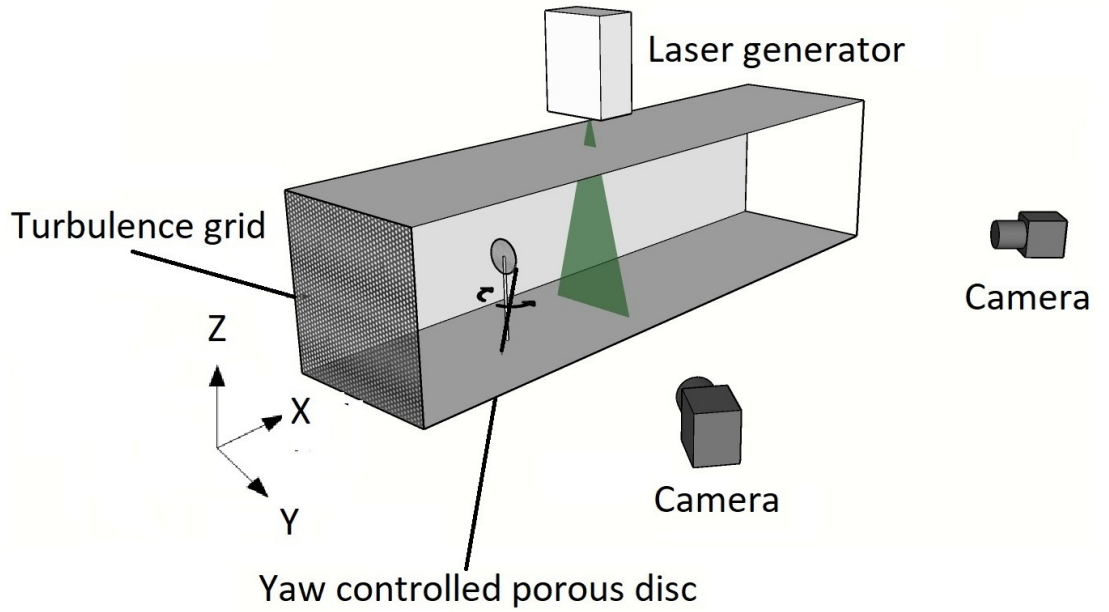

Figure 3.10 – *Scheme of the Stereo − PIV set-up for HIT1 and HIT2 campaign configuration.*

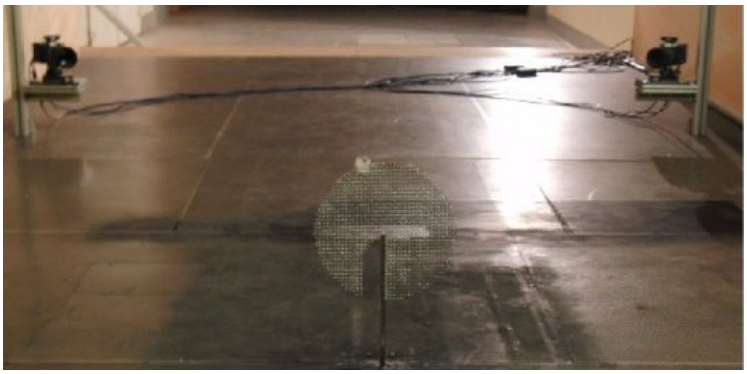

Figure 3.11 – *Photo of the Stereo – PIV set-up for ABL campaign configuration.*

As it can be seen the installations are equivalent although, for logistic reasons, the cameras' position was changed for ABL conditions. The image post processing, such as their acquisition, are done via $DaVis8.3$ software. The images are processed setting a multi pass decreasing size (64 px × 64 px, 32 px × 32 px) interrogation window with an overlap of 50 %. The time delay Δt between the images is settled according to the flow speed. The original vector resolution is defined as the distance between two vectors, and it is the same in the transverse (Δy) and vertical direction (Δz). To each velocity field, after being post processed, a bilinear interpolation on mesh with a twice finer resolution of the original PIV resolution is applied. The obtained vector resolution is divided by the rotor diameter, giving a dimensionless vector resolution $R_v = \Delta y/D = \Delta z/D$. The reconstructed velocity field sizes vary depending on the configuration. For the sake of simplicity, a rectangular mask is usually applied to the original trapezoidal field. In table 3.3, the field sizes divided by the rotor diameter ($b = base/D$ and $h = height/D$) are shown for all the configurations, as well as the time delays Δt, the reference wind speed U_{ref} and the vector resolution Rv_v.

Table 3.3 – *Stero-PIV parameters.*

Set-up	U_{ref} $[ms^{-1}]$	b	h	Δt $[\mu s]$	R_v
HIT1	6	≈ 3	≈ 2.3	105	8.5×10^{-3}
HIT2a	5	≈ 2.5	≈ 1.3	126	5×10^{-3}
HIT2b	10	≈ 2.5	≈ 1.3	84	5×10^{-3}
HIT2c	15	≈ 2.5	≈ 1.3	42	5×10^{-3}
ABL	5	≈ 2.9	≈ 1.4	126	5×10^{-3}

Regarding the acquisition protocol, it varies depending on the measurement

conditions. In case of static yaw conditions, an ensemble-averaging of a given number of samples N_b acquired with a 2.5 Hz sampling frequency was done, while in case of dynamic yaw, PIV acquisitions were triggered according to the yaw motion evolution. Time delays of multiples of the aerodynamic time scale τ_0 were applied to the PIV trigging system from the start of the yaw manoeuvre in order to perform a conditional averaging of the collected velocity fields. The time delays were varied form $3\tau_0$ to $20\tau_0$ in order to be able to reconstruct the phase-averaged evolution of the wake deviation consequent to a dynamic yaw variation. Regarding the estimation of the maximal statistical uncertainty, it was chosen the approach introduced by Benedict and Gould [1996] assuming that the probability density function of velocity fluctuations follows a normal law. As a consequence, the maximal uncertainty of the mean velocity and its standard deviation can be retrieved as it follows:

$$\epsilon_u = \frac{Z.I_{Umax}}{\sqrt{Nb}} \tag{3.1}$$

$$\epsilon_\sigma = \frac{Z}{\sqrt{2Nb}} \tag{3.2}$$

where Z corresponds to the confidence interval of 95% (Z=1.96), Nb is the number of independent samples (acquired images) and I_{Umax} the maximal turbulence intensity measured in the wake region. As it was mentioned while describing the wind tunnel configurations in section 3.2, a turbulence intensity measure was also done in an empty field (no disc installed) at the upstream disc location (I_{Uup}) and at Stereo-PIV measurement location (I_{Udown}). The turbulence intensity values, as well as the spacing between the upstream wind turbine and the wake measurement location Δx, the number of samples N_b and the maximal statistical uncertainties are collected in table 3.4.

The last step applied to the averaged velocity field was a correction of the stream-wise velocity measurements along the transverse direction in order to reduce the potential presence of transverse inhomogeneity. Being $U(y, z)$ the measured velocity field, it is possible to define a free stream region as the external region in which there is no presence of the disc wake signature in the measurement plane. Figure 3.12 shows an example of velocity field for HIT1 configuration in static conditions. The free stream region is defined for $Y/D < -1$ and $Y/D > 1$, the average of these values, if applied on a field without the presence of the disc, gives $U_{ref-emptyfield}$, and if applied in presence of the disc as in figure 3.12, gives $U_{ref-disc}$.

Table 3.4 – *Experimental configuration parameters: spacing Δx, reference scaled wind speed U_{ref}, upstream turbulence intensity I_{Uup}, downstream turbulence intensity I_{Udown}, maximal turbulence intensity in the wake region I_{Umax}, number of samples Nb, maximal statistical uncertainty on the mean velocity ϵ_u, maximal uncertainty on the standard deviation ϵ_σ*

	Δx $[m]$	U_{ref} $[ms^{-1}]$	I_{Uup} [%]	I_{Udown} [%]	I_{Umax} [%]	Nb	ϵ_u [%]	ϵ_σ [%]
HIT1	$3.5 \times D$	6	4.8	4	12	300	1.6	9
HIT2 a	$4.2 \times D$	5	4.5	4	12.6	300	1.4	8
HIT2 b	$4.2 \times D$	10	4.5	4	10.5	300	1.2	8
HIT2 c	$4.2 \times D$	15	4.5	4	13.2	300	1.4	8
ABL	$4.2 \times D$	5	11	11	16	1000	1	4

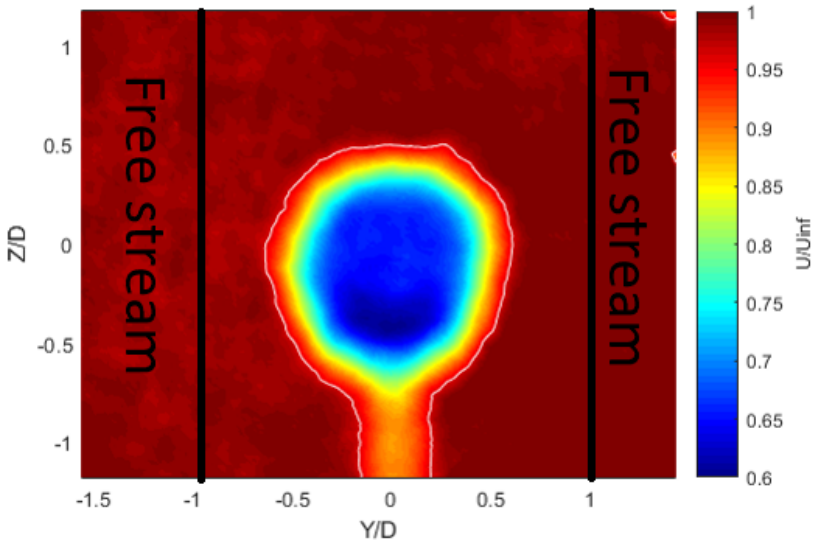

Figure 3.12 – *Example of Stereo-PIV velocity field for HIT1 configuration in static condition $\gamma = 0^\circ$. The vertical black lines represent the boarder of the free stream region. The values of this region are averaged to determine $U_{ref-disc}$ and $U_{ref-emptyfield}$ whether the disc is present or not.*

At this point, knowing the velocity field without disc ($U_{empty}(y, z)$), it is possible to retrieve the velocity deficit $\Delta U_{treated}$ defined as:

$$\Delta U_{treated} = U - \frac{U_{empty}}{U_{ref-emptyfield}} \times U_{ref-disc} \tag{3.3}$$

The treated velocity field $U_{treated}$ can be found as it follows:

$$U_{treated} = U_{ref-disc} + \Delta U_{treated} \tag{3.4}$$

Figure 3.13 shows an example of this procedure applied on a static case ($\gamma = 0^{\circ}$) for HIT1 condition. A one-dimensional velocity profile of the streamwise velocity U is retrieved at hub height. The velocity U is normalized by the reference wind speed $U_{ref-disc}$ while the transverse position is normalized by the disc diameter D. As it can be seen, for the not treated velocity field, the asymmetry between the left and the right side is more marked.

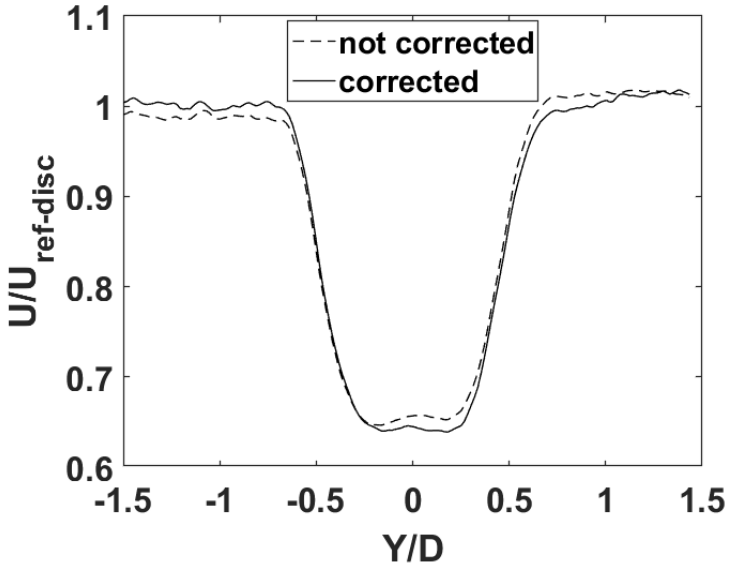

Figure 3.13 – *Example of Stereo-PIV velocity field transverse correction for HIT1 configuration in static condition $\gamma = 0^{\circ}$. The figure shows dimensional profiles centered at the porous disc hub height. The velocity U is normalized by the reference wind speed $U_{ref-disc}$, while the transverse position is normalized by the disc diameter D.*

3.4.2 Wake center position determination

The wake deviation is determined by the estimation of the displacement of the wake center position Y_c. Thus,the wake deviation angle θ can be easily retrieved by simple trigonometric considerations (Fig.3.14). These parameters are linked by the relation

$$\chi = \gamma + \theta = \gamma + \arctan\left(\frac{\delta}{\Delta x}\right) \tag{3.5}$$

where χ is the skew angle of the wake, γ is the yaw angle and Y_c^I represents the position of the wake center after yaw variation.

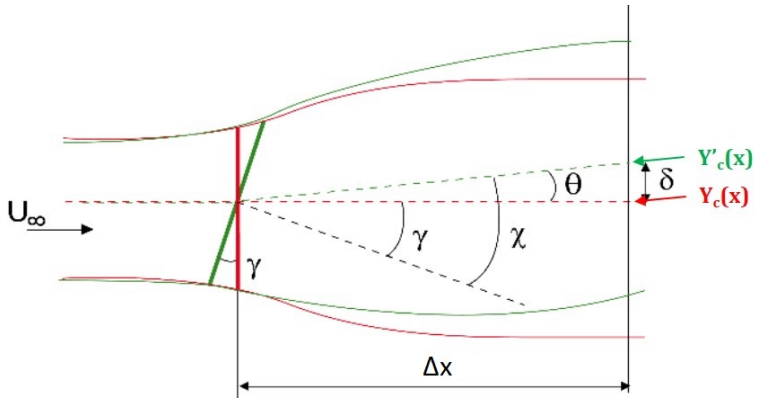

Figure 3.14 – *Representation of the skew angle χ, the yaw angle γ and the deviation angle θ.*

Regarding the determination of the wake center position Y_c, different methods can be applied. For the sake of brevity, only the most common ones will be described and, for a part of these, some examples of their application for processing the experimental results will be shown, in order to select one of them. The first method used was the one developed by Parkin et al. [2001]. This method consists in the determination of the edges of the wake according to the velocity deficit level (e.g. 96 % of the free stream velocity). The position of Y_c corresponds to the median of the segment [AB] in the case of $\gamma = 0^\circ$ and to the median of the segment [A'B'] in the misaligned case (Fig.3.15).

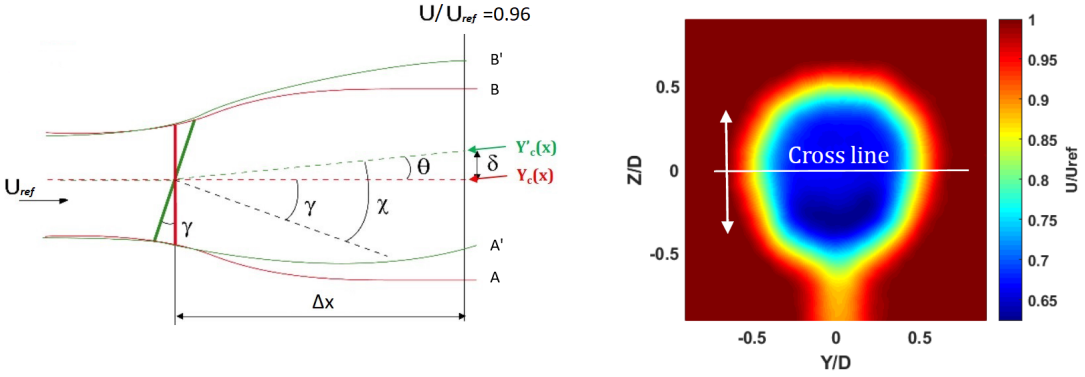

Figure 3.15 – *Example of the wake center determination by the use of Parkin method (Parkin et al. [2001]). On the right, the wake center determination, on the left the velocity profile extraction from the stream-wise velocity field.*

This method is based on a one-dimensional approach, this means that the choice of the vertical position of the velocity profile (cross line in Fig.3.15 right) could affect the determination of the wake center. Indeed, the retrieved wake center position is not an expression of a "global" measure from the entire two-dimensional velocity field, but it is retrieved by the analysis of a cross line, which can be affected by the choice of the line (generally the line is chosen at the hub height). Because of the aforementioned reasons, although it has been used in a preliminary campaign of this PhD project not discussed in this manuscript (Macrì et al. [2018]), this method was not applied for the campaigns presented here. Another method is the one developed by Howland et al. [2016]. This method is based on the determination of the "center of mass", and can be applied on the plane Y, Z. In this case, the coordinates of the wake center Y_c and Z_c are:

$$Y_c = \frac{\iint y\Delta U dydz}{\iint \Delta U dydz} \;\&\; Z_c = \frac{\iint z\Delta U dydz}{\iint \Delta U dydz} \tag{3.6}$$

where ΔU is the streamwise velocity deficit ($\Delta U = U_{ref} - U$). The integration is performed over the entire velocity field. This method could also be applied on a one-dimensional velocity profile by a 1D integration in the y direction at a given z position:

$$Y_c(z) = \frac{\int y\Delta U dy}{\int \Delta U dy} \tag{3.7}$$

A third possible method evaluated for the analysis of the results was the one developed by Muller et al. [2015]. This method is a weighted average of the velocity deficit position y where the weighting is chosen as the exponential of the instantaneous local streamwise velocity deficit ΔU defined as before (Eq.3.8). This method was conceived by the author to be used as one-dimensional method (the average is thus calculated at the center of the disc height z), and so, it leads to the same problems as those of the Parkin method.

$$y_c(z) = \frac{\int y\ exp^{\Delta U}\ dy}{\int exp^{\Delta U}\ dy} \tag{3.8}$$

It has to be mentioned that this method can easily be adapted to be used on a two-dimensional velocity field in order to determine both coordinates of the wake center in the plane Y, Z:

$$Y_c = \frac{\iint y\ exp^{\Delta U}\ dydz}{\iint exp^{\Delta U}\ dydz} \;\&\; Z_c = \frac{\iint z\ exp^{\Delta U}\ dydz}{\iint exp^{\Delta U}\ dydz} \tag{3.9}$$

The last method evaluated was the one developed by Vollmer et al. [2016] based on the estimation of the available wind power of a potential downstream wind turbine. The available specific power (P_{av}) is calculated over a rotor swept area as in equation 3.10, where u is the stream-wise velocity component over a plane normal to the flow direction. Not considering air density variation, P_{av} is normalised by the air density. The available power is calculated for all the possible rotor positions in the ranges of $-0.5D \leq y_0 \leq 0.5D$ and $-0.2D \leq z_0 \leq 0.2D$. The wake center position is then determined by the values of y_0 and z_0 that minimize the available specific power: $Y_c = y_0(minP_{av})$ and $Z_c = z_0(minP_{av})$.

$$P_{av}(y_0, z_0) = \frac{1}{2} \iint u^3(y,z)dydz \quad (y-y_0)^2 + (z-z_0)^2 \leq \left(\frac{D}{2}\right)^2 \tag{3.10}$$

For the sake of completeness, it has to be mentioned that other methods based on the assumption of a gaussian shape of the wake can be applied such as the one tested by Coudou et al. [2017]. This method was not tested because of the non symmetric shape of the skewed wake, as it can be noticed in figure 3.13.

As a general approach, it was chosen to consider only the methods that exploit all the velocity field and not only a cross lines for two main reasons: to have a value representative of the entire wake, and to evaluate the importance of the vertical variation of the wake center position. This criteria narrow down the choice between the "2D formulation" of *Muller* and *Howland* methods together with the *Vollmer* methodology. Figure 3.16 shows an example of the application of these three methods to the HIT1 configuration for the static wake deviation of the P1 disc. As it can be seen, there is a remarkable difference between the results obtained by the *Muller* method and the others. It seems that this approach underestimates the wake deviation compared to the other methods. These reason could be found in the fact that Muller method puts more weight on the minimum of the velocity deficit than the others (due to the weighting with exponential of velocity deficit). This method would be more similar to a gaussian-shape fit method, where the wake center is directly associated with the position of the minimum of velocity (or maximum of velocity deficit).

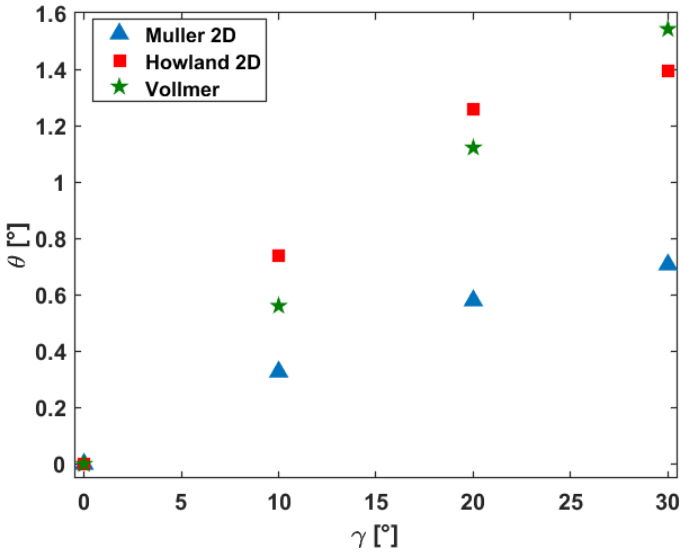

Figure 3.16 – *Comparison between Muller, Howland and Vollmer wake center determination methods for the static results of the HIT1 campaign for porosity P1. γ represents the disc yaw angle and θ the wake deviation angle.*

The discrepancies between *Howland* and *Vollmer* methods are smaller, giving the same order of magnitude to the phenomenon. Looking more in detail, the possible causes of discrepancies can be linked to the choice of the integration domain. Indeed, the *Vollmer* method considers an integration domain of the disc size that is displaced along the velocity field looking for the point of minimum available power, while the other two methods consider the entire velocity deficit domain. This should not be a priori a source of problem because the velocity deficit (part of the integrand) out of the disc signature should be null by definition, and so, there should not be a contribution of the free stream region to the result of the integral. Nevertheless it could happen that, due to the lower quality of the PIV images at the borders of the field and to the approach used to the determination of the reference speed U_{ref} (see Fig.3.13) and also to the local turbulence intensity that generates a residual scatter on the velocity statistics, an undesired and no-physically justified contribution of this part of the velocity field biases the results. In order to avoid this possible source of bias, it was chosen to retrieve the wake center by the use of the method based on the specific available power. As mentioned before, this methods consents to retrieve both the wake center coordinates. Nevertheless, the vertical wake position variation can be neglected in this study. Indeed, Figure 3.17 shows a comparison between the transverse wake position variation Y/D and the vertical wake position variation Z/D, both normalized by the disc diameter D. As it can be seen, the vertical displacement does

not have a clear trend and moreover the order of magnitude of its values is less than 0.01 times the rotor diameter.

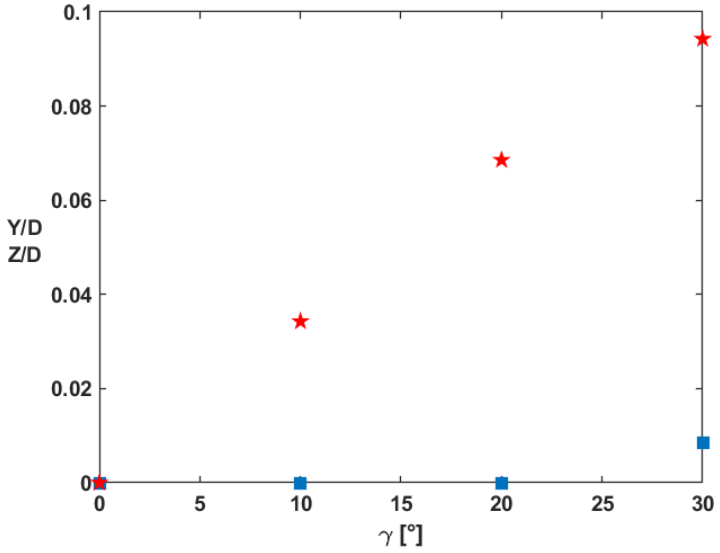

Figure 3.17 – *Comparison between vertical and transverse wake position variation for the static results of the HIT1 campaign for porosity P1.*

As concerns measurement uncertainties, taking into account the uncertainties on the wind speed, the PIV vector resolution (see Tab.3.4) and the methods used to estimate the wake center, it was possible to estimate the maximal measurement error for both set-ups by applying usual resolution-based error estimation methods. The estimated measurement uncertainty is θ=$\pm$0.07° & Y_c = $\pm 4.2\times10^{-4}m$ for HIT1 conditions and θ=$\pm$0.04° & Y_c = $\pm 6.5\times10^{-4}m$ for HIT2 and ABL conditions.

To complement the local indicator of wake deviation, which is the wake center position, the more integrated indicator provided by the above available wind power density at the downstream WT model location $P_{avd} = P_{av}(\Delta x, y = 0, z = 0)$ was also used. This metric is interesting to analyze, because it is a good intermediate between the wake deviation of the upstream WT model and the load response of the downstream WT model, when it is located at the same position as the PIV measurement plane.

3.5 Load variation measurements

The load measurements were performed by an unsteady 6-component aerodynamic balance, $ATI^{TM} modelmini40$. The balance was mounted on a rigid structure lo-

cated underneath the test section floor, and the downstream wind turbine model was installed on a specific designed support. The balance has 6 analogical channels that, such as for the encoder measuring the yaw variation, are acquired at a frequency of 2 kHz by a National Instrument card. The whole system is controlled by *Labview*. Figure 3.18 shows an example of the balance measurement set up for HIT2 conditions.

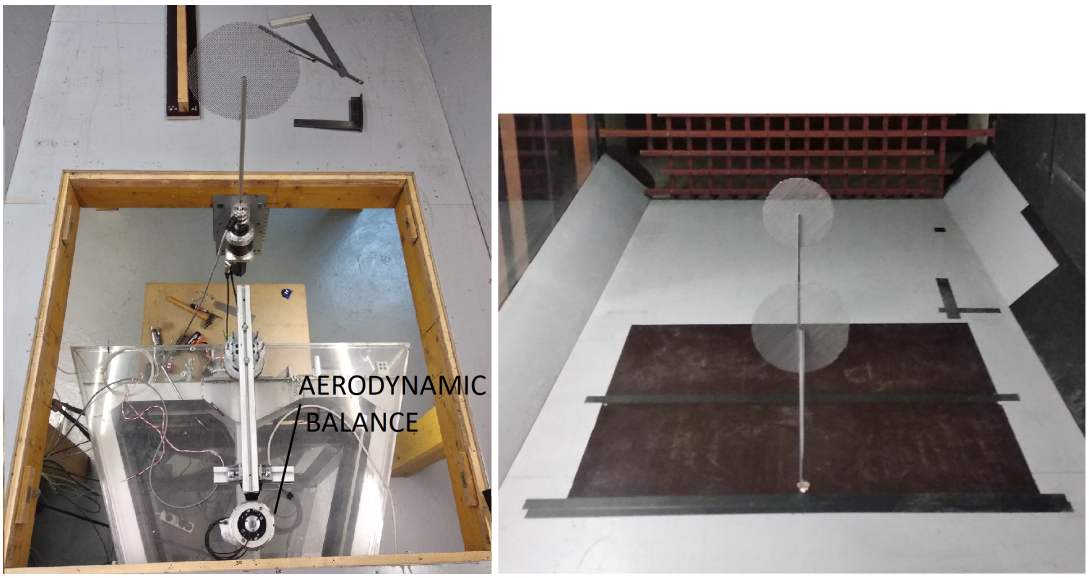

Figure 3.18 – *Example of the HIT2 set-up for the load variation measurements. Balance installed over the rigid support (left), operational conditions with downstream wind turbine mounted on the balance (right).*

The purpose of load variation analysis is their evaluation for the downstream wind turbine undergoing a yaw manoeuvre of the upstream wind turbine. Multiple considerations concerning aerodynamic aspects and the balance characteristics brought to focus the analysis on the thrust coefficient C_T variation. Indeed, this parameter is a direct and reliable indicator of the charge of a wind turbine, such as that one of an actuator disk. Due to the balance resolution and sensitivity, it was chosen to retrieve the thrust coefficient C_T (Eq. 3.11) by the measurement of the moment on the transverse axis T_Y, where ρ is the air density, U_{ref} the free stream speed, S_d the disk surface and b the lever arm.

$$C_T = \frac{T_Y}{0.5\rho U_{ref}^2 S_d b} \tag{3.11}$$

Moreover, since the principal aim of the study is to evaluate load variation in case of dynamic measurements, it was chosen to scale C_T with the thrust coefficient ($C_{T_{start}}$) at $yaw = 0^\circ$ or at the start of the yaw manoeuvre. Finally, the

thrust coefficient variation can directly be assessed by the measurement of the pitch moment $\frac{C_T}{C_{T\,start}} = \frac{T_Y}{T_{Y\,start}}$. According to the balance specifications, the torque measurement uncertainty (95 % confidence level) is 1.75 % of the full-scale load (4 Nm), that is unfortunately too close to the torque values measured for the HIT1 conditions, for both porosity levels and for the higher porosity in ABL condition. Hence, these three configurations will not be considered in the further load investigations because not sufficiently reliable. In the case of static load measurements (no yaw variation of the upstream model), the results are retrieved by averaging a 2 minute acquisition at 2kHz, and then, the averaged six values of voltage (after the subtraction of the offset voltages) are converted into the six load components via a conversion matrix provided by the balance constructor. In case of dynamic configurations, acquisitions are performed for a minimum of 500 consecutive 0°-30° back and forward yaw displacement cycles at a sampling frequency of $2kHz$. A pre-processing of data is needed to filter out the natural frequency of the balance. A zero-phase digital low pass 5^{th} order Butterworth filtering strategy was applied to the raw balance signals in order to filter out the balance resonance ($\approx 6Hz$) without rejecting the first harmonics of the cyclic yawing frequency. The cut-off frequency of the filter was generally an half balance resonance frequency. An example of the load measurement data processing for a dynamic yaw variation is given for the HIT2 set-up. Figure 3.19 shows the power spectral density (PSD) for the concatenated yaw variation, and the load fluctuations $\frac{C_T}{C_{T\,start}}$. The last part of the data processing consists in the proper phase-averaging on the rising and descending yaw ramp. Indeed, thanks to the synchronisation of the encoder and the balance acquisitions, it was possible to isolate each ramp of yaw variation (here in after positive yaw variation for 0° to 30° and negative yaw variation for 30° to 0°) relying on the yaw measurement. In this way, it was possible to properly and repeatably detect the start and the end of each ramp in order to make an accurate phase average of all the ramps. Figure 3.20 shows, as an example, the averaging results for the "cycle averaging" approach. It is possible to appreciate and notice the post processing protocol effectiveness from the averaging effect. Indeed, the shape of $\frac{C_T}{C_{T\,start}}$ in the case of the absence of filtering strategy shows that, for dynamic conditions, the phase-average itself is not sufficient to filter out the balance resonance. Observing the shape of the $\frac{C_T}{C_{T\,start}} filtered$, it is possible to appreciate the smoothing effect of the filtering strategy. Moreover, due to the general superposition of both curves and taking into account the applied filtering strategy, it is possible to assume that the oscillations of the original curve are related to the balance resonance frequency and that filtering out this frequency does not distort the main pattern.

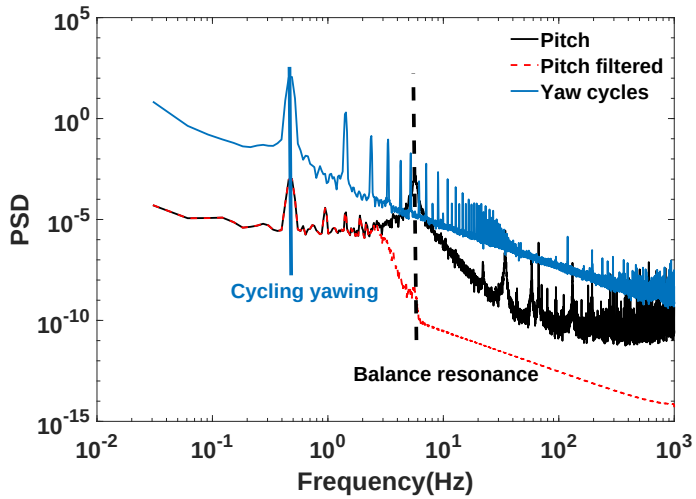

Figure 3.19 – *Power spectral density of the yaw motion and pitch moment.*

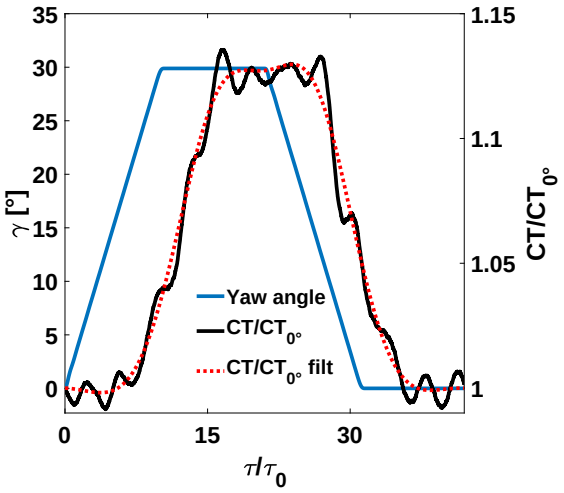

Figure 3.20 – *Example of a yaw motion cycle and the associated cycle-averaged WT thrust coefficient variation.*

Chapter 4

Wake and load dynamics under yaw manoeuvres

In this chapter, the results of the three wind tunnel experimental campaigns discussed in this manuscript will be treated and analysed. Some of these results has been published in Macrí et al. [2020]. It has to be mentioned that several experimental data analysis protocol were investigated, passing through different steps and different approaches, especially as concerns the center of the wake determination method, as discussed in chapter 3. For the sake of clarity, the results obtained with previous approaches are not exposed here because a detailed analysis of these results can be found in Macrì et al. [2018] and Macrì et al. [2020].

4.1 Results for static yaw conditions

This section resumes results concerning the influence of various static yaw angles applied to an upstream wind turbine on its wake deviation, on the available wind power for a virtual downstream wind turbine and on the actual thrust applied to a downstream wind turbine. They will serve as baseline reference cases for the remainder of the chapter dealing with dynamic yaw variation.

4.1.1 Wake center deviation

The measurements were performed for yaw angles γ from 0° to 30° by steps of 10°. The static wake deviation was studied for all the experimental configurations listed in table 4.1 and for both disc porosity levels. Before going into more details of the wake deviation analysis, figure 4.1 shows an example of PIV velocity field measurement for the HIT1 P1 case, where it is possible to appreciate the wake deviation effects on the two dimensional wake signature.

Table 4.1 – *Experimental configurations analysed in static conditions : spacing Δx, reference scaled wind speed U_{ref}, porosity level P, induction factor a*

	Δx $[m]$	U_{ref} $[ms^{-1}]$	P $[\%]$	a
HIT1 P1	$3.5 \times D$	6	57	0.16
HIT2a P1	$4.2 \times D$	5	57	0.16
HIT2b P1	$4.2 \times D$	10	57	0.16
HIT2c P1	$4.2 \times D$	15	57	0.16
ABL P1	$4.2 \times D$	5	57	0.16
HIT1 P2	$3.5 \times D$	6	67	0.11
HIT2a P2	$4.2 \times D$	5	67	0.11
HIT2b P2	$4.2 \times D$	10	67	0.11
HIT2c P2	$4.2 \times D$	15	67	0.11
ABL P2	$4.2 \times D$	5	67	0.11

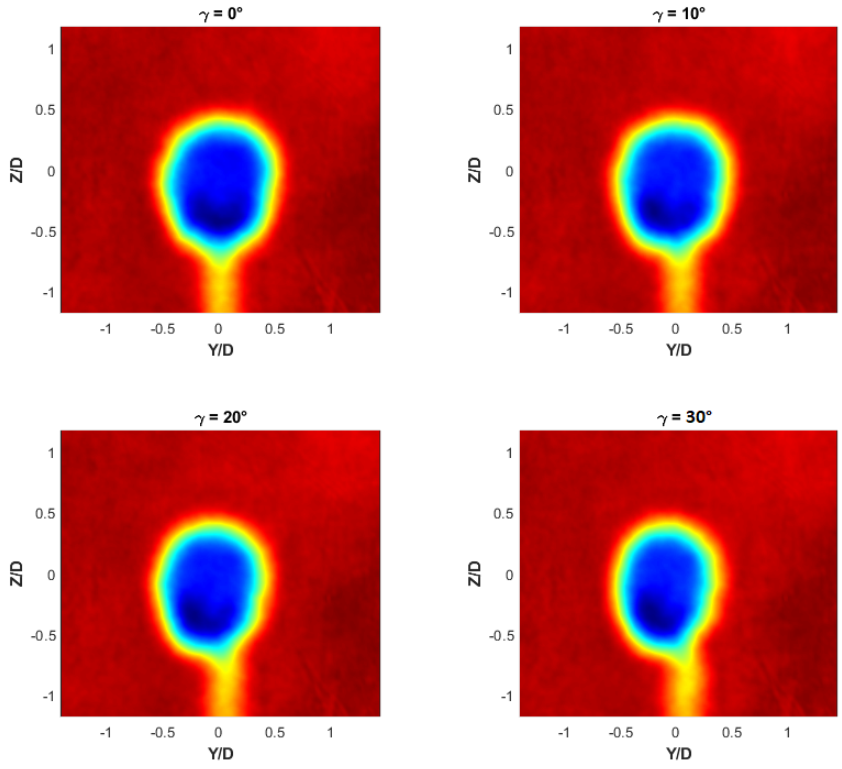

Figure 4.1 – Stereo PIV velocity fields for static HIT1 P1 configuration.

Figure 4.2 shows a summary of the wake deviation angle, determined via the estimation of the available wind power of a potential downstream wind turbine model (Eq.3.10), versus the wind turbine yaw angle for static conditions.

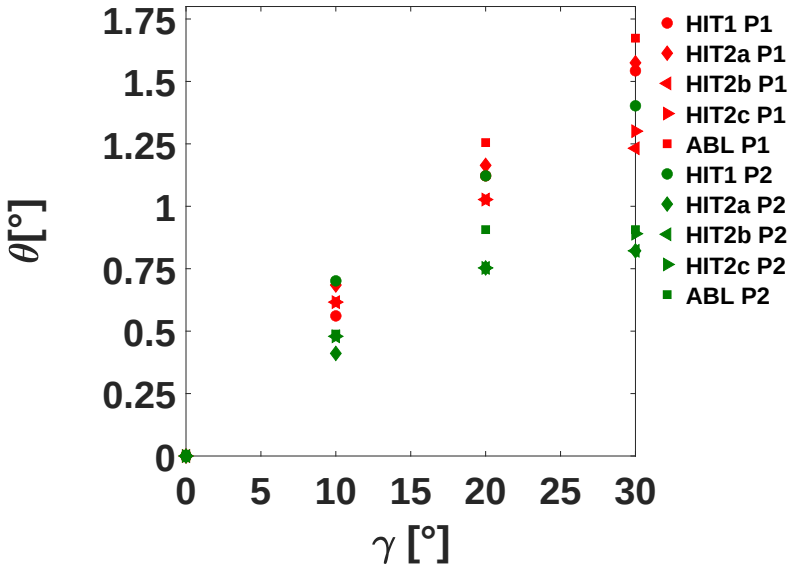

Figure 4.2 – Wake deviation angle θ, determined via the estimation of the available wind power of a potential downstream wind turbine model (Eq.3.10), as a function of the yaw angle γ. Red symbols represent the lower porosity (P1), green symbols the higher (P2).

Several general comments can be made:

- As already shown by previous studies (Parkin et al. [2001], Howland et al. [2016], Espana [2009]), the relationship between the wake deviation angle and the yaw angle is a non-linear monotonically increasing function and the wake deviation angle is one order of magnitude lower than the yaw angle. Theoretically, due to the absence of rotational entrainment in the wake of a porous disc, the absolute value of the wake deviation angle is identical for negative or positive yaw angles. A different behavior had been observed for a rotating wind turbine model, with a light dependence of the wake deviation angle to the direction of misalignment (Bastankhah and Porté-Agel [2016a], Bartl et al. [2018]). It is assumed in the present work that this asymmetry does not play a major role in the wake dynamics and therefore, is not studied.
- The results show some scatter inherent to the propagation of cumulative errors (measurement, statistical, processing) and illustrate the difficulty of

accurately determining such a small deviation angle (maximum measurement error θ=$\pm$0.07°).

- No dependence on flow conditions can be detected.

- The porosity level (and hence the equivalent induction factor) affects the wake deviation: cases with a lower porosity level (higher induction factor) present a higher wake deviation.

- In Macrì et al. [2018], present authors made some comparisons between similar experimental results and wake deviation empirical models. The trends were similar but the models systematically overestimated the wake deviation compared to experimental values. Comparison is also very sensitive to the wake center definition used (not shown here but mentioned in Coudou et al. [2018]). Indeed, there are several wake center tracking methods and their extrapolation to skewed wakes is still under discussion.

Some specific discrepancies can be stressed:

- The HIT1 P2 configuration presents a higher deviation than the other ones with the same porosity level, without any straightforward physical grounds.

- The ABL P2 configuration presents a discrepancy between its trend (especially at γ = 20°) and the other results at the same porosity level. This is because the flow inhomogeneity together with the higher level of ambient turbulence make the velocity deficit generated by the disc with the higher porosity level rather small and unsuitable to properly track the wake center. For these reasons, the ABL P2 configuration will not be discussed further.

- The discrepancies that can be seen for the cases HIT2b P1 and HIT2c P1, with respect to the other P1 porosity level cases, are not unusual in experimental measurements (Aubrun et al. [2019]) and may be due to a minor variation in the performances of one of the experimental measurement systems while changing the set-up.

4.1.2 Available wind power variations of the downstream wind turbine

Figure 4.3 shows the available wind power density variations (P_{avd}) at the downstream wind turbine location versus the static yaw angle of the upstream wind turbine.

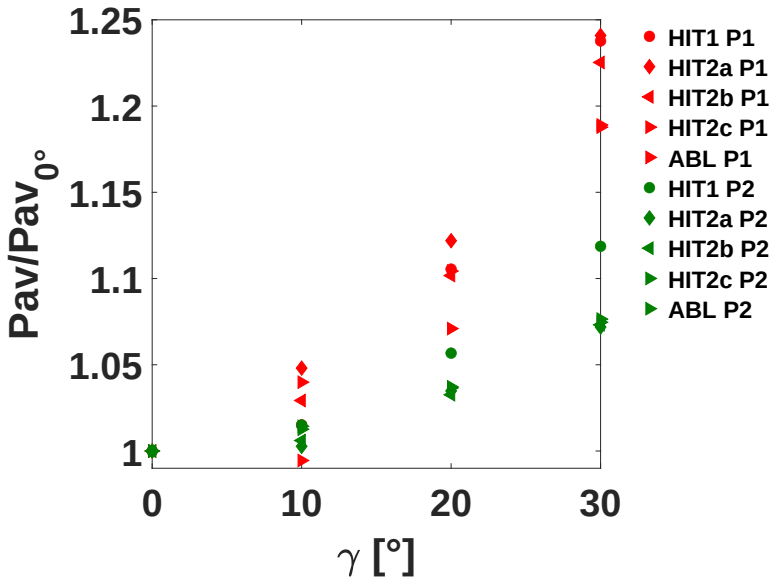

Figure 4.3 – Normalised available power of the downstream wind turbine model versus the yaw angle of the upstream wind turbine model. Red symbols: porosity P1, green symbols: porosity P2.

Several general comments can be made:

- As for the wake center and the downstream wind turbine thrust coefficient, the relationship between the available wind power at the downstream wind turbine location and the yaw angle of the upstream one is a non-linear monotonically increasing function.

- As for the thrust coefficient, there is a clear effect of porosity, and so the induction factor. For the P1 porosity cases, the gain for a 30° yaw angle compared to the one for no yaw condition is around 23 %, while it is about 7 % for the lower P2 porosity level. It is interesting to mention that the gain appears to be higher than those obtained for the thrust coefficient. This is probably due to the different nature of the parameters. Indeed, the available wind power does not take into account the downstream wind turbine performances, while the thrust coefficient is a direct indicator of the turbine operation.

- As for the wake center deviation, the HIT1 P2 configuration presents a higher increment than the other ones with the same porosity level, without any straightforward physical grounds.

- As for the wake center deviation, the discrepancies that can be seen for the cases HIT2b P1 and HIT2c P1 are not unusual in experimental measurements (Aubrun et al. [2019]) and may be due to a minor variation in the performances of one of the experimental measurement systems while changing the set-up.

4.1.3 Downstream wind turbine thrust coefficient variation

Figure 4.4 shows the downstream wind turbine thrust coefficient versus the static yaw angle applied to the upstream wind turbine measured by the aerodynamic balance (cf. § 3.5), for both porosity levels and for all the flow conditions mentioned in table 4.1.

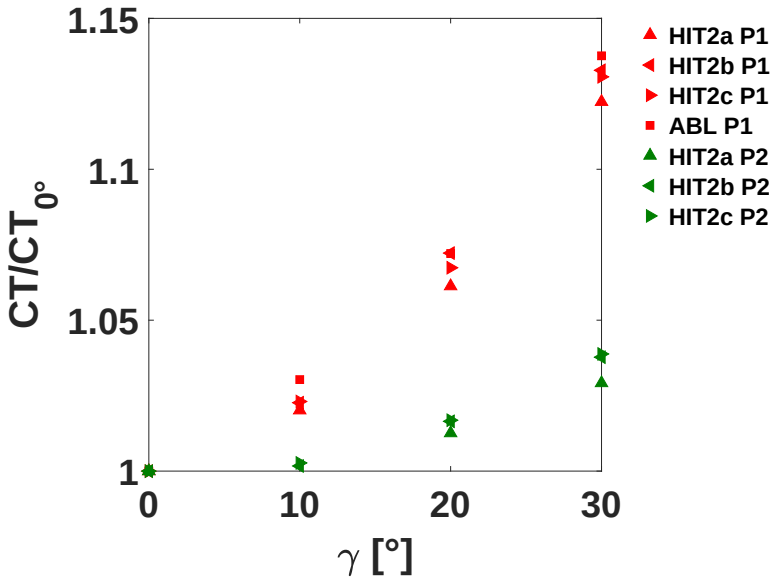

Figure 4.4 – Normalised thrust coefficient of the downstream wind turbine model versus the yaw angle of the upstream wind turbine model. Red symbols: porosity P1, green symbols: porosity P2.

Several general comments can be made:

- The relationship between the downstream wind turbine thrust coefficient and the yaw angle is a non-linear monotonically increasing function.
- This indicator presents less scatter than the wake deviation angle and the results do not show any unexplained outliers. Its integrative nature (global

load applied to the porous disc) plays a smoothing role and the range of variations is also more significant.

- There are clear thrust differences depending on the porosity level. For the P1 porosity cases, the thrust gain for a 30° yaw angle compared to the 0° case is around 13 %, irrespective of the flow conditions, while for the lower porosity level, it is about 3 %. These values suggest a remarkable influence of the porosity (and hence the axial induction factor) on the consequences of a yaw modification of an upstream wind turbine on the load applied to a downstream one.

4.2 Comparison of aerodynamic performances of both wind turbine

This part of the chapter aims to compare the aerodynamic performances of the yawed upstream wind turbine with the performances of the downstream wind turbine. The wind turbine being modelled by porous discs, this evaluation will be done using the C_P and C_T variation laws from the actuator disc concept theory, for both non yawed (section 2.1.1) and yawed conditions (section 2.2.3).

4.2.1 Yawed upstream wind turbine thrust and power coefficients

In this section, the method to assess the thrust coefficient variation of the upstream wind turbine consequent to its yaw variation will be described for a yaw angle from $-30°$ to $30°$. Because during the aforementioned experimental campaigns the efforts on the upstream wind turbine were not measured, the evaluation of the thrust coefficient variation for the upstream wind turbine was retrieved by re-exploiting experimental data acquired during an ancient experimental campaign performed in the main test section of the Malavard wind tunnel (HIT2 configuration, with a 0.2 m diameter porous disc, a reference wind speed $U_{ref} = 20ms^{-1}$ and an induction factor $a = 0.21$). The model is mounted on a 6-component platform balance that provided time averaged lift and drag forces as well as aerodynamic moments, a detailed description of balance performances and configuration can be found in Baleriola [2018]. The thrust coefficient (C_T) is retrieved by the measurement of the drag force (F_x) in the wind x direction and the drift force (F_y) in the y direction. Indeed, by the measurement of these two forces, it is possible to retrieve the C_x and C_y:

$$C_x = \frac{F_x}{0.5\rho U_{ref}^2 S_d} - C_{x-rod} \tag{4.1}$$

$$C_y = \frac{F_y}{0.5\rho U_{ref}^2 S_d} \tag{4.2}$$

where ρ is the air density, U_{ref} the free stream velocity, S_d the disc surface and C_{x-rod} the thrust coefficient of the cylinder rod that supports the disc. In this way only the forces exerted on the disc are taken into account. These two coefficients represent the components of the thrust coefficient C_T in the flow direction and the side direction. Therefore, the thrust coefficient can be retrieved as it follows:

$$C_T = \sqrt{C_x^2 + C_y^2} \tag{4.3}$$

By simple trigonometric considerations, the angle β between C_x and C_y can be deduced:

$$\beta = \operatorname{atan} \frac{C_y}{C_x} \tag{4.4}$$

Taking into account the definition of the thrust coefficient for yawed conditions introduced in section 2.2.3, the thrust force T is normal to the disc surface (Fig.2.10). Therefore the values of β are supposed to be equal to the yaw angle γ. Looking at figure 4.5, it is evident that this is not the case. Indeed, it seems evident that a linear relationship links both angles, generally $\beta \approx 0.47\gamma - 1.11$, it is interesting to mention that the behaviour is symmetrical according to the yaw angle sign. This leads to different possible considerations on the interpretation of the results, and especially to the proper comparison between the experimental results and the theoretical law describing the variation of the thrust coefficient of the upstream wind turbine consequent to its yaw angle (Eq.2.40). Looking at the hypothesis of the *Momentum theory* it seems reasonable to think that the values of C_T retrieved by the balance measurements should be projected on the normal direction to the disc surface. Just on the purpose of discussing the two possible solutions, the measured values of the thrust coefficient C_T were projected on the perpendicular of the disc surface leading to C_{Tn}:

$$C_{Tn} = C_T \cos(\gamma - \beta) \tag{4.5}$$

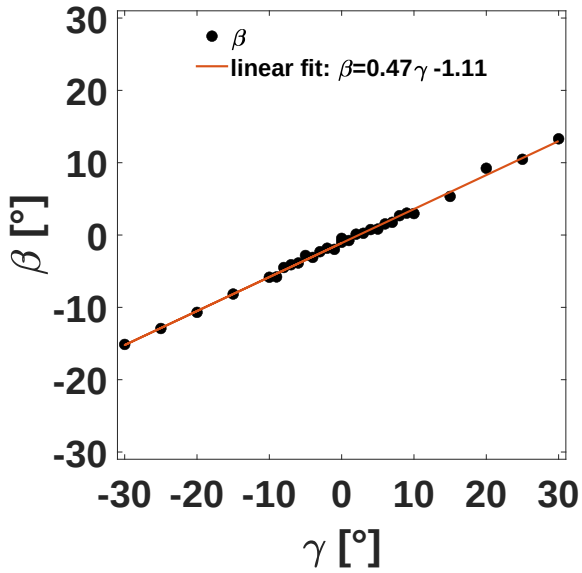

Figure 4.5 – Angle β, defined between C_T and the wind direction, versus the wind turbine yaw angle γ.

Figure 4.6 shows a comparison of the normalised thrust coefficient values with the expected theoretical values:

$$C_{Tad}(\gamma) = 4a(cos\gamma - a) \tag{4.6}$$

Looking at the results, the C_T values have a good agreement with the expected values, especially for yaw angle below 15°, while the C_{Tn} values are remarkably lower. It is also interesting to notice that, as for the angle β, also the experimental values of both C_T and C_{Tn} have a symmetrical behaviour according to the yaw angle sign. Despite, the theory suggests that the proper way to compare the results with the expected value should be to use C_{Tn} it is evident that C_T works better. One possible cause of this discrepancy could be on the fact that, always according to the actuator disc theory, only the perpendicular components of the wind speed (and so the force?) concur to the power extraction and this could bring to neglect the transversal components of the forces. These are just considerations on the results analysis to support the use of the actuator disc theoretical laws to describe the thrust and power coefficient variations according to a yaw manoeuvre. Being not the aim of this work to discuss the interpretation and the application of theory behind the use of the actuator disc concept, these considerations will not be pushed forward. Finally, despite these discrepancies between theory and measurements it seems reasonable to use the law deduced from the same theory

for the power coefficient variation according the yaw manoeuvre:

$$C_{Pad}(\gamma) = 4a(cos\gamma - a)^2 \tag{4.7}$$

Figure 4.7 shows the expected normalized power coefficient in function of the upstream wind turbine yaw angle. Showing that a 30° yaw angle could lead to a C_P reduction beyond the 30%.

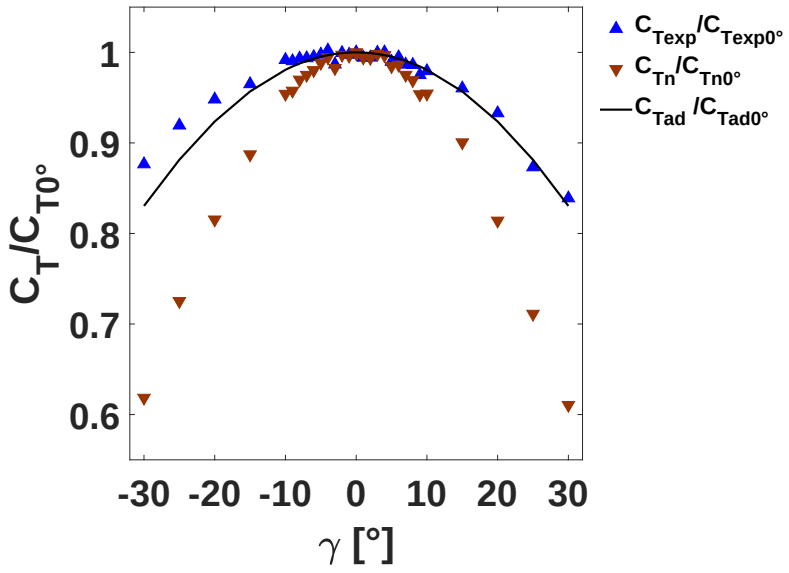

Figure 4.6 – Normalised thrust coefficient of the upstream wind turbine compared with the theoretical law from the actuator disc theory.

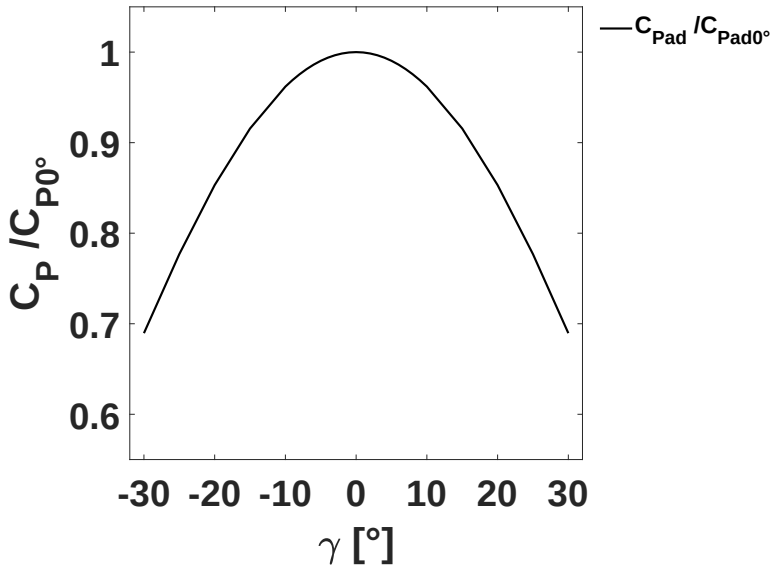

Figure 4.7 – Normalised power coefficient of the upstream wind turbine predicted by the the theoretical law from the actuator disc theory.

4.2.2 Downstream wind turbine performances

In this section the thrust and power coefficients of the downstream wind turbine will be retrieved by the load measurements described in section 3.5. In order to be able to assess the global performance of the two-turbine system in the next section, it was chosen to use as a unique reference, the thrust coefficient for the wind turbine model located in an undisturbed flow, so the performance that the wind turbine would have had without the presence of wake interaction. The thrust coefficient C_T defined as in equation 3.11 is normalized by the measurement of the thrust coefficient in case of upstream turbine yaw angle of 90°, in this way it is possible to retrieve in a quite satisfactory manner the coefficient for free-stream conditions. Figure 4.8 shows the results of the thrust coefficient variations normalised by the free-stream condition. Most of the considerations are the same as done in section 4.1.3 although, due to the different normalization strategy, some further comments can be done:

- as expected, a clear effect of the porosity on the thrust variation can ben distinguished. Indeed, although the higher porosity has shown a lower increase in terms of load on the downstream wind turbine model (Fig.4.4) the values compared to the free-stream condition are always remarkably higher than for the lower porosity.

- although data are available only for porosity P1 and so not generalised, in ABL conditions the normalized thrust values are higher than for homogeneous flows.

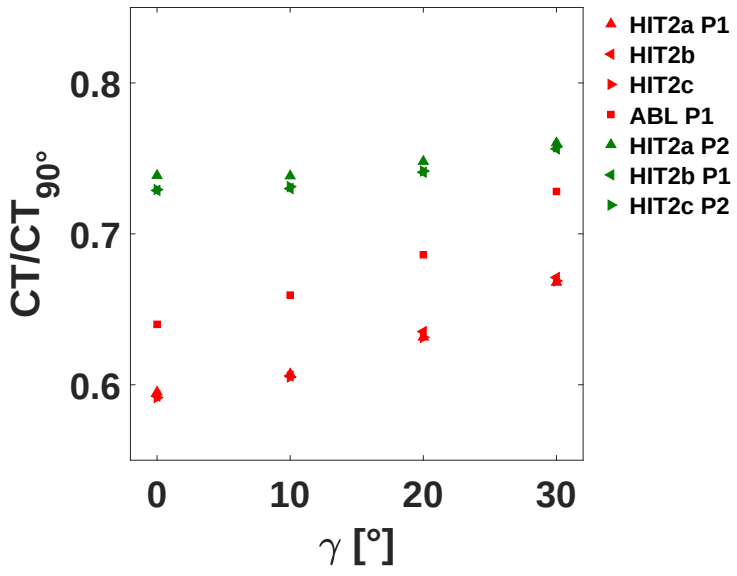

Figure 4.8 – Normalised thrust coefficient of the downstream wind turbine model. Red symbols: porosity P1, green symbols: porosity P2

Regarding the downstream wind turbine power coefficient variation, taking into account the fact that the downstream wind turbine is not subjected to yaw motion, its power coefficient is defined as:

$$C_P = \frac{F_x U_d}{0.5 \rho U_{ref}^3 S_d} \tag{4.8}$$

where F_x represents the force on the disc surface S_d, ρ the air density, U_d the velocity at the disc location and U_{ref} the reference wind speed. Some considerations can be done about the reference wind speed, indeed for the actual thrust coefficient on the downstream disc, U_{ref} should be varied according to the wake interaction, but given the purpose of normalise with the undisturbed condition it is more relevant to use the free-stream velocity as U_{ref} for all the yaw angles. Different approaches have to be taken for U_d that, in case of free-stream condition, is related to the U_{ref} by the relation in equation 2.2. Indeed, because of the wake interactions the reference wind speed for the downstream wind turbine model it

would not be the free-stream velocity but a lower velocity U_{av} defined as the mean available wind speed in the region were it would be placed the downstream wind turbine. This value is retrieved by the PIV measurements on a disc surface placed where it would be the downstream wind turbine model:

$$U_{av}(Y_0, Z_0) = \frac{1}{S_d} \iint u(y,z)dydz \quad (y - Y_0)^2 + (z - Z_0)^2 \leq \left(\frac{D}{2}\right)^2 \tag{4.9}$$

where u is the stream-wise velocity component over a plane normal to the flow direction, S_d is the disc surface, D the disc diameter, Y_0 and Z_0 the coordinates of where it would be the center of the downstream wind turbine model. So it is possible to rewrite the power coefficient as:

$$C_P = \frac{F_x(1-a)U_{av}}{0.5\rho U_{ref}^3 S_d} \tag{4.10}$$

As for the C_T analysis, the power coefficient will be normalised by the reference case of upstream turbine yaw angle of 90° where $U_{av} \approx U_{ref}$. Therefore considering that the induction factor is defined as a disc characteristics, it does not change according to any external condition. Via some algebraic steps, it is possible to assess that the C_P variation **normalized by the the free stream condition** corresponds to the the thrust variation **normalized by the the free stream condition** multiplied by the ratio between the available wind speed and the reference wind speed:

$$\frac{C_P}{C_{P90^\circ}} = \frac{C_T}{C_{T90^\circ}} \frac{U_{av}}{U_{ref}} \tag{4.11}$$

Figure 4.9 shows the downstream turbine model power coefficient according to the upstream wind turbine yaw angle. Because of its definition (Eq.4.11) the same considerations done for the thrust coefficient in figure 4.8 are valuable also for the power coefficient.

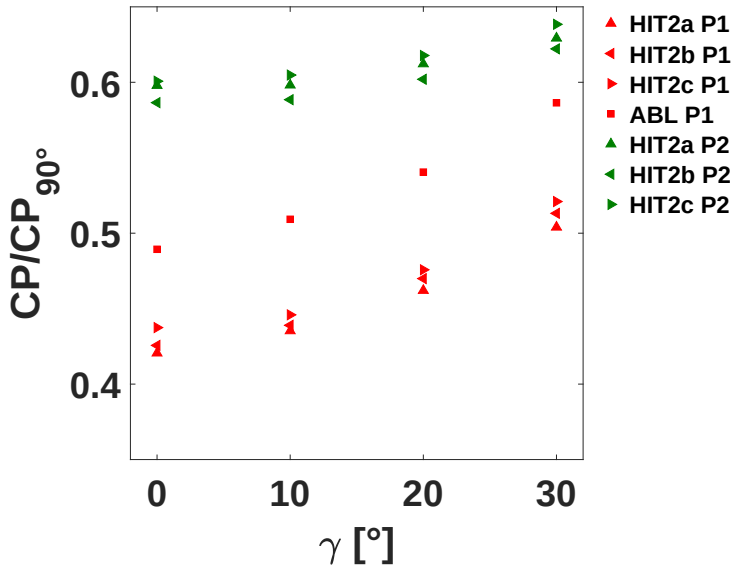

Figure 4.9 – Normalised power coefficient of the downstream wind turbine model. Red symbols: porosity P1, green symbols: porosity P2

4.2.3 Wind farm performances

In this section an attempt to evaluate the wind farm performance according to the *Actuator Disc Theory* (section 2.1.1) is performed. It is important to state that the rentability of the wake steering strategy has already been discussed and proven by several studies in both wind tunnel (with rotating model) and full scale. This analysis is just an evaluation of the possibility to have reliable results using the actuator disc concepts. As concerns to the upstream wind turbine performances, there will be used equations 4.6 and 4.7 already discussed in section 4.2.1, using the induction factors correspondent to P1 and P2 porosity levels (see Tab.4.1), while for the downstream turbine $\frac{C_P}{C_{P90^\circ}}$ consequently to the consideration done in section 4.2.2. So by simple algebraic steps on the theoretical equations, it is possible to define the global power performances of the two wind turbines as:

$$\eta_{CP} = \frac{1}{2}\left(\frac{(cos\gamma - a)^2}{(1-a)^2} + \frac{C_P}{C_{P90^\circ}}\right) \tag{4.12}$$

Figure 4.10 shows the variation of the global power performances η_{CP}.

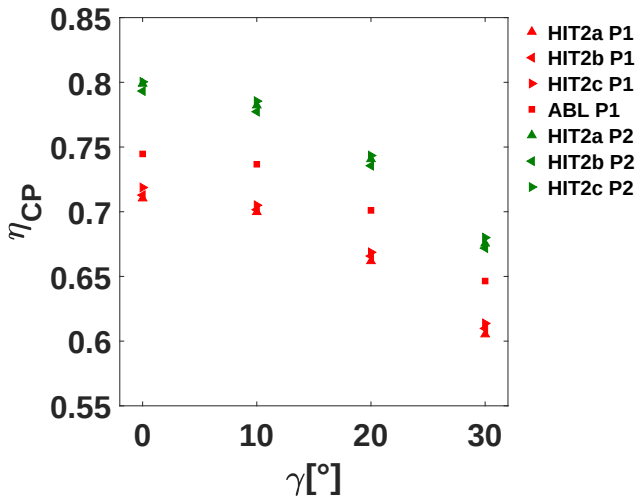

Figure 4.10 – Global load performances η_{CP}. Red symbols: porosity P1, green symbols: porosity P2.

Looking at the results the wake steering does not seem to have a positive effect on the overall wind turbine system. Indeed the global performances decrease while the yawing strategy is applied. Nevertheless, several works cited in section 2.3.2 have somehow proven the effectiveness of this strategy, so probably the present results would suggest the non-feasibility of this kind of performance analysis by the use of the actuator disc theory.

4.3 Results for dynamic yaw conditions

4.3.1 Metrics for dynamics

To analyse the effects of yaw manoeuvre on the upstream wind turbine wake and the downstream wind turbine thrust dynamics, some metrics to determine the properties of the transient phenomena need to be defined. It is necessary to establish a common protocol (equally reliable) to assess the transient duration, start and end for the three phenomena: yaw manoeuvre, wake deviation, available wind power variation and thrust variation. First, the cycle-averaged yaw angle, the wake deviation angle, the available power density and the thrust coefficient values were normalized in order to have transient curves between 0 and 1:

$$\Delta\gamma^* = \frac{\gamma - \gamma_{start}}{\gamma_{end} - \gamma_{start}} \tag{4.13}$$

with γ_{start} and γ_{end} the γ values before and after the transient,

$$\Delta\theta^* = \frac{\theta - \theta_{start}}{\theta_{end} - \theta_{start}} \tag{4.14}$$

with θ_{start} and θ_{end} the θ values before and after the transient,

$$\Delta P_{av}^* = \frac{P_{av} - P_{av_{start}}}{P_{av_{end}} - P_{av_{start}}} \tag{4.15}$$

with $P_{av_{start}}$ and $P_{av_{end}}$ the P_{av} values before and after the transient,

$$\Delta C_T^* = \frac{C_T - C_{T_{start}}}{C_{T_{end}} - C_{T_{start}}} \tag{4.16}$$

with $C_{T_{start}}$ and $C_{T_{end}}$ the C_T values before and after the transient.

In order to facilitate the determination of the start and the end of transient phenomena, fitting laws were applied to the transient curves, depending on the yaw manoeuvre sign (yaw increase or yaw decrease). Below, some examples of these fitting laws are presented only for the wake center deviation and the thrust variation. The same considerations can be done for the power density. For the positive yaw manoeuvre, the cycle-averaged results were fitted to equation 4.17, while for the negative yaw variation they were fitted to equation 4.18.

$$\Delta\theta^*(\tau) \text{ or } (\Delta C_T^*(\tau)) = 1 - exp\left(-\frac{\frac{\tau-\tau_{lag}}{\tau_0}}{c}\right)^3 \text{ for } \tau > \tau_{lag} \tag{4.17}$$

$$\Delta\theta^*(\tau) \text{ or } (\Delta C_T^*(\tau)) = exp\left(-\frac{\frac{\tau-\tau_{lag}}{\tau_0}}{c}\right)^3 \text{ for } \tau > \tau_{lag} \tag{4.18}$$

For both equations, c and τ_{lag} are the fitting coefficients, τ the time triggered with the yaw manoeuvre start, and τ_0 the aerodynamic time scale. c represents the variation rate of the function and can be linked to the transient duration, whereas τ_{lag} represents the beginning of the function evolution and can be linked to the transient start. The fitting coefficients were determined by a classical non linear least square fitting method. Regarding the yaw angle, a fitting procedure was not necessary because of the high time resolution and precision of the acquisition. Finally, the transient start τ_{start} corresponds to the time when the curve crosses the 5% threshold of the total variation and the transient end τ_{end} to the time when the curve crosses the 95% threshold. Dimensionless values are obtained by dividing all times by the aerodynamic time scale τ_0: $\tau_{start}^* = \frac{\tau_{start}}{\tau_0}$ and $\tau_{end}^* = \frac{\tau_{end}}{\tau_0}$. The transient dimensionless manoeuvre duration $\Delta\tau_\theta^*$ is obtained by retrieving the time difference between these two dimensionless values: $\Delta\tau_\theta^* = \tau_{end}^* - \tau_{start}^*$. As concerns the wake deviation angle, the power density and the thrust coefficient, the start

(τ_{start}) and the end (τ_{end}) parameters could also have been retrieved in a similar way as presented in Macrì et al. [2020], crossing the line of slope $\frac{d\Delta\theta^*}{d\tau}$,$\frac{d\Delta C_T^*}{d\tau}$ and $\frac{d\Delta P_{av}^*}{d\tau}$, corresponding to the point of the maximal gradient of this curve with the aforementioned thresholds. This approach has finally not been applied because it considers the variations as linear, neglecting therefore the acceleration and deceleration phases. Indeed, with this method, τ_{start}^* is over-estimated. while τ_{end}^* under-estimated, this leads to a consequent underestimation of the duration in comparison with the methods based on the exponential fit. Figure 4.11 shows an example of the transient duration determination for the wake deviation during a positive yaw variation and figure 4.12 for a negative yaw variation. Figure 4.13 and figure 4.14 show two examples of the transient duration determination of the thrust coefficient during a positive yaw variation and during a negative yaw variation respectively.

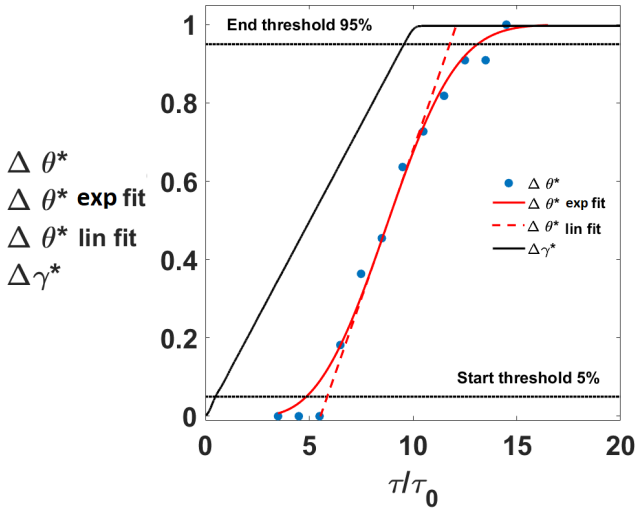

Figure 4.11 – Example of cycle-averaged wake deviation history during yaw manoeuvre for configuration HIT1 P1 during a positive yaw variation. Symbols: — $\Delta\gamma^*$,● $\Delta\theta^*$, - - - $\Delta\theta^*$ linear, — $\Delta\theta^*$ exp fitted, - - start thresholds. Data fitted for $\tau > \tau_{lag}$.

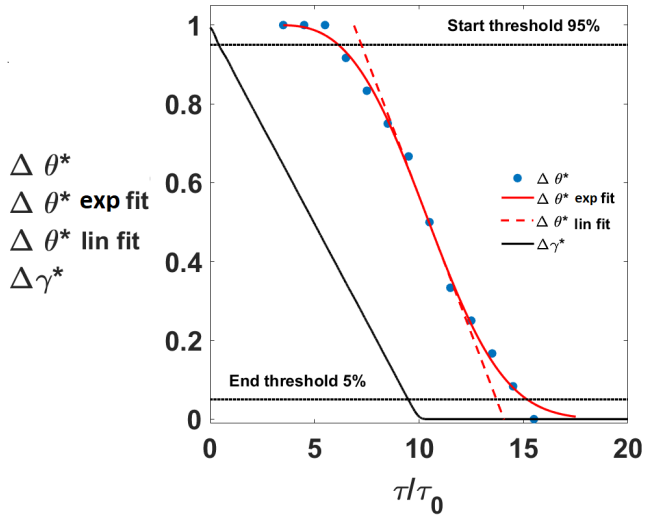

Figure 4.12 – Example of cycle-averaged wake deviation history during yaw manoeuvre for configuration HIT1 P1 during a negative yaw variation. Symbols: — $\Delta\gamma^*$,● $\Delta\theta^*$, - - - $\Delta\theta^*$ linear, — $\Delta\theta^*$ fitted, - - start thresholds. Data fitted for $\tau > \tau_{lag}$.

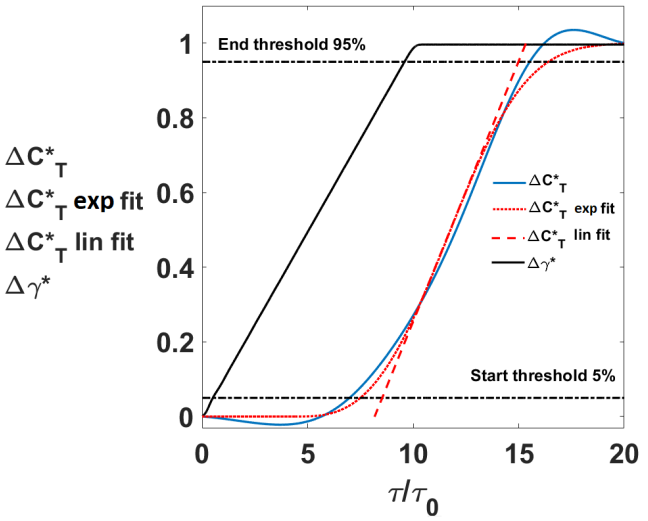

Figure 4.13 – Example of cycle-averaged thrust coefficient history during yaw manoeuvre for configuration HIT2a P2 during a positive yaw variation. Symbols: — $\Delta\gamma^*$, — ΔC_T^*, - - - ΔC_T^* linear, — ΔC_T^* exp fitted, - - start and end thresholds. Data fitted for $\tau > \tau_{lag}$.

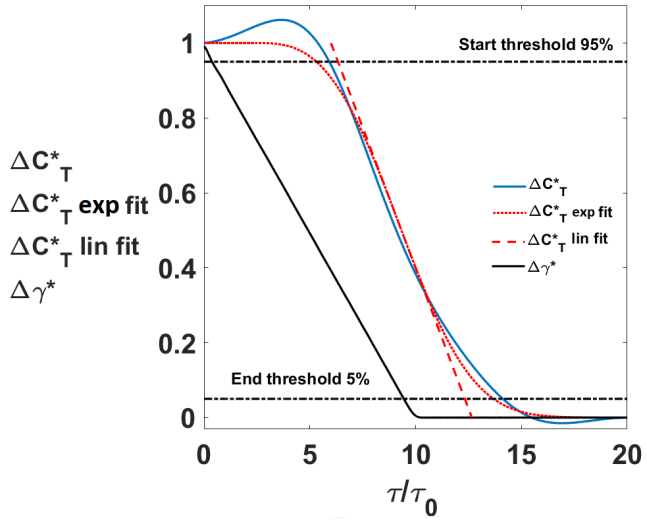

Figure 4.14 – Example of cycle-averaged thrust coefficient history during yaw manoeuvre for configuration HIT2a P2 during a negative yaw variation. Symbols: — $\Delta\gamma^*$, — ΔC_T^*, - - - ΔC_T^* linear, — ΔC_T^* exp fitted, - - start and end thresholds. Data fitted for $\tau > \tau_{lag}$.

Other metrics defined for this study are $\Delta\tau^*_{ratio}$ and $\frac{U_{adv}}{U_{ref}}$. The first one represents the ratio between the wake deviation duration and the manoeuvre duration ($\Delta\tau^*_{ratio} = \frac{\Delta\tau^*_\theta}{\Delta\tau^*_m}$). The second one represents the ratio between the advection velocity and the reference wind speed. The advection velocity is defined as the ratio between the streamwise spacing Δx between the upstream wind turbine model and the downstream location (where the wake deviation is investigated or where the downstream wind turbine model is located), and the delay between the start of the manoeuvre and the start of the wake deviation ($U_{adv} = \frac{\Delta x}{\tau_{start}}$). In order to obtain intermediate information between the upstream wind turbine wake deviation and the response of downstream wind turbine in term of thrust modification, the same metrics were also calculated for the available wind power density at the downstream wind turbine position. All the metrics applied to the dynamic wake deviation of the upstream wind turbine, and to the thrust variation of the downstream wind turbine, are summarized in tables 4.2 and 4.3, respectively. It is important to mention that for cases 10 & 11, the yaw manoeuvre speed was doubled in order to evaluate the influence of a speed-up.

Table 4.2 – *Dynamic wake deviation metrics.*

		Positive yaw manoeuvre							Negative yaw manoeuvre						
Case	set-up	c	τ^*_{lag}	τ^*_{start}	τ^*_{end}	$\Delta\tau^*_{\theta}$	$\Delta\tau^*_{ratio}$	$\frac{U_{adv}}{U_{ref}}$	c	τ^*_{lag}	τ^*_{start}	τ^*_{end}	$\Delta\tau^*_{\theta}$	$\Delta\tau^*_{ratio}$	$\frac{U_{adv}}{U_{ref}}$
1	HIT1 P1	7.7	2	4	12.3	8.3	1	0.87	8.4	3	5.3	14.3	9	1.10	0.66
2	HIT1 P2	7.9	0.9	3	11.5	8.5	1.03	1.1	8.5	2.7	5	14.1	9.1	1.11	0.7
3	HIT2a P1	9.6	0.8	3.9	14.2	10.3	1.13	1.08	7.3	5	7.3	15.2	7.9	0.87	0.57
4	HIT2a P2	8.5	1.3	4	13.1	9.1	1.01	1.05	7.2	4.6	6.9	14.5	7.6	0.85	0.6
7	HIT2c P1	11.9	0.3	3.9	16.6	12.7	1.54	1.08	6.9	4.6	6.3	13.6	7.3	0.89	0.67
9	ABL P1	8.2	2	4.6	13.3	8.7	0.96	0.91	7.6	4.4	6.8	15	8.2	0.90	0.61
10	HIT2a 2S P1	4.8	3.2	4.6	9.7	5.1	1.21	0.91	3.8	4.7	5.8	9.9	4.1	0.97	0.72
11	HIT2a 2S P2	4.5	3.4	4.7	9.4	4.7	1.13	0.89	3.9	4.4	5.5	9.7	4.2	0.99	0.76

Table 4.3 – *Dynamic thrust metrics.*

		Positive yaw manoeuvre						Negative yaw manoeuvre					
Case	set-up	c	τ^*_{lag}	τ^*_{start}	τ^*_{end}	$\Delta\tau^*_{C_T}$	τ^*_{ratio}	c	τ^*_{lag}	τ^*_{start}	τ^*_{end}	$\Delta\tau^*_{C_T}$	τ^*_{ratio}
3	HIT2a P1	8.4	4.3	6.9	16	9.1	0.98	7.8	2.4	4.9	13.3	8.4	0.98
4	HIT2a P2	6.3	6.4	8.2	15	6.8	0.73	6.3	1.9	3.9	10.6	6.7	0.73
5	HIT2b P1	7.7	5.2	7.2	15.5	8.3	0.97	6.9	3.6	5.9	12.9	7.4	0.97
6	HIT2b P2	6.7	6.2	7.8	15	7.2	0.83	5.9	3.5	5.1	11.4	6.3	0.83
7	HIT2c P1	7.6	5.6	7.5	15.6	8.1	0.97	6.7	3.8	5.6	12.8	7.2	0.98
8	HIT2c P2	6.5	6.6	8.1	15.1	7	0.81	7.1	2.4	4.3	12	7.7	0.81
9	ABL P1	9	4.2	7.1	16.6	9.6	1.03	7.9	2.6	5.1	13.5	8.4	1.03
10	HIT2a 2S P1	4.1	4.9	6	10.5	4.5	1.03	3.1	4.6	5.4	8.8	3.3	1.02
11	HIT2a 2S P2	4.7	4.3	5.6	10.7	5.1	1.19	3.8	2.9	4	8	4	1.18

4.3.2 Transient durations

In order to characterize the dynamical consequences of the yaw manoeuvre, the first parameter to analyze is τ^*_{ratio}, since this parameter is useful to compare the duration of the yaw manoeuvre with the duration of the induced wake flow and load modifications. Figure 4.15 and figure 4.16 show an intuitive visual way of analyzing τ^*_{ratio}, by plotting $\Delta\tau^*_\theta$ and $\Delta\tau^*_{C_T}$ respectively against the manoeuvre duration $\Delta\tau^*_m$. The values far from the diagonal line indicate a dynamic behaviour of the wake deviation, or of the thrust variation, different from the yaw manoeuvre. If values are below the diagonal, the response to the manoeuvre is faster than the yaw manoeuvre duration. If values are above the diagonal, the response to the manoeuvre is slower than the manoeuvre duration. The results are classified according to the disc porosity level and the yaw manoeuvre direction. In general, wake deviation durations are all around the $\Delta\tau^*_\theta\,(or\,\Delta\tau^*_{C_T}) = \Delta\tau^*_m$ line, except for one outlier (case 11) where the difference can be explained by a higher RMSE for the fitting procedure (due to a more scattered wake center evolution). No significant difference between the wake dynamics and the yaw manoeuvre can be noticed, whatever the disc porosity levels and the flow conditions. In contrast, the thrust variation duration is in general lower than the yaw manoeuvre duration. The influence of the porosity level can be noticed, and in general, cases of negative yaw variation evolve faster than cases of positive yaw variation, especially for porosity level P1. Concerning the cases of higher yaw manoeuvre speed, no clear trend is visible on the effect of porosity and yaw manoeuvre. This may be due to the smaller number of cases analysed, but generally a higher yaw manoeuvre speed does not seem to significantly impact the behaviour of the downstream wind turbine thrust variation. In tables 4.2 and 4.3, the fitting coefficient c that represents the transient variation rate is given. There is a direct relationship between this parameter and the dimensionless transient durations $\Delta\tau^*_\theta$ and $\Delta\tau^*_{C_T}$ deduced from thresholds (section 4.3.1). This fitting parameter together with τ_{lag} will be further investigated in section 4.3.4.

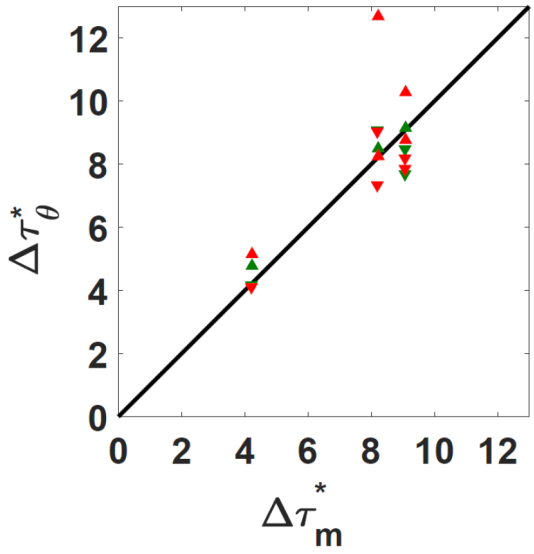

Figure 4.15 – Wake deviation duration versus yaw motion duration. Summary of all the treated cases. Symbols: ▲ positive yaw manoeuvre duration, ▼ negative yaw manoeuvre duration. Colors: red for porosity P1, green for porosity P2.

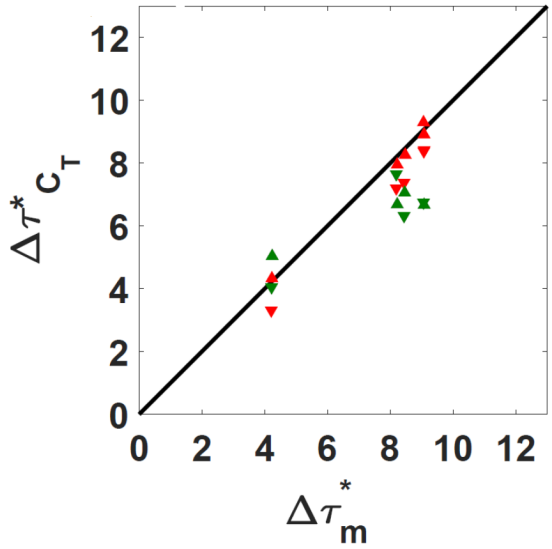

Figure 4.16 – Thrust variation duration versus yaw motion duration. Summary of all the treated cases. Symbols: ▲ positive yaw manoeuvre duration, ▼ negative yaw manoeuvre duration. Colors: red for porosity P1, green for porosity P2.

4.3.3 Transient starts and ends

In order to obtain more detailed knowledge of the timing characteristics and the history of modification, it is important to check τ^*_{start} and τ^*_{end} for wake deviation, available wind power density and thrust variations, since τ^*_{start} values give information about the time delays before the upstream wind turbine wake starts deflecting, before the available wind power density for the downstream wind turbine is modified, and then, before the thrust applied to the downstream wind turbine starts increasing. τ^*_{end} values inform about the delays necessary for the stabilisation of all the variations in the final state .

Figure 4.17 shows a summary of the time parameters, through a timeline representation for the wake deviation, the available wind power density and the thrust variations. The transient duration values are also shown in a parallel plot to facilitate the reading.

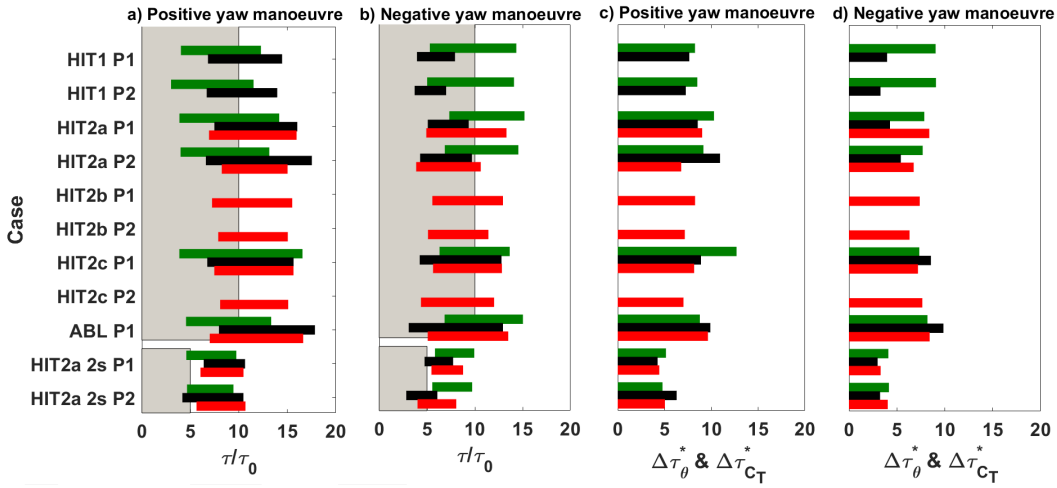

Figure 4.17 – Timeline representation of the wake deviation, the available wind power density and the thrust variations for different porosity levels and flow conditions. For figures a & b, the horizontal bar extremes represent the start and the end of the studied phenomenon. a) Positive yaw manoeuvre main parameters, b) Negative yaw manoeuvre main parameters, c) Positive yaw manoeuvre duration, d) Negative yaw manoeuvre duration. Colors: green = values retrieved by the center wake position, black = values retrieved by the wind power density, red = values retrieved by the thrust variations, gray = expected yaw manoeuvre duration

Several conclusions on the wake dynamics can be drawn :

- In general, the wake deviation transient (green timelines) has slightly shorter duration and starts later for the negative yaw variation than for the positive

one. As explained in section 4.3.1, a time delay between the start of the yaw manoeuvre and the wake deviation is expected since the wake deviation is observed at a certain downstream distance. Air mass needs time to travel from the upstream wind turbine model to the downstream location of interest. This wake transport velocity, or advection velocity, is generally assessed as equal to the free-stream velocity U_{ref} (Trujillo et al. [2011]), but some previous studies also proposed a lower value due to the velocity deficit within the wake of $0.8U_{ref}$ (Machefaux et al. [2015b]), or an average between the free-stream velocity and the wake speed (Bossanyi [2018b], Keck et al. [2014]). This information is checked through the ratio $\frac{U_{adv}}{U_{ref}}$ reported in table 4.2. The ratio is presently close to 1 for a positive yaw manoeuvre, and around 0.8 for a negative yaw manoeuvre.

- A detailed analysis of timing parameters does not provide any evidence of a major effect of the porosity on the wake deviation behaviour.
- Concerning the cases of higher yaw manoeuvre speed, no particular impact of the yaw manoeuvre speed on the wake response is visible.
- Theoretically, the fitting coefficient τ^*_{lag} (Tab.4.2 & 4.3) can be interpreted as a time delay before the transient starts. The relationship between this parameter and τ^*_{start} will be investigated in section 4.3.4 together with the relation between c and the phenomena durations.

Figure 4.17 also presents the transient parameters for the available wind power density deduced from the wake measurement by PIV at the downstream location where the second wind turbine model can be installed (black timelines). Systematic differences in the timing parameters of this available wind power density compared to the wake center deviation are visible, with shorter starting time delays for the positive yaw manoeuvre and longer ones for the negative yaw manoeuvre. As this value is obtained by a space integration of the wake velocity, it illustrates that the modification of the overall wake velocity field can be different from the modification of the wake center position, which is a more local indicator and for which the range of deviation to be captured is very small. This available wind power density dynamics also illustrates how the incoming flow will dynamically impact the downstream wind turbine model and modify its corresponding thrust. It was therefore expected that the thrust transient starts and ends (red timelines) will be systematically later than the available wind power ones. The additional time delay between both would represent the wind turbine model response to the modification of the incoming flow. This trend is not verified in the present results since both situations can be observed. The reasoning was based on the hypothesis that the induction zone of the downstream wind turbine model does not

play a role in its dynamic process which is clearly not true. The thrust variation starts later for a positive yaw manoeuvre than for a negative one. This trend is in opposition with the wake deviation behavior and contradicts the assumption that one can use the same time delay due to advection for the upstream wind turbine wake deviation and for the downstream wind turbine thrust variation.

4.3.4 Interpretation fitting law coefficients

In this section, an evaluation of the fitting coefficients of the exponential law is done with respect to the timing parameters used for the transient analysis. In figure 4.18, the wake deviation duration $\Delta\tau_\theta^*$ is plotted against the c coefficient of the fitting law for both positive and negative manoeuvre and porosities levels, while in figure 4.19, the same analysis is done for the thrust variation duration $\Delta\tau_{CT}^*$.

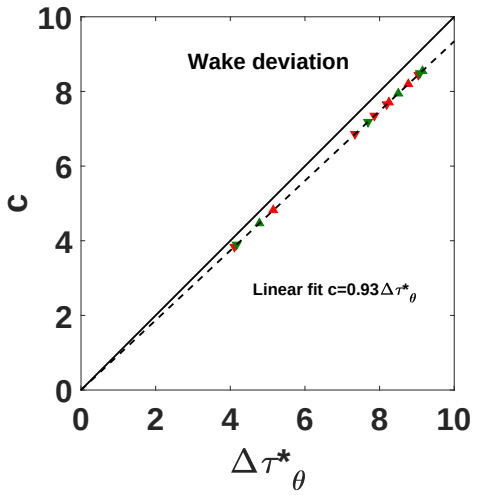

Figure 4.18 – Wake deviation duration $\Delta\tau_\theta^*$ versus the c fitting coefficient of the exponential laws. Summary of all the treated cases. Symbols: ▲ positive yaw manoeuvre duration, ▼ negative yaw manoeuvre duration. Colors: red for porosity P1, green for porosity P2.

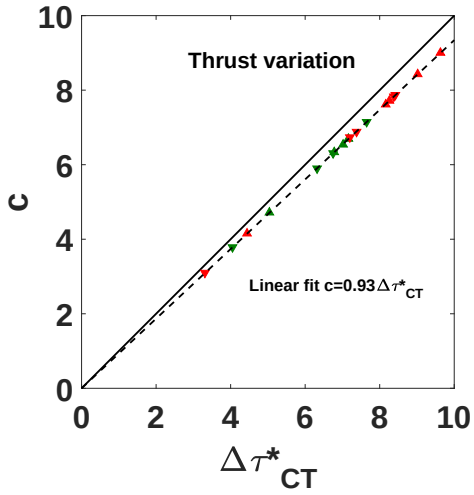

Figure 4.19 – Thrust variation duration $\Delta\tau^*_{CT}$ versus the c fitting coefficient of the exponential fitting laws. Summary of all the treated cases. Symbols: ▲ positive yaw manoeuvre duration, ▼ negative yaw manoeuvre duration. Colors: red for porosity P1, green for porosity P2.

Generally c has a very clear correlation with the duration for both wake deviation and thrust variation cases. Indeed, it possible to retrieve by linear fitting imposing the fit law to pass through the origin, a linear relationship that links c to both wake deviation and thrust variation duration. This linear fitting was done separately for the wake deviation and thrust variation but leaded to the same slope of 0.93:

$$c = 0.93\Delta\tau^* \tag{4.19}$$

where $\Delta\tau^*$ is either the wake deviation duration $\Delta\tau^*_\theta$ either the thrust variation duration $\Delta\tau^*_{CT}$. These results confirm the robustness of the fit coefficient c although the reason that keep c constantly lower than the phenomenon duration has still to be investigated. In figure 4.20, the start of the wake deviation τ^*_{start} is plotted against the τ^*_{lag} coefficient of the exponential fitting laws for both positive and negative manoeuvre and porosity levels. In figure 4.21, the same analysis is done for the start of the thrust variation.

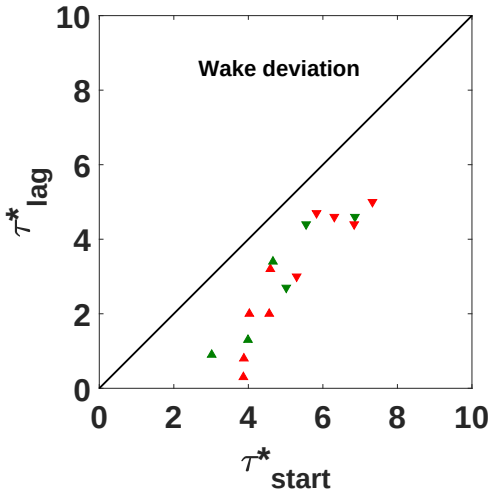

Figure 4.20 – Wake deviation start τ^*_{start} versus the τ^*_{lag} fitting coefficient of the exponential laws. Summary of all the treated cases. Symbols: ▲ positive yaw manoeuvre duration, ▼ negative yaw manoeuvre duration. Colors: red for porosity P1, green for porosity P2.

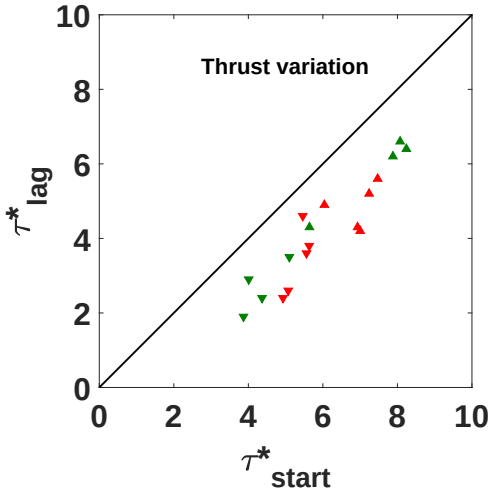

Figure 4.21 – Thrust variation start τ^*_{start} versus the τ^*_{lag} fitting coefficient of the exponential laws. Summary of all the treated cases. Symbols: ▲ positive yaw manoeuvre duration, ▼ negative yaw manoeuvre duration. Colors: red for porosity P1, green for porosity P2.

Several conclusions on the τ^*_{lag} coefficient can be done:

- Although it can be observed an higher scatter than for the c coefficient, τ^*_{lag} also shows a detectable trend.
- The thrust data seems to have lower scatter than the wake deviation data and this could be related to the higher time resolution of the load measurements.
- There is generally a bias between the values that oscillate between 1 and 2 τ_0. This could be partially attributed to the threshold value used for the τ^*_{start} determination.

In conclusion, the fitting laws implemented for the dynamic yaw conditions seem to be exploitable for a generalisation of a law describing the transition phenomenon. Especially, the c coefficient has proven to be quite robust to be used in an empirical law to model the transient. Regarding the τ^*_{lag} coefficient, although its physical signification is clear, its implementation in an empirical law demands more caution. Indeed, the measured values do not follow a trend as clear as for the duration coefficient. This is probably due to the specificity of this parameter which is directly linked to the start of the phenomenon, and consequently it is more sensible to dispersion. Nevertheless, τ^*_{lag}, being representative of advection, could be adjusted by making some simple advection hypothesis. The higher robustness of the c parameter, being representative of the transient duration, can probably due to the fact that it damps better the scatter of τ^*_{start} and τ^*_{send} which are generally concordant (both either overestimated or underestimated). At this stage, further exploitation of these data and studies have to be done in view of the implementation of an empirical model.

Chapter 5

Production dynamics of two full scale wind turbines

This chapter has been subject of the publication "Experimental analysis of time delays in wind turbine wake interactions" Macrì et al. [2020]. Due to the fact that the publication substantially collects an exhaustive review of this part of the PhD work, here it is essentially reported with minor modifications. A post-processing of SCADA data acquired with a high sampling frequency on two neighbouring wind turbines is performed through inter-correlation functions in order to assess the time delays between the wind turbine responses, depending on wind direction and wind speed.

5.1 Introduction & work objectives

The dynamic properties of the physical phenomena playing a role in the wake steering or induction control are now taken into account in some wind farm control models Machefaux et al. [2015a] but some parameters need to be refined. For instance, the time delays between a manoeuvre of an upstream wind turbine and its effect on the downstream one can be approached by a pure advection hypothesis, assuming that the time delay is equal to the time for the air masses advected at the free wind speed to transit from the upstream to the downstream wind turbine. Some previous works suggested to use a proportion (80 %) of the free wind speed as advection speed Machefaux et al. [2015a], or an average between the free wind speed and the wake speed Bossanyi [2018a]. Furthermore, the wind turbine dynamic response will also impact the overall time delay. Consequently, this parameter needs to be further studied and better quantified. Through the post processing of a field database collected during the French national project SMARTEOLE on two full-scale wind turbines, the overall time delay between the

dynamics of two wind turbines will be assessed. Correlation functions between both wind turbine power time series acquired at a sampling frequency of 1Hz are performed and time delays between the wind turbine responses are assessed. By classifying the set of time series according to the wind direction and the wind turbine operating point, the influence of the wake interaction on the time delay between the wind turbine responses will be studied.

5.2 Approach & methods

5.2.1 Experimental setup

The measurement campaign took place on a wind farm (WF) located in the north of France (Figure 5.1) with measurements done between January 2017 and November 2018 and already used in Garcia et al. [2019] and Duc et al. [2019]. The WF (Engie Green owned) is called *Sole du Moulin Vieux* (SMV) and is located on the western limit of the Ablaincourt-Pressoir municipality. It is made of seven wind turbines (WTs) named SMV1 to SMV7 which are sited from north to south and spaced approximately 4.3 D apart. These SENVION MM82 WTs (guaranteed power curve in figure 5.3) have a diameter (D) and hub height (HH) of D = 82 m and HH = 80 m; and their nominal power is 2050 kW which is reached for a nominal wind speed of 14.5 ms^{-1}, while their cut-in wind speed is 3.5 ms^{-1}. The site is not complex, with a very flat terrain composed mainly of grasslands, with the exception of a small forest located south of the farm. The long term observed wind, illustrated on the wind rose of figure 5.2, shows that the prevailing wind directions comes mainly from the south west. This corresponds mostly to the alignment between turbines SMV5 and SMV6 which is 207° with respect to the north, consequently this layout makes it possible to observe a very strong and frequent wake effect between these two turbines.

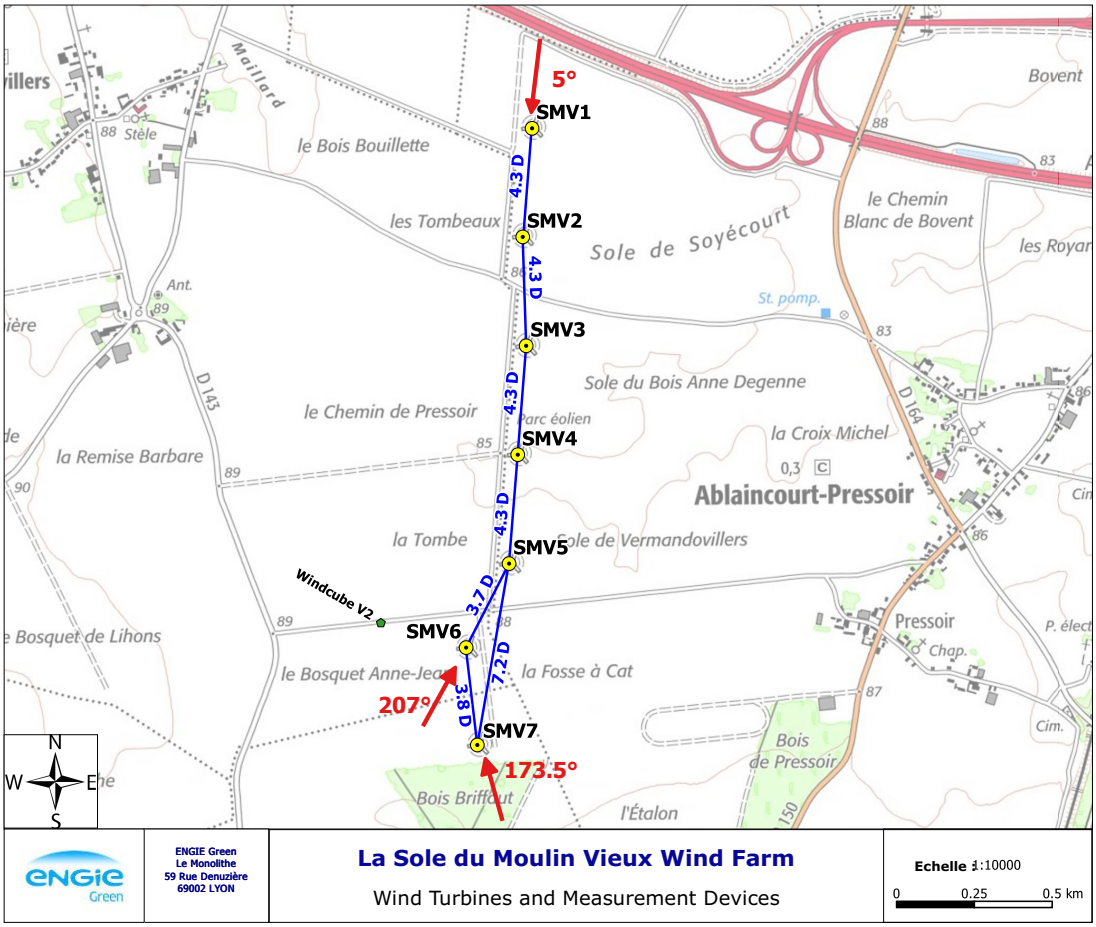

Figure 5.1 – *Layout of the SMV wind farm and location of wind measurement devices. Inter-distances between the wind turbines are expressed in rotor diameters (with D=82 m), while red arrows indicate the wind direction with maximum wake interaction between the turbines of interest. The location of the ground based lidar Windcube V2 is also indicated.*

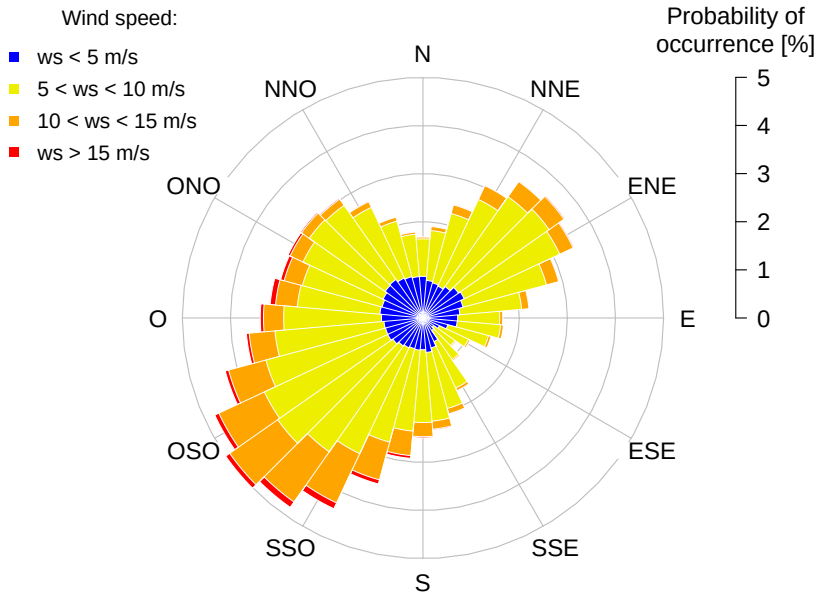

Figure 5.2 – *Long term observed wind rose. Taken from Duc et al. [2019]*

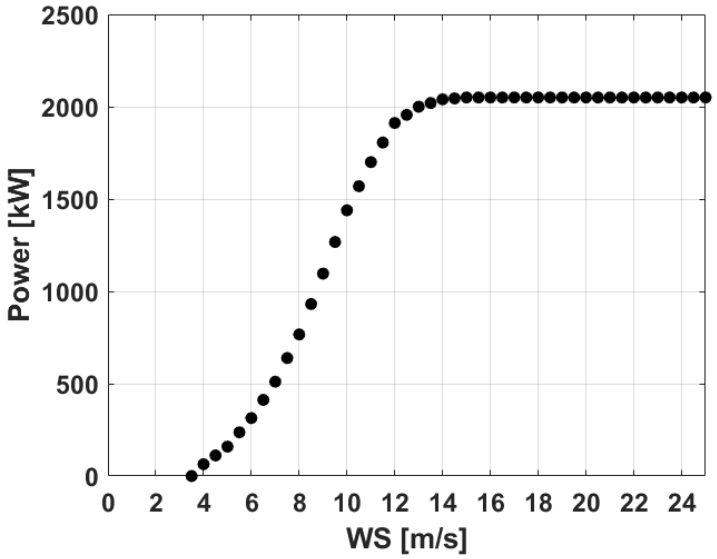

Figure 5.3 – *Senvion MM82 guaranteed power curve*

5.2.2 Identification of reference wind turbines

A crucial point of this work was the Supervisory Control and Data Acquisition (SCADA) time series classification according to wind direction and wind speed. Indeed measurements of two different wind turbines in the same WF can be discordant for multiples reasons, so an inaccurate choice of the reference WT can trick the classification. Concerning the wind speed, the presence of the wake of an other WT can affect the measurements, while for wind direction, some undesired bias on the vane position can false the measurements. In order to reduce the possible sources of errors in the estimation of the wind characteristics, the SCADA data-set quality was tested taking as a reference a ground based lidar (Windcube V2) whose location is indicated on figure 5.1. Indeed, over a quite large period of measurement (May 2017 - Jan 2018), both SCADA and Windcube data were available. The lidar provides 10min-averages of wind speed and direction at different heights. The SCADA average wind measurements for the same ten minutes intervals were compared to the lidar measurements at the altitude 80 m only, to be consistent with the wind turbine hub heights. For each wind turbine in the farm, the difference in measured wind speed and direction was calculated for each sample, and then this data-set was classified according to the Windcube wind direction and binned over 20° sector, giving a single mean error value per wind turbine for each direction sector. Some considerations regarding the lidar position have to be done before analyzing the results. Indeed, according to the farm layout in figure 5.1, the lidar is generally in the wake of one or more WTs for the wind sectors [20°:180°]. This affects its measurements, especially concerning the wind speed, and thus those sectors are disregarded in the following analysis. The first evaluation was focused on the wind direction measurement: this measurement being less sensitive to wake effects it was chosen to establish a single reference WT in order to proceed with the classification of the entire SCADA data-set over wind sectors. The wind direction was evaluated looking at the mean absolute error (MAE) between the seven WT SCADA measurements and the Windcube. Figure 5.4 shows the result of this analysis. Looking at the MAE, and taking into consideration the position of the Windcube, the WT SMV3 is a good choice as reference since its MAE is generally among the smaller for most of the bins, and in particular for the sector of maximal wake interaction. Focusing on the wind sector [180°:340°] (Windcube upwind) it shows a maximum error below 8°.

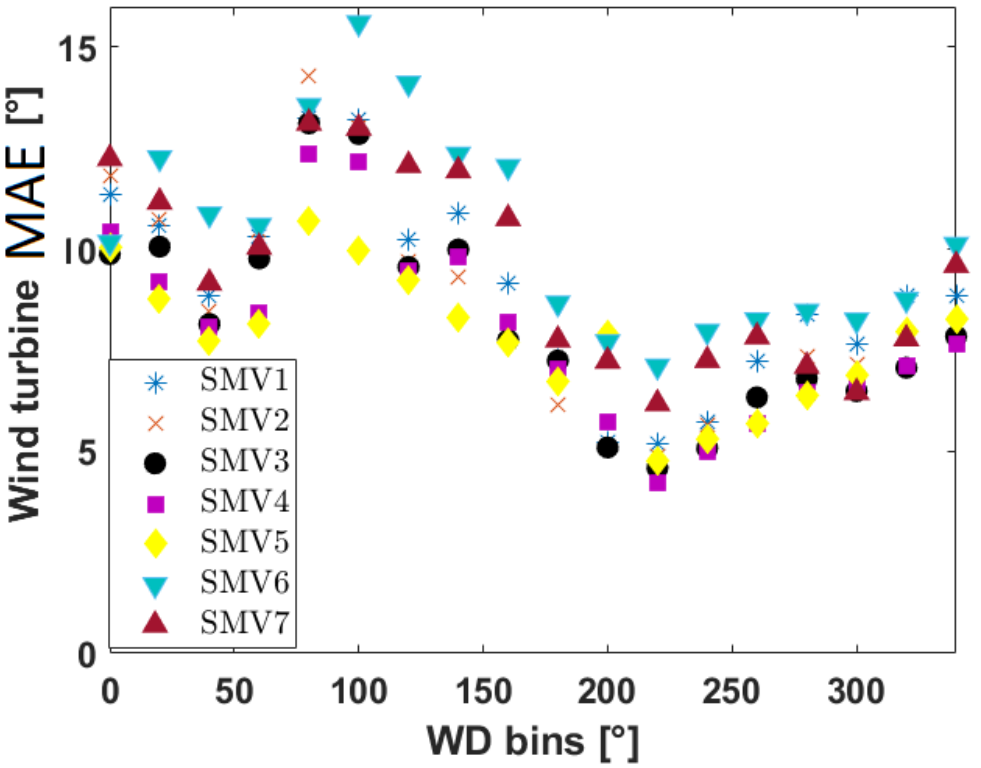

Figure 5.4 – *SCADA wind direction measurements mean absolute errors (MAE)*

The same kind of evaluation was done for the wind speeds. The percentage error of the SCADA wind speed measurements with respect to the Windcube was calculated for each sector. Figure 5.5 shows the results of the analysis. Three different WT references has been taken according to the wind sectors in order to consistently take into account the wake effects within the wind farm. Indeed, looking at sector [220°:320°], where there are no supposed wake interactions, SMV4 represents a good choice (measurement error generally less than 2%) as a reference for this sector. Just by symmetry considerations, SMV4 has been also chosen as reference for the sector [40°:140°] since the Windcube is an unreliable reference for this sector. Then according to the farm layout and the observed results, it is reasonable to take SMV1 as reference for northern wind sectors [340°:20°] and respectively SMV7 for southern sectors [160°:200°].

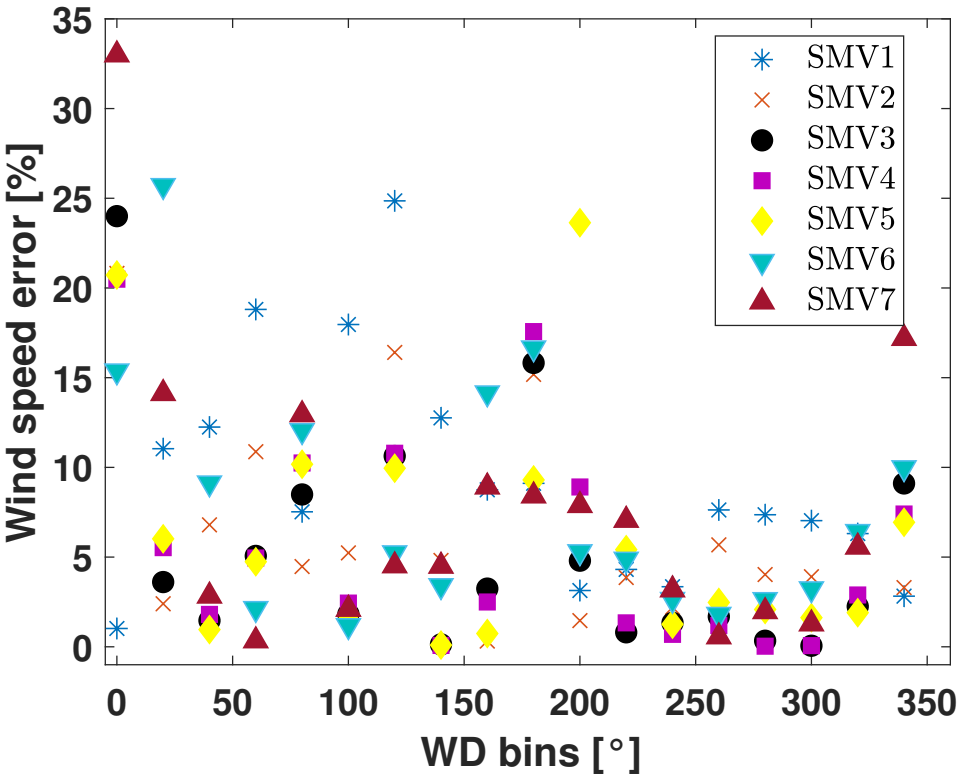

Figure 5.5 – *SCADA wind speed percentage mean errors*

The table 5.1 recaps the chosen reference wind turbines for each wind sector.

Table 5.1 – Summary of the reference turbines chosen to determine the incoming wind speed and wind direction assessment, depending on the wind direction sector.

Wind direction sector	**Reference wind turbine**	
	Wind speed	**Wind direction**
North [340°; 20°]	SMV1	SMV3
East [40°; 140°]	SMV4	
South [160 ; 200°]	SMV7	
West [220; 320°]	SMV4	

5.2.3 Data filtering & processing

Once determined the proper references for the estimation of wind characteristics it was possible to process the whole SCADA database. The database contains 10min-averaged and standard deviation data for each WT and high frequency

sampled data (1Hz) for WT SMV5 & SMV6 only. Before using the inter-correlation functions on the active power signals of these two turbines for each 10min-interval, some filtering had to be made. The filters that were applied to the data are listed below:

1. Both wind turbines had to be operational.
2. No movement of the nacelle position of both turbines had to be observed.
3. Any abnormal turbine behavior (such as curtailment) had to be observed.
4. Only periods with a wind speed between 10 ms^{-1} and 12 ms^{-1} (measured at the identified reference wind turbine) were kept in the analysis. This is done in order to observe both high wake effects and sufficiently high power production at the downstream turbine.

Furthermore a data quality check was applied to the 1Hz active power time series. Indeed, to properly study the correlation it was necessary to have a continuous sampling (600 samples for 10 minutes period at 1Hz) without gaps and duplicated values. So, over each 10min-period, the high frequency time series were analyzed to remove duplicates and detect the presence of missing data in the time-series. Any 10min-time series with gaps longer than one second were rejected, as concern the others, contingent gaps were filled by linear interpolation.

5.2.4 Calculation of inter-correlations between the turbines

After the data filtering and processing, it was possible to proceed on the calculation of the inter-correlation levels for each selected period. Any linear trends in the power signals was first removed in order to focus on the power fluctuations of both wind turbines. The inter-correlation coefficient versus the time delay τ between the de-trended power signals P'_{SMV6} and P'_{SMV5} was calculated as in eq(5.1):

$$R_{P_5P_6}(\tau) = \frac{\int P'_{SMV6}(t)P'_{SMV5}(t-\tau)dt}{\sqrt{\overline{P'_{SMV6}{}^2}}\sqrt{\overline{P'_{SMV5}{}^2}}} \tag{5.1}$$

The maximal value of $R_{P_5P_6}(\tau)$ was calculated for each correlation function. Periods with correlation peaks below 0.5 were rejected, while for the others the time delay τ correspondent to the peak was retrieved. The filtered correlation statistics were binned over 20° wind sector (using the reference wind turbine SCADA data). Sector with less than 10 samples were rejected because they were considered as non-statistically representative. In the end, after all these restrictive filters, only five sectors corresponding to the most prevailing wind directions were obtained (see figure 5.2).

5.3 Results

Figure 5.6 shows the average of the inter-correlation coefficients between the wind turbine power signals measured on SMV5 and SMV6 over wind direction sectors of 20°. For an easier representation, the absolute values of the inter-correlations statistics are shown. Indeed, according to the wind sector, SMV6 can be either upwind or downwind compared to SMV5 causing negative inter-correlation statistics.

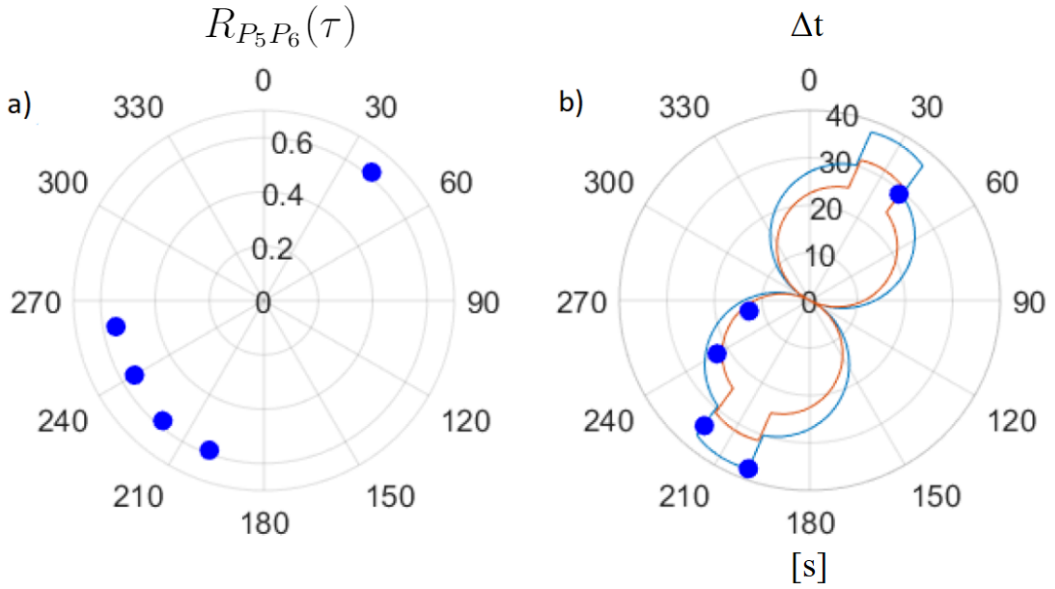

Figure 5.6 – Polar plot of inter-correlation coefficients (a) and time responses in seconds (b) between the 1Hz power signals of wind turbine SMV6 and SMV6 with wind speed between $10ms^{-1}$and $12ms^{-1}$. Dots represent the inter-correlation statistics, colored lines the T_{adv} estimation thresholds.

Results show inter-correlation coefficients around 0.6 for all the sectors matching the filtering conditions, independently of the wake interaction presence. Figure 5.6b shows the average delay between the active power signals variations of SMV5 and SMV6 obtained by the maximum of inter-correlations. As a general approach, this work aims to evaluate whether this time delay could be related to a physical phenomenon, in particular the advection time between the two wind turbines. As possible evaluation of the quality of the results, it was chosen to compare the data with a classical estimation of the advection time based on the wind speed. The advection time, intended as the time for the air masses to transit from the location of the upstream turbine to the position of the downstream one,

was so estimated by the measurement of the reference SCADA wind speed. As mentioned earlier, one solution to estimate the advection time in wake interaction conditions is to use a portion (80%) of the free stream velocity (U_∞) as done in Machefaux et al. [2015a]. Having considered in this work only wind speeds between 10 ms^{-1} and 12 ms^{-1} the advection time (T_{adv}) corresponding to these thresholds was estimated. Figure 5.7 schematize the calculation of the streamwise distance ΔX between SMV5 & SMV6. Knowing the geometrical spacing between the wind turbines WT_{Dist} = 3.7D (at 207°) and the wind direction WD, by simple trigonometry, it is possible to retrieve ΔX as in eq(5.2). Then ΔX is divided for the advection speed U_{adv} to retrieve T_{adv} (represented by the colored lines in figure 5.6b). Concerning the advection speed, for the wake interactions sectors [200°:220°] and [20°:40°] it was taken $0.8U_\infty$ while for the other sectors just U_∞.

$$\Delta X = WT_{Dist} cos(WD - 207^\circ) \tag{5.2}$$

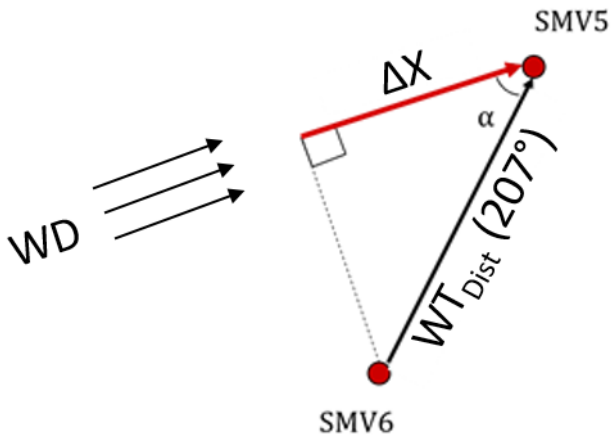

Figure 5.7 – Determination of the streamwise distance ΔX ($\alpha = WD - 207^\circ$)

Finally looking at the time response results, it can be found a general agreement between the classical estimation of T_{adv} and the time response between the wind turbines. Focusing on the wake regions, the results show as the wake interaction affects the wind turbine dynamics. Indeed, the presence of the wake not only (as well known) decreases the power availability on the downstream turbine, but reduces its time response and this reduction can be retrieved by the evaluation of the power time series such as the aerodynamic advection time. The importance of the evaluation of this parameter directly by the power time series is given by the fact that these are generally the most reliable SCADA data and they can be easily integrated in the machine control system.

5.4 Conclusion

A post-processing of SCADA data acquired with a high sampling frequency on two neighbouring wind turbines is performed through inter-correlation functions in order to assess the time delays between the wind turbine responses depending on wind direction and wind speed. Furthermore the influence of the level of wake interactions is discussed in terms of inter-correlation statistics showing a general accordance with the classical advection considerations. The obtained results show that this kind of analysis can contribute to refine the dynamic parameters of the wind farm control models. For several reasons (among other the storage) it is not trivial to have a large 1Hz database available. So the purpose of this work was to evaluate the potentiality of this approach on the exploitation of the power measurements to retrieve the wind turbine response especially in wake interactions conditions. Therefore, this work has to be considered as a preliminary study. Right now, another acquisition campaigns is on going with $1Hz$ SCADA being recorded on all wind turbines in the farm. Hopefully, the study of this new database will help in pushing further this first analysis.

Chapter 6

Conclusions & perspectives

The objective of this thesis was to provide information on the wake dynamics of a wind turbine model with particular focus on the wake behaviour during the execution of a yaw manoeuvres. In order to achieve this goal the aerodynamic characterisation of the wake of a wind turbine model and its effect on the load of a downstream wind turbine model consequent to a dynamic positive (misalignment scenario) or negative (realignment scenario) yaw variation were experimentally studied for different incoming flow conditions, Reynolds scales and induction factors.

In chapter 1 the global research context of wind energy with particular focus on the wake interactions and wind farm control research topics was shortly introduced.

Chapter 2 presented a non exhaustive literature review on the state-of-the-art concerning wind turbine and wind farm aerodynamics, with particular attention on the wake properties, wake engineering models and wind farm control. The wind turbine modelling used on the experiments of this thesis, based on the actuator disc concept, was described as well the principal wake properties with focus on the skewed wake conditions. Moreover the most common wind farm control strategies were introduced.

In chapter 3, a detailed description of the three experimental set-ups used for this study as well the two wind tunnels of $PRISME$ laboratory were described with particular focus on the generated flow conditions: two campaigns in homogeneous isotropic turbulent flow (HIT) conditions and one in Atmospheric Boundary Layer (ABL) conditions. The models used for the wind turbine representation were described and their choice was motivated. A detailed description of experimental protocol as concerns to disc and yaw manoeuvre scaling, wake tracking (*Stereo*

PIV acquisition protocol and data post processing) and downstream wind turbine model load variation measurements (6 DOF aerodynamic balance acquisition protocol and data post processing) was provided. Particular attention was put on the wind turbine and yaw manoeuvre downscaling based on the WT size and realistic manoeuvrer speed. As a consequence of this approach, the manoeuvre duration (scaled according to a full scale condition) is multiples of the aerodynamic rotor time scale (τ_0) leading to the analysis of the relatively slow dynamics of the wake steering strategy actuation transient on an operational wind turbine. Moreover an exhaustive description of the most common wake center determination methodologies and the motivations that lead to the the choice of the one based on the available wind power density at position of a hypothetical downstream wind turbine model was provided.

In chapter 4 the wake deviation, available wind power and thrust variations were analysed. The wake deviation angle, the available wind power and the thrust coefficient of the downstream wind turbine model were chosen as a metrics and were first analysed as a function of different static yaw angles. Then, before the analysis of the consequence of a dynamic yaw variation on these parameters, an assessment of the aerodynamic performances of the two wind turbine models was done using the classical *Momentum theory* equations and compared with the performance of two wind turbines operating in optimal conditions (no yaw, no wake interaction). Results show that according to *Momentum theory* equations and classical definition of wind farm performances, the wake steering does not seem to have a positive effect on the overall wind turbine performance. This conclusion is contradictory with the literature on full scale wind farm experiments on wake steering and the reproduction in wind tunnel of wake steering via rotating wind turbine models. Therefore these results should suggest the non-feasibility of performance analysis by the use of the actuator disc theory for the evaluation of such wind farm control strategy. After the considerations on the wind farm performance, the duration, start and end of the temporal response of the metrics to a dynamic yaw variation were estimated and compared. The main results are summarized here. Overall results do not show any noticeable influence of the flow conditions (Homogeneous Isotropic Turbulent flows or Atmospheric Boundary Layer flow) or of the Reynolds numbers on the static and dynamical properties of the different metrics. The influence of the degree of physical modelling of the wind turbine (porous disc versus rotating wind turbine model) on the results had not been studied since it was assumed that this feature does not play a major role in the yawed far-wake dynamics, but this question needs to be further investigated. Concerning the characterisation of the magnitude of the wake deviation in static yaw conditions, results show that the wake deviation is one order of magnitude

lower than the yaw increment and that the relationship between the wake deviation and the yaw angle is non linear, as previously found in the literature. In the case of a higher porosity level, the thrust increment is much lower than in the case of lower porosity. However, while a relevant influence of the porosity on the wake deviation angle and thrust magnitude of the downstream wind turbine model is found in static conditions, no significant influence of porosity is observed on the wake and load dynamics. On the other hand, the analysis of the three metrics reveals different temporal characteristics depending on whether yaw manoeuvre is positive or negative. In general, the wake deviation transient has slightly shorter duration and starts later for the negative yaw variation than for the positive one. A proper knowledge of such effects helps to determine the time necessary for the wake steering to totally develop. On the contrary, the thrust variation starts later for the positive yaw manoeuvre than for the negative one. The influence of the yaw manoeuvre speed was tested and doubling the yaw manoeuvre speed does not seem to influence the wake or load dynamics. Finally, the study shows that the same dynamical properties of the wake of the upstream wind turbine and load variation of the downstream wind turbine cannot be generalised to any yaw variation configurations, and that the advection velocity should be assumed to be different according to the yaw manoeuvre direction. A first step in proposing fitting coefficients was made in order to support a dynamic model of the wake deviation or the thrust for positive or negative yaw variations. The fitting laws implemented for the dynamic yaw conditions seem to be exploitable for a generalisation of a law describing the transition phenomenon. Especially, the c coefficient has proven to be quite robust to be used in an empirical law. Regarding the τ^*_{lag} coefficient, although its physical signification is clear, its implementation in an empirical law demands more caution. Indeed, the measured values does not follow a trend as clear as for the duration coefficient. This is probably due to the specificity of this parameter which is directly linked to the start of the phenomenon, and consequently it is more sensible to its dispersion. Nevertheless, τ^*_{lag}, being representative of advection, could be adjusted by making some simple advection hypothesis. On the other hand, the c parameter, being representative of the transitory duration, can better damp the fluctuations of τ^*_{start} and τ^*_{end} which are generally concordant (both either overestimated or underestimated). At this stage, further exploitation of these data and studies have to be done in view of the implementation of an empirical model. Indeed, an empirical model capable to predict the wake and load variation dynamics would be beneficial if implemented in wind farm control models providing information about wake and downstream wind turbine loads time response to the upstream wind turbine yaw manoeuvre. A proper knowledge of these time responses and of their variability according to the kind of yaw manoeuvre would be important for the tuning of dynamic wind farm control models,

helping to improve their accuracy. Although during this PhD work different wind turbine model scales, porosity levels and flow conditions were tested, it would be interesting to test higher porosity levels to reproduce situations of higher wake signature (higher thrust coefficient) as well as test also with rotating wind turbine models to see whether the WT modelling degree is important on the wake dynamics. An other interesting perspective concerning the analysis of the load variations would be to have both the upstream and downstream wind turbine models placed on synchronized aerodynamic balances in order to properly evaluate and compare the load dynamics variation of both models. These are just a few possible studies to further investigate this phenomenon whose comprehension is becoming the more and more crucial to improve wind farm production optimization.

Chapter 5 presented a preliminary work on the full-scale analysis of time delays in wind turbine wake interactions. A post-processing of SCADA data acquired with a high sampling frequency on two neighbouring wind turbines was performed through inter-correlation functions in order to assess the time delays between the wind turbine responses, depending on wind direction and wind speed. Furthermore the influence of the level of wake interactions was discussed in terms of inter-correlation statistics showing a general accordance with the classical advection considerations. The obtained results showed that this kind of analysis can contribute to refine the dynamic parameters of the wind farm control models. For several reasons (among other the storage) it is not trivial to have a large 1Hz database available. So the purpose of this work was to evaluate the potentiality of this approach on the exploitation of the power measurements to retrieve the wind turbine response especially in wake interactions conditions.

Bibliography

Characteristics of atmospheric turbulence near the ground. Part 2: Single point data for strong winds (neutral atmosphere). Unknow, October 1985.

Mahdi Abkar and Fernando Porté-Agel. Influence of atmospheric stability on wind-turbine wakes: A large-eddy simulation study. *Physics of fluids*, 27(3): 035104, 2015.

Aliza Abraham, Luis A Martinez-Tossas, and Jiarong Hong. Mechanisms of dynamic near-wake modulation of a utility-scale wind turbine. *arXiv preprint arXiv:2006.16321*, 2020.

MS Adaramola and P-Å Krogstad. Experimental investigation of wake effects on wind turbine performance. *Renewable Energy*, 36(8):2078–2086, 2011.

John F Ainslie. Calculating the flowfield in the wake of wind turbines. *Journal of Wind Engineering and Industrial Aerodynamics*, 27(1-3):213–224, 1988.

Matthew L Aitken, Branko Kosović, Jeffrey D Mirocha, and Julie K Lundquist. Large eddy simulation of wind turbine wake dynamics in the stable boundary layer using the weather research and forecasting model. *Journal of Renewable and Sustainable Energy*, 6(3):033137, 2014.

P Henrik Alfredsson and JA Dahlberg. A preliminary wind tunnel study of windmill wake dispersion in various flow conditions, part 7. 1979.

Jennifer Annoni, Paul Fleming, Andrew K Scholbrock, Jason M Roadman, Scott Dana, Christiane Adcock, Fernando Porte-Agel, Steffen Raach, Florian Haizmann, and David Schlipf. Analysis of control-oriented wake modeling tools using lidar field results. *Wind Energy Science (Online)*, 3(NREL/JA-5000-72767), 2018.

Sandrine Aubrun, Philippe Devinant, and Guillaume Espana. Physical modelling of the far wake from wind turbines. application to wind turbine interactions. In *Proceedings of the European wind energy conference, Milan, Italy*, pages 7–10, 2007.

Sandrine Aubrun, Stéphane Loyer, PE Hancock, and Paul Hayden. Wind turbine wake properties: Comparison between a non-rotating simplified wind turbine model and a rotating model. *Journal of Wind Engineering and Industrial Aerodynamics*, 120:1–8, 2013.

Sandrine Aubrun, Majid Bastankhah, Raúl Bayoán Cal, Boris Conan, R Jason Hearst, D Hoek, Michael Hölling, M Huang, C Hur, B Karlsen, et al. Round-robin tests of porous disc models. In *Journal of Physics: Conference Series*, volume 1256, page 012004. IOP Publishing, 2019.

S Baidya Roy, Stephen Wilson Pacala, and RL Walko. Can large wind farms affect local meteorology? *Journal of Geophysical Research: Atmospheres*, 109(D19), 2004.

Robert W Baker and Stel N Walker. Wake measurements behind a large horizontal axis wind turbine generator. *Solar Energy*, 33(1):5–12, 1984.

Sophie Baleriola. *Etude expérimentale de la modification des charges aérodynamiques sur pale d'éolienne par du contrôle d'écoulement actif*. PhD thesis, 2018.

Rebecca Jane Barthelmie, K Hansen, Sten Tronæs Frandsen, Ole Rathmann, JG Schepers, W Schlez, J Phillips, K Rados, A Zervos, ES Politis, et al. Modelling and measuring flow and wind turbine wakes in large wind farms offshore. *Wind Energy: An International Journal for Progress and Applications in Wind Power Conversion Technology*, 12(5):431–444, 2009.

RJ Barthelmie, L Folkerts, FT Ormel, P Sanderhoff, PJ Eecen, O Stobbe, and NM Nielsen. Offshore wind turbine wakes measured by sodar. *Journal of Atmospheric and Oceanic Technology*, 20(4):466–477, 2003.

Jan Michael Simon Bartl, Franz Volker Mühle, Jannik Schottler, Lars Roar Sætran, Joachim Peinke, Muyiwa S Adaramola, and Micheal Holling. Wind tunnel experiments on wind turbine wakes in yaw: effects of inflow turbulence and shear. 2018.

Majid Bastankhah and Fernando Porté-Agel. A new analytical model for wind-turbine wakes. *Renewable Energy*, 70:116–123, 2014.

Majid Bastankhah and Fernando Porté-Agel. Experimental and theoretical study of wind turbine wakes in yawed conditions. *Journal of Fluid Mechanics*, 806: 506–541, 2016a.

Majid Bastankhah and Fernando Porté-Agel. Experimental and theoretical study of wind turbine wakes in yawed conditions. *Journal of Fluid Mechanics*, 806: 506, 2016b.

LH Benedict and RD Gould. Towards better uncertainty estimates for turbulence statistics. *Experiments in fluids*, 22(2):129–136, 1996.

Hans Georg Beyer, Thomas Pahlke, Wolfgang Schmidt, Hans-Peter Waldl, and Ubbo de Witt. Wake effects in a linear wind farm. *Journal of Wind Engineering and Industrial Aerodynamics*, 51(3):303–318, 1994.

Frédéric Blondel and Marie Cathelain. An alternative form of the super-gaussian wind turbine wake model. *Wind. Energy Sci. Discuss*, 2020:1–16, 2020.

Sjoerd Boersma, Bart Doekemeijer, Mehdi Vali, Johan Meyers, and Jan-Willem

van Wingerden. A control-oriented dynamic wind farm model: Wfsim. *Wind Energy Science*, 3(1):75–95, 2018.

Ervin Bossanyi. Combining induction control and wake steering for wind farm energy and fatigue loads optimisation. In *Journal of Physics: Conference Series*, volume 1037, page 032011. IOP Publishing, 2018a.

Ervin Bossanyi. Combining induction control and wake steering for wind farm energy and fatigue loads optimisation. In *J. Phys. Conf. Ser*, volume 1037, page 032011, 2018b.

Ervin Bossanyi and Tiago Jorge. Optimisation of wind plant sector management for energy and loads. In *2016 European Control Conference (ECC)*, pages 922–927. IEEE, 2016.

Tony Burton, Nick Jenkins, David Sharpe, and Ervin Bossanyi. *Wind energy handbook*. John Wiley & Sons, 2011.

Leonardo P Chamorro and Fernando Porté-Agel. Effects of thermal stability and incoming boundary-layer flow characteristics on wind-turbine wakes: a wind-tunnel study. *Boundary-layer meteorology*, 136(3):515–533, 2010.

M Churchfield, Qi Wang, A Scholbrock, T Herges, T Mikkelsen, and M Sjoholm. Using high-fidelity computational fluid dynamics to help design a wind turbine wake measurement experiment. In *Journal of Physics. Conference Series*, volume 753. National Renewable Energy Lab.(NREL), Golden, CO (United States), 2016.

Nicolas Coudou, S Buckingham, and J van Beeck. Experimental study on the wind-turbine wake meandering inside a scale model wind farm placed in an atmospheric-boundary-layer wind tunnel. In *J Phys Conf Ser*, volume 854, page 012008, 2017.

Nicolas Coudou, Maud Moens, Yves Marichal, Jeroen Van Beeck, Laurent Bricteux, and Philippe Chatelain. Development of wake meandering detection algorithms and their application to large eddy simulations of an isolated wind turbine and a wind farm. In *Journal of Physics: Conference Series*, volume 1037, 2018.

JO Counihan. Adiabatic atmospheric boundary layers: a review and analysis of data from the period 1880–1972. *Atmospheric Environment (1967)*, 9(10): 871–905, 1975.

A Crespo and J Hernández. A numerical model of wind turbine wakes and wind farms. In *European wind energy conference EWEC, Rome, Italy*, volume 2, pages 111–115, 1986.

A Crespo, J Hernandez, E Fraga, and C Andreu. Experimental validation of the upm computer code to calculate wind turbine wakes and comparison with other models. *Journal of Wind Engineering and Industrial Aerodynamics*, 27(1-3): 77–88, 1988.

Antonio Crespo, J Hernandez, and Sten Frandsen. Survey of modelling methods for wind turbine wakes and wind farms. *Wind Energy: An International Journal for Progress and Applications in Wind Power Conversion Technology*, 2(1):1–24, 1999.

Thomas Duc, Olivier Coupiac, Nicolas Girard, Gregor Giebel, and Tuhfe Göçmen. Local turbulence parameterization improves the jensen wake model and its implementation for power optimization of an operating wind farm. *Wind Energy Science*, 4(2):287–302, 2019.

Guillaume Espana. *Étude expérimentale du sillage lointain des éoliennes à axe horizontal au moyen d'une modélisation simplifiée en couche limite atmosphérique*. PhD thesis, 2009.

Guillaume Espana, Sandrine Aubrun, Stéphane Loyer, and Philippe Devinant. Wind tunnel study of the wake meandering downstream of a modelled wind turbine as an effect of large scale turbulent eddies. *Journal of Wind Engineering and Industrial Aerodynamics*, 101:24–33, 2012.

P. Fleming, J. Annoni, J. J. Shah, L. Wang, S. Ananthan, Z. Zhang, K. Hutchings, P. Wang, W. Chen, and L. Chen. Field test of wake steering at an offshore wind farm. *Wind Energy Science*, 2(1):229–239, 2017. doi: 10.5194/wes-2-229-2017. URL `https://www.wind-energ-sci.net/2/229/2017/`.

Paul Fleming, Pieter MO Gebraad, Sang Lee, Jan-Willem van Wingerden, Kathryn Johnson, Matt Churchfield, John Michalakes, Philippe Spalart, and Patrick Moriarty. Simulation comparison of wake mitigation control strategies for a two-turbine case. *Wind Energy*, 18(12):2135–2143, 2015.

Paul Fleming, Jennifer King, Katherine Dykes, Eric Simley, Jason Roadman, Andrew Scholbrock, Patrick Murphy, Julie K Lundquist, Patrick Moriarty, Katherine Fleming, et al. Initial results from a field campaign of wake steering applied at a commercial wind farm–part 1. *Wind Energy Science (Online)*, 4(NREL/JA-5000-73991), 2019.

Paul Fleming, Jennifer King, Eric Simley, Jason Roadman, Andrew Scholbrock, Patrick Murphy, Julie K Lundquist, Patrick Moriarty, Katherine Fleming, Jeroen van Dam, et al. Continued results from a field campaign of wake steering applied at a commercial wind farm–part 2. *Wind Energy Science*, 5(3):945–958, 2020.

Paul A Fleming, Pieter MO Gebraad, Sang Lee, Jan-Willem van Wingerden, Kathryn Johnson, Matt Churchfield, John Michalakes, Philippe Spalart, and Patrick Moriarty. Evaluating techniques for redirecting turbine wakes using sowfa. *Renewable Energy*, 70:211–218, 2014.

Sten Frandsen. On the wind speed reduction in the center of large clusters of wind turbines. *Journal of Wind Engineering and Industrial Aerodynamics*, 39(1-3): 251–265, 1992.

Sten Frandsen, Rebecca Barthelmie, Sara Pryor, Ole Rathmann, Søren Larsen, Jørgen Højstrup, and Morten Thøgersen. Analytical modelling of wind speed deficit in large offshore wind farms. *Wind Energy: An International Journal for Progress and Applications in Wind Power Conversion Technology*, 9(1-2):39–53, 2006.

Joeri A Frederik, Bart M Doekemeijer, Sebastiaan P Mulders, and Jan-Willem van Wingerden. The helix approach: Using dynamic individual pitch control to enhance wake mixing in wind farms. *Wind Energy*, 2020.

Robert Edmund Froude. On the part played in propulsion by differences of fluid pressure. *Trans. Inst. Naval Architects*, 30:390, 1889.

E Torres Garcia, S Aubrun, O Coupiac, N Girard, and M Boquet. Statistical characteristics of interacting wind turbine wakes from a 7-month lidar measurement campaign. *Renewable energy*, 130:1–11, 2019.

Pieter Gebraad, Jared J Thomas, Andrew Ning, Paul Fleming, and Katherine Dykes. Maximization of the annual energy production of wind power plants by optimization of layout and yaw-based wake control. *Wind Energy*, 20(1):97–107, 2017.

Pieter MO Gebraad and JW Van Wingerden. A control-oriented dynamic model for wakes in wind plants. In *Journal of Physics: Conference Series*, volume 524, page 012186. IOP Publishing, 2014.

Pieter MO Gebraad, Paul A Fleming, and Jan-Willem van Wingerden. Wind turbine wake estimation and control using floridyn, a control-oriented dynamic wind plant model. In *2015 American Control Conference (ACC)*, pages 1702–1708. IEEE, 2015.

Pieter MO Gebraad, FW Teeuwisse, JW Van Wingerden, Paul A Fleming, SD Ruben, JR Marden, and LY Pao. Wind plant power optimization through yaw control using a parametric model for wake effects—a cfd simulation study. *Wind Energy*, 19(1):95–114, 2016.

Hermann Glauert. Airplane propellers. In *Aerodynamic theory*, pages 169–360. Springer, 1935.

WIND ENERGY COUNCIL GLOBAL. Global wind report 2018. *Bruxelas:[sn]*, 2019.

Tuhfe Göçmen, Paul Van der Laan, Pierre-Elouan Réthoré, Alfredo Peña Diaz, Gunner Chr Larsen, and Søren Ott. Wind turbine wake models developed at the technical university of denmark: A review. *Renewable and Sustainable Energy Reviews*, 60:752–769, 2016.

I Grant, P Parkin, and X Wang. Optical vortex tracking studies of a horizontal axis wind turbine in yaw using laser-sheet, flow visualisation. *Experiments in fluids*, 23(6):513–519, 1997.

Ian Grant and P Parkin. A dpiv study of the trailing vortex elements from the

blades of a horizontal axis wind turbine in yaw. *Experiments in Fluids*, 28(4): 368–376, 2000.

Flavio Heer, Peyman Mohajerin Esfahani, Maryam Kamgarpour, and John Lygeros. Model based power optimisation of wind farms. In *2014 European Control Conference (ECC)*, pages 1145–1150. IEEE, 2014.

U Högström, DN Asimakopoulos, H Kambezidis, CG Helmis, and A Smedman. A field study of the wake behind a 2 mw wind turbine. *Atmospheric Environment (1967)*, 22(4):803–820, 1988.

Michael F Howland, Juliaan Bossuyt, Luis A Martínez-Tossas, Johan Meyers, and Charles Meneveau. Wake structure in actuator disk models of wind turbines in yaw under uniform inflow conditions. *Journal of Renewable and Sustainable Energy*, 8(4):043301, 2016.

Giacomo Valerio Iungo and Fernando Porté-Agel. Volumetric lidar scanning of wind turbine wakes under convective and neutral atmospheric stability regimes. *Journal of Atmospheric and Oceanic Technology*, 31(10):2035–2048, 2014.

NO Jensen. A note on wind turbine interaction. *Riso-M-2411, Risoe National Laboratory, Roskilde, Denmark*, page 16, 1983.

Ángel Jiménez, Antonio Crespo, and Emilio Migoya. Application of a les technique to characterize the wake deflection of a wind turbine in yaw. *Wind energy*, 13 (6):559–572, 2010.

Kathryn E Johnson and Geraldine Fritsch. Assessment of extremum seeking control for wind farm energy production. *Wind Engineering*, 36(6):701–715, 2012.

I Katic, Jørgen Højstrup, and Niels Otto Jensen. A simple model for cluster efficiency. In *European wind energy association conference and exhibition*, volume 1, pages 407–410, 1986.

RE Keck, R Mikkelsen, N Troldborg, M de Maré, and KS Hansen. Synthetic atmospheric turbulence and wind shear in large eddy simulations of wind turbine wakes. *Wind Energy*, 17:1247–1267, 2014. doi: 10.1002/we.1631.

Daniel B Kirk-Davidoff and David W Keith. On the climate impact of surface roughness anomalies. *Journal of the atmospheric sciences*, 65(7):2215–2234, 2008.

Torben Knudsen, Thomas Bak, and Mikael Svenstrup. Survey of wind farm control—power and fatigue optimization. *Wind Energy*, 18(8):1333–1351, 2015.

Gunner C Larsen, Helge Aa Madsen, Ferhat Bingöl, Jakob Mann, Søren Ott, Jens N Sørensen, Valery Okulov, Niels Troldborg, Morten Nielsen, Kenneth Thomsen, et al. Dynamic wake meandering modeling. *Risø National Laboratory*, 2007.

Gunner C Larsen, Helge Aa Madsen, Kenneth Thomsen, and Torben J Larsen. Wake meandering: a pragmatic approach. *Wind Energy: An International Journal for Progress and Applications in Wind Power Conversion Technology*, 11(4):

377–395, 2008.

Gunner Chr Larsen. *A simple wake calculation procedure*. Risø National Laboratory, 1988.

Torben J Larsen, Helge Aagaard Madsen, Gunner Chr Larsen, Niels Troldborg, and N Johansen. Status on development and validation of the dynamic wake meandering (dwm) model. In *EUROMECH Colloquium 508 on Wind Turbine Wakes*, pages 70–72. Universidad Politécnica de Madrid, 2009.

LEM Lignarolo, D Ragni, CJ Ferreira, and GJW Van Bussel. Experimental comparison of a wind-turbine and of an actuator-disc near wake. *Journal of Renewable and Sustainable Energy*, 8(2):023301, 2016.

PBS Lissaman. Energy effectiveness of arbitrary arrays of wind turbines. *Journal of Energy*, 3(6):323–328, 1979.

Ewan Machefaux, Gunner Chr Larsen, Niels Troldborg, Mac Gaunaa, and Andreas Rettenmeier. Empirical modeling of single-wake advection and expansion using full-scale pulsed lidar-based measurements. *Wind Energy*, 18(12):2085–2103, 2015a.

Ewan Machefaux, Gunner Chr Larsen, Niels Troldborg, Mac Gaunaa, and Andreas Rettenmeier. Empirical modeling of single-wake advection and expansion using full-scale pulsed lidar-based measurements. *Wind Energy*, 18(12):2085–2103, 2015b.

LAH Machielse, S Barth, ETG Bot, HB Hendriks, and JG Schepers. Evaluation of “heat and flux" farm control. final report. Technical report, ECN-E–07-105, 2008.

S Macrì, O Coupiac, N Girard, Annie Leroy, and S Aubrun. Experimental analysis of the wake dynamics of a modelled wind turbine during yaw manoeuvres. In *Journal of Physics: Conference Series*, volume 1037, page 072035. IOP Publishing, 2018.

S Macrì, S Aubrun, A Leroy, and N Girard. Experimental investigation of wind turbine wake dynamics during yaw variation. In *Journal of Physics: Conference Series*, volume 1618, page 022053. IOP Publishing, 2020.

S. Macrí, S. Aubrun, A. Leroy, and N. Girard. Experimental investigation of wind turbine wake and load dynamics during yaw manoeuvres. *Wind Energy Science Discussions*, 2020:1–20, 2020. doi: 10.5194/wes-2020-105. URL `https://wes.copernicus.org/preprints/wes-2020-105/`.

S Macrì, T Duc, A Leroy, N Girard, and S Aubrun. Experimental analysis of time delays in wind turbine wake interactions. *Journal of Physics: Conference Series*, 1618:062058, sep 2020. doi: 10.1088/1742-6596/1618/6/062058. URL `https://doi.org/10.1088%2F1742-6596%2F1618%2F6%2F062058`.

M Magnusson and A-S Smedman. Air flow behind wind turbines. *Journal of Wind Engineering and Industrial Aerodynamics*, 80(1-2):169–189, 1999.

M Magnusson and AS Smedman. A practical method to estimate wind turbine wake characteristics from turbine data and routine wind measurements. *Wind Engineering*, pages 73–92, 1996.

Neha Marathe, Andrew Swift, Brian Hirth, Richard Walker, and John Schroeder. Characterizing power performance and wake of a wind turbine under yaw and blade pitch. *Wind Energy*, 19(5):963–978, 2016.

Davide Medici and PH Alfredsson. Measurements on a wind turbine wake: 3d effects and bluff body vortex shedding. *Wind Energy: An International Journal for Progress and Applications in Wind Power Conversion Technology*, 9(3):219–236, 2006.

Davide Medici and JÅ Dahlberg. Potential improvement of wind turbine array efficiency by active wake control (awc). 2003.

Robert Flemming Mikkelsen and Jens Nørkær Sørensen. Yaw analysis using a numerical actuator disc model. In *Proceedings of 14th IEA Symposium on the Aerodynamics of Wind Turbines*. FFA, 2001. 14th IEA Symposium on the Aerodynamics of Wind Turbines ; Conference date: 04-12-2000 Through 05-12-2000.

Yann-Aël Muller, Sandrine Aubrun, and Christian Masson. Determination of real-time predictors of the wind turbine wake meandering. *Experiments in Fluids*, 56(3):53, 2015.

Wim Munters and Johan Meyers. An optimal control framework for dynamic induction control of wind farms and their interaction with the atmospheric boundary layer. *Philosophical Transactions of the Royal Society A: Mathematical, Physical and Engineering Sciences*, 375(2091):20160100, 2017.

Wim Munters and Johan Meyers. Towards practical dynamic induction control of wind farms: analysis of optimally controlled wind-farm boundary layers and sinusoidal induction control of first-row turbines. *Wind Energy Science*, 3(1): 409–425, 2018.

Søren Ott, Jacob Berg, and Morten Nielsen. Linearised cfd models for wakes. 2011.

Lucy Y Pao and Kathryn E Johnson. A tutorial on the dynamics and control of wind turbines and wind farms. In *2009 American Control Conference*, pages 2076–2089. IEEE, 2009.

P Parkin, Richard Holm, and Davide Medici. The application of piv to the wake of a wind turbine in yaw. In *Particle Image Velocimetry; Gottingen; 17 September 2001 through 19 September 2001*, pages 155–162, 2001.

Fernando Porté-Agel, Hao Lu, and Yu-Ting Wu. Interaction between large wind farms and the atmospheric boundary layer. *Procedia Iutam*, 10:307–318, 2014.

Fernando Porte-Agel, Majid Bastankhah, and Sina Shamsoddin. Wind-turbine and wind-farm flows : a review. *Boundary-layer meteorology.*, 174:1–59, 2020. URL `http://dro.dur.ac.uk/29141/`.

Ramin Rezaei. *Velocity Field Survey of the Interaction Between Blade and Tower*

in Upwind and Downwind Turbines. PhD thesis, University of Toledo, 2015.

B Sanderse. Aerodynamics of wind turbine wakes-literature review. 2009.

J Schepers. An engineering model for yawed conditions, developed on basis of wind tunnel measurements. In *37th Aerospace Sciences Meeting and Exhibit*, page 39, 1998.

JG Schepers, H Snel, G van Bussel, et al. *Dynamic inflow: yawed conditions and partial span pitch control*. Netherlands Energy Research Foundation ECN, 1995.

Jannik Schottler, Franz Mühle, Jan Bartl, Joachim Peinke, Muyiwa S Adaramola, Lars Sætran, and Michael Hölling. Comparative study on the wake deflection behind yawed wind turbine models. In *Journal of Physics: Conference Series*, volume 854, page 012032. IOP Publishing, 2017.

Jannik Schottler, Jan Michael Simon Bartl, Franz Volker Mühle, Lars Roar Sætran, Joachim Peinke, and Michael Hölling. Wind tunnel experiments on wind turbine wakes in yaw: redefining the wake width. 2018.

Carl R Shapiro, Dennice F Gayme, and Charles Meneveau. Modelling yawed wind turbine wakes: a lifting line approach. *Journal of Fluid Mechanics*, 841, 2018.

Paul Thomas Smulders, G Lenssen, and H van Leeuwen. *Experiments with windrotors in yaw*. Technische Hogeschool, Afdeling der Technische Natuurkunde, Vakgroep . . . , 1981.

H Snel and JG Schepers. *Joint investigation of dynamic inflow effects and implementation of an engineering method*. Netherlands Energy Research Foundation ECN, 1995.

William H Snyder. *Guideline for fluid modeling of atmospheric diffusion*, volume 81. Environmental Sciences Research Laboratory, Office of Research and . . . , 1981.

Michael A Sprague, Jason M Jonkman, and Bonnie Jonkman. Fast modular framework for wind turbine simulation: New algorithms and numerical examples. In *33rd Wind Energy Symposium*, page 1461, 2015.

AM Talmon. A wind tunnel investigation into the effects of tower and nacelle on wind turbine wake flow. *TNO Division of Technology for Society, Report*, pages 84–08479, 1984.

Niels Troldborg, Jens N Sorensen, and Robert Mikkelsen. Numerical simulations of wake characteristics of a wind turbine in uniform inflow. *Wind Energy: An International Journal for Progress and Applications in Wind Power Conversion Technology*, 13(1):86–99, 2010.

JJ Trujillo, F Bingöl, GC Larsen, J Mann, and M Kühn. Light detection and ranging measurements of wake dynamics. part ii: two-dimensional scanning. *Wind Energy*, 14:61–75, 2011. doi: 10.1002/we.402.

Juan José Trujillo and Martin Kühn. Adaptation of a lagrangian dispersion model for wind turbine wake meandering simulation. In *European Wind Energy Con-*

ference (EWEC), 2009.

PL Van Gent, Dirk Michaelis, BW Van Oudheusden, P-É Weiss, Roeland de Kat, Angeliki Laskari, Young Jin Jeon, Laurent David, Daniel Schanz, Florian Huhn, et al. Comparative assessment of pressure field reconstructions from particle image velocimetry measurements and lagrangian particle tracking. *Experiments in Fluids*, 58(4):33, 2017.

guidline VDI. 3783/12, 2000. environmental meteorology, physical modelling of flow and dispersion processes in the atmospheric boundary layer–applications of wind tunnels, 2000.

LJ Vermeer, Jens Nørkær Sørensen, and Antonio Crespo. Wind turbine wake aerodynamics. *Progress in aerospace sciences*, 39(6-7):467–510, 2003.

P. E. J. Vermeulen. An experimental analysis of wind turbine wakes. In *3rd International Symposium on Wind Energy Systems*, pages 431–450, January 1980.

Lukas Vollmer, Gerald Steinfeld, Detlev Heinemann, and Martin Kühn. Estimating the wake deflection downstream of a wind turbine in different atmospheric stabilities: an les study. *Wind Energ. Sci*, 1:129–141, 2016.

S Voutsinas, K Rados, and A Zervos. On the analysis of wake effects in wind parks. *Wind Engineering*, pages 204–219, 1990.

JW Wagenaar, L Machielse, and J Schepers. Controlling wind in ecn's scaled wind farm. *Proc. Europe Premier Wind Energy Event*, pages 685–694, 2012.

J Wang, S Foley, EM Nanos, T Yu, Filippo Campagnolo, CARLO LUIGI Bottasso, Alex Zanotti, Alessandro Croce, et al. Numerical and experimental study of wake redirection techniques in a boundary layer wind tunnel. In *J. Phys. Conf. Ser*, volume 854, pages 10–1088, 2017.

Yu-Ting Wu and Fernando Porté-Agel. Large-eddy simulation of wind-turbine wakes: evaluation of turbine parametrisations. *Boundary-layer meteorology*, 138 (3):345–366, 2011.

Shengbai Xie and Cristina Archer. Self-similarity and turbulence characteristics of wind turbine wakes via large-eddy simulation. *Wind Energy*, 18(10):1815–1838, 2015.

W Yu, VW Hong, C Ferreira, and GAM van Kuik. Experimental analysis on the dynamic wake of an actuator disc undergoing transient loads. *Experiments in Fluids*, 58(10):149, 2017.

Wei Zhang, Corey D Markfort, and Fernando Porté-Agel. Wind-turbine wakes in a convective boundary layer: A wind-tunnel study. *Boundary-layer meteorology*, 146(2):161–179, 2013.

S Zhong and DG Infield. Prediction of wind turbine performance in axial and non-axial flows by a prescribed wake method. In *Proceedings of the 13th BWEA Conference*, pages 261–267, 1991.

Stefano MACRÌ

Contribution à l'optimisation de la gestion de production des parcs éoliens

Résumé : Ces dernières décennies ont connu un fort développement de la demande en énergie éolienne, du fait de ses potentialités pour réduire les émissions de CO2 pour la production d'électricité. Dans ce contexte, il est nécessaire d'optimiser les stratégies de production d'énergie dans les parcs d'éoliennes. En effet ces derniers subissent des pertes de production et une augmentation de la fatigue structurelle des éoliennes est observée. Une des principales causes est liée aux interactions de sillages. Des solutions prometteuses pour atténuer ces effets sont les stratégies de contrôle d'induction ou de lacet appliquées aux éoliennes individuellement. Ce travail de recherche étudie la réponse dynamique d'un sillage d'une éolienne contrôlée en lacet et de son impact sur la charge exercée sur une éolienne en aval. Des scenarii de désalignement sont ainsi reproduits en souffleries avec des modèles d'éoliennes de type disque poreux. Les expérimentations sont réalisées à deux échelles réduites et pour deux types d'écoulements incidents : un turbulent homogène et isotrope, et une couche limite atmosphérique. Les transitoires rencontrés pendant les manœuvres en lacet sont analysés via des mesures de vélocimétrie laser par imagerie de particules et d'efforts par balance aérodynamique. Les principaux résultats montrent que les dynamiques du sillage et de la charge résultante sont indépendantes du type d'écoulement et du nombre de Reynolds, mais en revanche, elles dépendent du sens de la manœuvre (lacet croissant ou décroissant). En complément, l'interaction de sillage entre deux éoliennes à échelle réelle est également étudiée grâce au traitement de données acquises durant une campagne d'essais de terrain réalisée dans le cadre du projet SMARTEOLE. Grâce aux corrélations entre les séries temporelles de puissance générée, les déphasages entre les réponses des deux éoliennes sont quantifiés et l'influence du niveau d'interaction de sillage et de la vitesse de vent incident sont estimées.
Mots clés : contrôle de parc éolien, modélisation expérimentale d'éoliennes, concept de disque actuateur, interactions de sillages

Contribution to the optimisation of the wind farm production management

Abstract: Last decades saw a huge increase of the global wind energy demand because of its crucial contribution to the reduction of the CO2 emission for power generation. This situation highlighted some challenging aspects, such as the necessity to improve power yield maximization strategies. Indeed, wind farms (WFs) experience wake interactions, leading to power losses and fatigue loads for wind turbines (WTs). Promising solutions to mitigate these effects are based on Wind Farm control. The most common solutions currently being studied are the induction and the yaw control (or wake steering) strategies by controlling WTs individually. The present work deals with yaw control strategies and aims to characterize the effect of wind turbine wake deviation on the dynamics and global load variations of a downstream wind turbine, during a positive and negative yaw manoeuvre representing a misalignment/realignment scenarii. These were reproduced in wind tunnels while modelling the WTs as porous discs. Experiments were performed at two reduction scales and for two inflow conditions: homogenous isotropic and turbulent, and atmospheric boundary layer flows. The transient processes during yaw maneuvers were analysed from PIV and load measurement. While overall results show a non-dependence on the wake and load dynamics of the flow conditions and Reynolds scales, they highlight an influence of the yaw maneuver direction. In addition, the wake interaction between two full-scale WTs was also analysed through the processing of WT operational data acquired during a measurement campaign from the SMARTEOLE project. Through inter-correlations of power time series, time delays between neighboring WT responses were quantified, and their dependence to the degree of wake interaction and to the incoming wind speed is finally assessed.
Keywords: : wind farm control, wind turbine modelling, wind tunnel, actuator-disc-concept, wake interactions

Laboratoire PRISME
8 Rue Léonard de Vinci
45072 Orléans, France